

DEVELOPMENT OF CERIUM-DOPED GLASS SCINTILLATORS FOR
APPLICATIONS IN PROTON COMPUTED TOMOGRAPHY



A Thesis Submitted in Partial Fulfillment of the Requirements for the
Degree of Doctor of Philosophy in Physics
Suranaree University of Technology
Academic Year 2022

การพัฒนาซินทิลเลเตอร์ชนิดแก้วเจือด้วยซีเรียมเพื่อประยุกต์ใช้ใน
เครื่องสร้างภาพตัดขวางจากโปรตอนด้วยคอมพิวเตอร์



นายพงษ์นเรศ บุญถึง

วิทยานิพนธ์นี้เป็นส่วนหนึ่งของการศึกษาตามหลักสูตรปริญญาวิทยาศาสตรดุษฎีบัณฑิต
สาขาวิชาฟิสิกส์
มหาวิทยาลัยเทคโนโลยีสุรนารี
ปีการศึกษา 2565

DEVELOPMENT OF CERIUM-DOPED GLASS SCINTILLATORS FOR
APPLICATIONS IN PROTON COMPUTED TOMOGRAPHY

Suranaree University of Technology has approved this thesis submitted in
partial fulfillment of the requirements for the Degree of Doctor of Philosophy.

Thesis Examining Committee



(Dr. Wanchaloem Poonsawat)

Chairperson



(Asst. Prof. Dr. Chinorat Kobdaj)

Member (Thesis Advisor)

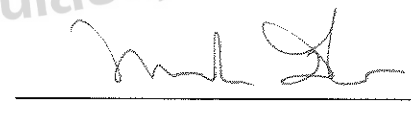

(Prof. Dr. Yupeng Yan)

Member (Thesis Co-advisor)


A. Kaewkhao

(Assoc. Prof. Dr. Jakrapong Kaewkhao)

Member (Thesis Co-advisor)


(Assoc. Prof. Dr. Panomsak Meemon)

Member


(Assoc. Prof. Dr. Chatchai Jothityangkoon)

Vice Rector for Academic Affairs
and Quality Assurance


(Prof. Dr. Santi Maensiri)

Dean of Institute of Science

พงษ์นเรศ บุญถึง: การพัฒนาซินทิลเลเตอร์ชนิดแก้วเจือด้วยซีเรียมเพื่อประยุกต์ใช้ในเครื่องสร้างภาพตัดขวางจากโปรตอนด้วยคอมพิวเตอร์ (DEVELOPMENT OF CERIUM-DOPED GLASS SCINTILLATORS FOR APPLICATIONS IN PROTON COMPUTED TOMOGRAPHY) อาจารย์ที่ปรึกษา : ผู้ช่วยศาสตราจารย์ ดร.ชินรัตน์ กอบเดช, 87 หน้า.

คำสำคัญ: ซินทิลเลเตอร์ชนิดแก้ว/ ซีเรียม/ ลำอนุภาคโปรตอน/ โปรไฟล์ความลึกของโดส

เครื่องสร้างภาพตัดขวางจากโปรตอนด้วยคอมพิวเตอร์ซึ่งเป็นเครื่องมือสร้างภาพทางการแพทย์ 3 มิติ เป็นเครื่องมือในการวินิจฉัยผู้ป่วยก่อนเข้ารับการรักษาด้วยโปรตอน ในการสร้างภาพตัดขวางจากโปรตอนด้วยคอมพิวเตอร์ การวัดเส้นทางเดินของอนุภาคโปรตอนและการวัดพลังงานของโปรตอนเป็นหัวใจหลักในการสร้างภาพ ซินทิลเลเตอร์ชนิดแก้วเจือด้วยธาตุหายากมีความน่าสนใจสำหรับการวัดพลังงาน เนื่องจากต้นทุนต่ำ รูปร่างยืดหยุ่น และความยาวคลื่นที่เปล่งออกมาที่มองเห็นได้ แก้วบอเร็ตโดยการเจือแร่โลหะหายากถูกสังเคราะห์โดยวิธีหลอมและทำให้เย็นตัวลงอย่างรวดเร็ว แก้วแกโดลิเนียม-แบเรียม-ฟลูออโรบอเร็ตและแกโดลิเนียม-อะลูมิเนียม-ฟลูออโรบอเร็ตที่เจือด้วยซีเรียมไอออนได้ถูกสนใจเพื่อศึกษาคุณสมบัติทางกายภาพและทางแสง คุณสมบัติทางกายภาพประกอบไปด้วยความหนาแน่นของแก้วและคุณสมบัติการเปล่งแสงวับ เช่น การส่องผ่านและโฟโตลูมิเนสเซนซ์และเวลาสลายตัว งานวิจัยนี้ยังศึกษาเลขออกซิเดชันของซีเรียมโดยใช้เทคนิค X-ray Absorption Near Edge Structure ในด้านของการทดสอบกับรังสี ซินทิลเลเตอร์ชนิดแก้วถูกทดสอบด้วยรังสีเอกซ์และเปรียบเทียบกับผลึกมาตรฐาน BGO นอกจากนี้ ซินทิลเลเตอร์ชนิดแก้วยังถูกทดสอบด้วยลำอนุภาคโปรตอนที่พลังงาน 70 MeV เพื่อแสดงลักษณะของโปรไฟล์ความลึกของโดส (depth-dose profile) ของลำอนุภาคโปรตอน ระบบการวัด 2 ชนิดของวัสดุดูดซับซึ่งประกอบไปด้วย Virtual water phantom และน้ำ โปรไฟล์ความลึกของโดสจะถูกหาโดยวัดแสงที่เปล่งจากแก้วและการเปลี่ยนความหนาของวัสดุดูดซับ ผลการคำนวณแสดงให้เห็นว่าวัสดุดูดซับทั้งสองชนิดสามารถใช้ในการจำลอง GATE คำนวณพลังงานการสะสมของลำโปรตอนบนซินทิลเลเตอร์ชนิดแก้วเจือและเปรียบเทียบกับผลของการวัดแสงในวัดโปรไฟล์ความลึกของโดส โปรไฟล์ความลึกของโดสที่คำนวณพบว่ามีผลคล้ายคลึงกับการวัดทั้งวัสดุดูดซับทั้งสองชนิด

สาขาวิชาฟิสิกส์
ปีการศึกษา 2565

ลายมือชื่อนักศึกษา พงษ์นเรศ บุญถึง
ลายมือชื่ออาจารย์ที่ปรึกษา ชินรัตน์ กอบเดช

PHONGNARED BOONTUENG : DEVELOPMENT OF CERIUM-DOPED GLASS
SCINTILLATORS FOR APPLICATIONS IN PROTON COMPUTED TOMOGRAPHY.
THESIS ADVISOR : ASST. PROF. CHINORAT KOBDAJ, Ph.D. 87 PP.

Keyword: scintillating glasses/ cerium/ proton beam/ depth-dose profile

Proton-computed tomography, a 3D medical imaging instrument, is a tool to diagnose the patient before getting proton therapy. To reconstruct the image, it is important to track the path of the proton and measure its energy. Scintillating materials based on rare-earth-doped glasses are interesting for measuring energy because they are low-cost, can be formed into different shapes, and give off light in the visible spectrum. We successfully synthesized the borate glass by doping rare earth elements using a melt-quenching technique. In this work, we focus on gadolinium-barium-fluoroborate and gadolinium-aluminum-fluoroborate glasses doped by cerium ions. The physical and scintillation properties of the fabricated glasses were measured, including glass density and scintillation properties such as transmittance, photoluminescence, and decay time. The oxidation states of cerium were determined using an x-ray absorption near edge structure technique. Under x-ray radiation, the doped glasses were irradiated and compared to those of the standard BGO scintillator. Moreover, the glasses were impinged by a 70 MeV proton beam to demonstrate the depth-dose profile of the proton beam. Two kinds of systems of absorber materials for measurement of the depth-dose profile were considered: virtual water phantom and water. The measurement observed an emission light by changing the absorber thicknesses to get a depth-dose profile. The measurements showed that both materials could be used as absorbers to provide the depth-dose profile. In the GATE simulation, the deposition energy of the proton beam on the glass was calculated and compared to the observed emission in the depth-dose profile. The calculated profiles were found to be compatible with the observed emissions for both absorber materials.

School of Physics
Academic Year 2022

Student's Signature พวงนเรด บุญตุง
Advisor's Signature C. Kobdaj

ACKNOWLEDGEMENTS

The scholarship came with the condition that I complete my doctorate. First and foremost, I told myself that I would just finish my Ph.D. and then go to work. By the way, after finishing my master's degree, I found the motivation to pursue my Ph.D. because I needed to do something in the field of medical physics. I was invited by Thanachot Nasawad, who is a great master's degree student at SUT, to join the Nuclear and Particle Physics Group at SUT. I attended the first meeting of the leader group, which was led by Assistant Professor Dr. Chinorat Kobdaj, who later became my supervisor. He suggested my topics be related to medical physics, and I found the motivation to do the Ph.D. research. I began working on this interesting topic with a novel sensor. Unfortunately, I could not go aboard to do the glass experiment due to the COVID-19 situation. However, because my supervisor has many collaborations, I went to do another topic, which was in contrast to the initial topic. I met Associate Professor Dr. Jakkapong Kaewkao from Nakhon Pathom Rajabhat University who has invited me to begin a new topic-related experimental project that I have never done before. He was so kind and helped me a lot with experiments until our work get published. Fortunately, Dr. Narongrit Ritjoho stepped up to be the lecturer at SUT to develop the pCT system and also help with a lot of my work. He taught me how to use a program for calculating simulations that I had never used before. I could not imagine finishing my Ph.D. without meeting him.

I acknowledge the Science Achievement Scholarship of Thailand (SAST) for financial support as well as the TRF International Research Network Program (IRN62W0006). I also thank the SUT-NANOTEC-SLRI Joint Research Facility (Beam Line 5.2) for Synchrotron Utilization at the Synchrotron Light Research Institute (SLRI), Thailand, for supporting the XAS instrument. We would like to thank Suranaree University of Technology (SUT) and Thailand Science Research and Innovation (TSRI) for supporting this research.

I are very grateful to CEGM members from NPRU, including, Nuanthip Wantana, Yaowaluk Tariwong, Chayani Sarumaha, Supakit Yonphan, and Wasu Cheewasukhanont, for the synthesis and analysis techniques used to produce

the glass scintillator. I acknowledge members from KCMH, Assistant Professor Dr. Taweap Sanghangthum, for controlling a proton beam line and dedicated beam time. I acknowledge members of the Laser and Optics group of SUT for supporting various optical instruments. In particular, I would like to thank Associate Professor Dr. Panomsak Meemon and Jadsada Saetiew for providing the technical setup for the spectrometer and collimator.

I'd like to thank my family for their encouragement and support in completing my Ph.D. My parents' success in their work has inspired me to push myself in my Ph.D. life. I would like to thank my friends from the Nuclear and Particle Physics Group at SUT for helping with my experiments. Finally, I am extremely grateful to myself for completing my Ph.D. By the way, I think I have to improve myself to be a good researcher in the future.

Phongnared Boontueng



CONTENTS

	Page
ABSTRACT IN THAI	I
ABSTRACT IN ENGLISH	II
ACKNOWLEDGEMENTS	III
CONTENTS	VII
LIST OF TABLES	X
LIST OF FIGURES	XI
LIST OF ABBREVIATIONS	XV
CHAPTER	
I INTRODUCTION	1
II RESEARCH BACKGROUND	3
2.1 Proton-computed tomography	3
2.1.1 Position-sensitive detector	4
2.1.2 Residual range detector	4
2.1.3 Evolution of pCT	6
2.2 Physics of proton therapy	7
2.2.1 proton interaction mechanisms	7
2.2.2 Energy loss rate	7
2.2.3 Range	10
2.2.4 Depth-dose profile	12
2.3 Scintillation	13
2.3.1 Physics of scintillation	13
2.3.2 Types of scintillator	17
2.4 Glass scintillators	19
2.4.1 Fabrication of the glass	19
2.4.2 Network former	20
2.4.3 Singlet and triplet states	21
2.4.4 Luminescent center	22
2.5 Cyclotron	23
2.5.1 Physics of proton cyclotron	23

CONTENTS (Continued)

		Page
	2.5.2 KCMH Proton Center	25
III	GADOLINIUM ALUMINUM FLUOROBORATE SCINTILLATING GLASS . . .	26
	3.1 Introduction	26
	3.2 Material and method	28
	3.2.1 scintillating glasses synthesis	28
	3.2.2 Characterizations	28
	3.3 Results and discussion	29
	3.3.1 Physical properties	29
	3.3.2 XANES	30
	3.3.3 Transmittance and optical band gap	31
	3.3.4 Photoluminescence	33
	3.3.5 Decay time	34
	3.3.6 X-ray-induced luminescence	35
	3.4 Summary	35
IV	GADOLINIUM BARIUM FLUOROBORATE SCINTILLATING GLASS . . .	38
	4.1 Introduction	38
	4.2 Materials and Methodologies	38
	4.2.1 Glass scintillator synthesis	38
	4.2.2 Characterizations	39
	4.3 Results and Discussion	40
	4.3.1 Transmittance and optical band gap	40
	4.3.2 Photoluminescence	40
	4.3.3 X-ray induced luminescence	42
	4.3.4 XANES	43
	4.4 Summary	45
V	DEPTH-DOSE PROFILE	47
	5.1 Setup 1: The virtual water phantom	47
	5.1.1 Experimental Setup	47
	5.1.2 Measurement process	49
	5.1.3 Light yield calculations	50
	5.1.4 Simulation	50

CONTENTS (Continued)

	Page
5.1.5 Comparison between experiments and simulations .	51
5.2 Setup 2: The water phantom	52
5.2.1 Experimental Setup	52
5.2.2 Simulation	53
5.2.3 Comparison between experiments and simulations .	55
5.3 Summary	56
VI SUMMARY AND CONCLUSION	57
REFERENCES	59
APPENDICES	
APPENDIX A FABRICATION GLASS AND MEASUREMENT GLASS PROPERTIES	70
A.1 Fabrication of glass	70
A.2 Density measurement	71
A.3 Determine of the oxidation state of Ce^{3+} and Ce^{4+}	71
APPENDIX B INSTALLING SIMULATION SOFTWARE	76
B.1 Install Geant4	76
B.2 Install Root	77
B.3 Install GATE	77
APPENDIX C PROPERTY OF BEAM AT KCMH PROTON CENTER .	78
C.1 Proton beam characterization	78
C.2 The σ of proton beam	79
APPENDIX D MEASURED EMISSION LIGHT AND CALCULATED DE- POSITION ENERGY	81
CURRICULUM VITAE	87

LIST OF TABLES

Table		Page
2.1	The collaboration working on developing the pCT with their technology (Johnson, 2017).	8
2.2	The fitting parameters from BK rule for common materials (Newhauser and Zhang, 2015).	11
2.3	Example of doped lanthanide-earth element with emission wavelength and decay time (\mathcal{T}).	23
3.1	Glass properties, density (ρ), absorption edge of the transmittance spectra, indirect of the optical band gap (E_g), decay time, and light yield which is compared to that of standard BGO scintillator.	29
4.1	Properties, including the density, absorption edge of transmittance, and emission light yield of RL, compared to those of BGO. The chemical composition of $20\text{Gd}_2\text{O}_3-(80-x-y)\text{B}_2\text{O}_3-x\text{BaO}-y\text{CeF}_3$ is defined by the different BaO (x) and CeF_3 (y) concentrations.	42
4.2	Fraction of the cerium oxidation state calculated using the LCF method.	46
A.1	The glass name of GAF and their weight for the glass composition of $25\text{Gd}_2\text{O}_3-(65-x)\text{B}_2\text{O}_3-10\text{AlF}_3-x\text{CeF}_3$ (where $x = 0.0, 0.05, 0.1, 0.2,$ and 0.3 mol%).	70
A.2	The glass name (BGF) and the weight of the glass with composition of $20\text{Gd}_2\text{O}_3-(80-x-y)\text{B}_2\text{O}_3-x\text{BaO}-y\text{CeF}_3$ (where $x = 10, 20,$ and 30 mol%, and $y = 0.1, 0.5, 1.0,$ and 1.5 mol%).	71
C.1	The σ at different distance from the proton nozzle to isocenter.	79

LIST OF FIGURES

Figure		Page
1.1	Number of treatment particle therapy center in worldwide (Han, 2019).	2
2.1	Conceptual design of the pCT consisted of (1) a position-sensitive detector and (2) a residual range detector.	3
2.2	(a) Cross sectional view of ALPIDE pixel by showing the collection CMOS components, (b) Photograph of the ALPIDE, and (c) the structure of Bergen pCT system.	5
2.3	(a) OFFSET tracker and (b) the 2D image of ⁹⁰ Sr beta source.	6
2.4	Type of calorimeter for (a) the homogeneous calorimeters and (b) the sampling calorimeters.	6
2.5	Schematic proton interaction mechanisms: (a) energy loss by inelastic coulombic interactions, (b) distortion of proton path due to repulsive Coulomb elastic scattering with the nucleus, (c) remove a primary proton and create a secondary particles by non-elastic nuclear interaction (p: proton, e: electron, n: neutron, γ : gamma rays) (Newhauser and Zhang, 2015)	9
2.6	The CSDA range of proton for the mediums.	11
2.7	(a) The measurement setup of the silica glass fiber and (b) depth-dose profile and each spectra acquired from the fiber at 100, 180, and 225 MeV of the proton beam (Darafsheh et al., 2017).	13
2.8	(a) The setup of the water phantom and (b) the depth-dose profile of 74 MeV proton beam which is measure by Gd-, Cu-, Ce-doped fibers, and Markus chamber.	14
2.9	(a) The setup of the measurement and (b) the measured scintillation emission by the BC-408 scintillator distributing as a function of depth for a 60 MeV proton beam and simulated depth-dose by Geant4 (Almurayshid et al., 2017).	14

LIST OF FIGURES (Continued)

Figure		Page
2.10	Band structure of an extrinsic doped glass scintillator.	15
2.11	A typical Jablonski diagram.	18
2.12	The structures of borate glass for (a) BO_3 -triangles and (b) BO_4 -tetrahedra.	20
2.13	Schematic structure of the 2-dimension glass former.	21
2.14	Ground and excited states for singlet and triplet states.	22
2.15	Top view of the schematic cyclotron. The dees are under magnetic field (B), perpendicular to the dees.	24
2.16	(a) The cyclotron of the KCMH proton center, and (b) energy selection, which reduces the proton energy from 250 MeV to a range of 70–230 MeV. The red line represents the 250 MeV beam direction from the cyclotron.	25
3.1	Image of the fabricated scintillating glasses, $25\text{Gd}_2\text{O}_3-(65-x)\text{B}_2\text{O}_3-10\text{AlF}_3-x\text{CeF}_3$ (where $x = 0.05, 0.1, 0.2,$ and 0.3 mol%).	28
3.2	Ce L_{III} -edge XANES profiles of the (a) fabricated scintillating glasses and (b) CeF_3 and CeO_2 standards.	30
3.3	(a) Transmittance spectra of the fabricated scintillating glasses and (b) indirect optical band gap plotted from Tauc's relation. The dashed lines are drawn based on the calculated edge from Tauc's relation, indicating the optical band gap.	32
3.4	(a) Excitation spectra ($\lambda_{em} = 360$ nm) and (b) emission spectra ($\lambda_{ex} = 312$ nm) of the fabricated scintillating glasses.	34
3.5	Luminescence decay time measurements of the fabricated scintillating glasses.	36
3.6	X-ray-induced luminescence spectra of the fabricated scintillating glasses compared to that of the standard BGO scintillator. The BGO spectrum is scaled down by a factor of 5.	37
4.1	Image of the fabricated scintillating glass, including (1) B10GF:Ce1.0, (2) B20GF:Ce1.0, (3) B30GF:Ce1.0, (4) B10GF:Ce0.1, (5) B10GF:Ce0.5, and (6) B10GF:Ce1.5.	39

LIST OF FIGURES (Continued)

Figure		Page
4.2	(a) Transmittance spectra and (b) Tauc's plot as a function of photon energy of doped GBF glasses.	41
4.3	Excitation and emission spectra of Ce-doped GBF glasses.	43
4.4	RL spectra of the Ce-doped GBF glasses.	44
4.5	The Ce L_{III} -edge XANES spectra of GBF glasses doped at different Ce concentration and the reference spectra of CeF_3 and CeO_2	45
5.1	(a) The setup of the depth-dose profile in the setup of the virtual water phantom where x is the VPW thickness and (b) the experimental setup in the gantry room at KCMH. The red arrow represents the proton beam direction in the vertical direction.	48
5.2	The schematic measurement process.	49
5.3	The simulation of the measurement in the virtual water phantom. The red arrow represents the proton beam direction from the nozzle to the glass sample.	51
5.4	Comparison the results between experiments and simulations.	52
5.5	Schematic setup for the measurement of the water phantom. The water tank is made from an 10 mm acrylic. The scintillating glass was compacted with the collimator inside the glass holder, where it is made of 3 mm PETG.	53
5.6	The setup of the water phantom of the depth-dose profile at KCMH.	54
5.7	The simulation of the depth-dose profile in the setup of the water phantom. The proton beam radiates to the glass sample.	54
5.8	Comparison between experiments and simulations of the results in the setup of the water phantom.	55

LIST OF FIGURES (Continued)

Figure		Page
A.1	Preparing and mixing the glass compositions in the alumina crucible.	72
A.2	High temperature furnace at NPRU.	72
A.3	Reducing the stress of the glass after melting at high temperature.	73
A.4	Cutting and polishing the synthesized glasses into the required dimensions.	73
A.5	The 4-digit sensitive microbalance (AND, HR-200) for measuring the glass density.	74
A.6	Fraction of the cerium oxidation state calculated using the LCF method.	74
C.1	Beam profile measured by ALPIDE sensor.	77
C.2	Distance from the proton nozzle to the isocenter, which is defined from the proton nozzle to the isocenter. The σ is shown for the 70 MeV proton energy.	78
D.1	Fitted emission light from the scintillating glass from a water in range of 10 - 16.5 mm.	80
D.2	Fitted emission light from the scintillating glass from a water in range of 17 - 20.5 mm.	81
D.3	Fitted emission light from the scintillating glass from a water of 21 and 22 mm.	82
D.4	Deposition energy of the glasses from the proton beam in a water in range of 10 - 16.5 mm.	83
D.5	Deposition energy of the glasses from the proton beam in a water in range of 17 - 20.5 mm.	84
D.6	Deposition energy of the glasses from the proton beam in a water in range of 21 - 22.5 mm.	85

LIST OF ABBREVIATIONS

pCT	Proton-computed tomography
PT	Proton therapy
RE	Rare-earth elements
LSO	Cerium-doped lutetium oxyorthosilicate
YAG:Ce	Yttrium aluminum garnet activated by cerium
NaI(Tl)	Thallium-activated sodium iodide
CsI(Tl)	Thallium-activated cesium iodide
GAF	Gadolinium Aluminum Fluoroborate
GBF	Gadolinium Barium Fluoroborate
PIL	Proton-induced luminescence
XIL	X-ray-induced luminescence
KCMH	King Chulalongkorn Memorial Hospital
PETG	Polyethylene terephthalate glycol-modified
BGO	Bismuth Germanate
PMMA	Polymethyl Methacrylate
Ce	Cerium
Pr	Praseodymium
SM	Samarium
Nd	Neodymium
Eu	Europium
Gd	Gadolinium
Tb	Terbium
Dy	Dysprosium

CHAPTER I

INTRODUCTION

Proton therapy center, nowadays, is growing in worldwide, as shown in Figure 1.1. pCT is a proposed medical 3D imaging technique that uses a proton beam with energy up to 250 MeV to penetrate the human body and measure stopping power distributions inside the tissue volume. This technique is compatible with proton therapy and is currently under development worldwide (Bashkirov et al., 2016; Civinini et al., 2013; Saraya et al., 2014; Scaringella et al., 2013; Schulte et al., 2004). The present design of pCT requires a novel calorimeter that can precisely measure the residual energy of the scattered proton. It consists of a single array or multiple arrays of crystal scintillator, which convert radiation-induced ionization from proton beams into scintillation light. The light is then collected by a photomultiplier or large-area photodiode (Scaringella et al., 2013; Schulte et al., 2004). Scintillating materials with high density, short decay time, and high light yield are required for the development of highly efficient calorimeters. Many scintillating crystal materials have been proposed to apply as pCT calorimeter for instance, LSO (Schulte et al., 2004), YAG:Ce (Civinini et al., 2013; Scaringella et al., 2013), NaI(Tl) (Saraya et al., 2014), CsI(Tl) (Bashkirov et al., 2016).

Glass scintillator are an interesting alternative to crystal scintillator owing to their attractive characteristics, such as low cost, radiation absorption ability, ease of fabrication in different sizes and shapes, and durability in a normal atmosphere. Rare earth (RE) elements are extensively used as glass compounds to enhance the scintillating properties of glass. Some RE elements are considered to be luminescence centers in the glass to emit ultraviolet, visible, and near-infrared photons. Moreover, some of them can improve the emission intensity by transferring energy into suitable luminescence centers. For dosimeter or calorimeter applications in particle therapy, the glass scintillator requires high density to increase the stopping power of the energetic particles and short decay time to avoid redundancy of the incoming particles. High-density glass scintillator can be produced from high-Z elements, such as

gadolinium doped with lanthanide earth elements as luminescence centers (Sun et al., 2014b). Many scintillation studies have shown that cerium can be an excellent luminescent center because it can provide a short decay time in of the order of nanoseconds (Chewpraditkul et al., 2011; Pan et al., 2020; Rajaramakrishna et al., 2020; Shi et al., 2020; Sontakke et al., 2016; Sun et al., 2014a; Wantana et al., 2018; Yao et al., 2016) and it increases the radiation hardness of the Ce-doped glasses (Liu et al., 2016; Wang et al., 2003).

The aim of this work is to synthesize the scintillating glass based on doping of gadolinium and cerium. Cerium fluoride (CeF_3), an inorganic compound, was selected as the dopant cerium instead of the common cerium oxide (CeO_2) because cerium fluoride shows a higher ratio of Ce^{3+} to Ce^{4+} compared to cerium oxide (Sun et al., 2015b). Based on the required applications, the fabricated glass scintillators demonstrated emission spectra after irradiated by X-ray and proton beam. Furthermore, the depth-dose profiles of the proton were measured by the fabricated scintillating glasses. GATE simulations were also used to calculate the energy deposition of the fabricated glass scintillator and with compare the experimental results.

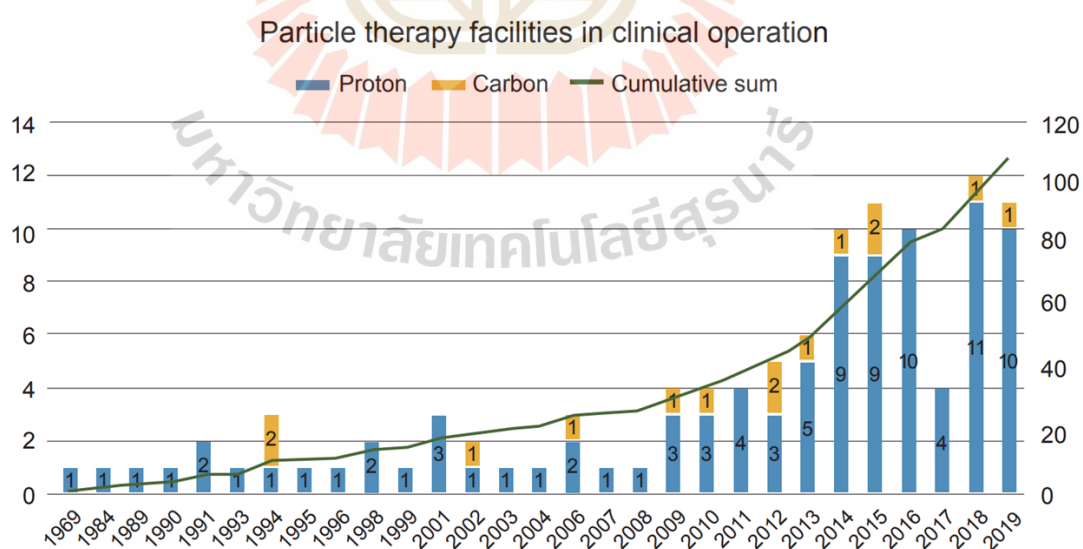


Figure 1.1 Number of treatment particle therapy center in worldwide (Han, 2019).

CHAPTER II

RESEARCH BACKGROUND

2.1 Proton-computed tomography

Proton-computed tomography (pCT) is computed tomography based on a proton beam. To reconstruct the imaging, a proton path of each particle is measured by the position detector before and after passing through a patient or phantom. To identify the type or materials of the patient or phantom, a proton energy should be determined using a calorimeter. In general, there are two types of calorimeters, homogeneous and sampling calorimeters. These details are described in Section 2.1.2.

The first reliably conceptual design of a pCT was proposed by Schulte (Schulte et al., 2004). The concept of pCT is basically comprised of a position-sensitive detector (PSD) and a residual energy-range detector (RRD). The PSD is considered to use the array tracking system to realize the particle path before and after passing through the patients or phantoms. Subsequently, the remaining energy after passing through the patients or phantoms is determined by the RRD. The RRD, which sometimes is called calorimeter, is currently under research to increase accuracy and reduce the materials budget.

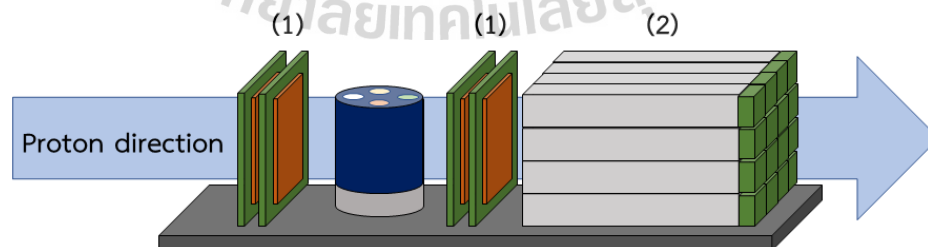


Figure 2.1 Conceptual design of the pCT consisted of (1) a position-sensitive detector and (2) a residual range detector.

2.1.1 Position-sensitive detector

The position of the proton path is critical in reconstructing and generating the patient's image. A detector with high resolution was used to measure the proton paths and classify each of the incoming protons. MIMOSA23 (Haas et al., 2018) and ALPIDE (Alme et al., 2020) sensor were among the CMOS sensors interested in serving as the SPD. In figure 2.2, a pixel in the ALPIDE sensors, which is made from silicon, produces electron-hole pairs when the incoming charged particles ionize the medium in this layer. The ionized electrons were collected. And these processes generate electronic signals within a pixel and nearby. In figure 2.2(b), the dimension of each ALPIDE chip is $30 \times 15 \text{ mm}^2$ with a matrix of $1,024 \times 512 \text{ pixels}^2$. Recently, an ALPIDE sensor with higher resolution than the MIMOSA23 sensor was used to measure the proton paths in the prototype of pCT system at the University of Bergen, as shown in figure 2.2(c).

Unlike CMOS sensors, the developer also used the $500 \mu\text{m}$ square multi-cladding BCF-12, which is rearranged in $20 \times 20 \text{ mm}^2$ with orthogonal ones to each other, to create the Optical Fiber Folded Scintillating Extended Tracker Detector (OFFSET), as shown in figure 2.3. The OFFSET tracker uses a read-out channel reduction for beam profile detection (Lo Presti et al., 2014). The example of the OFFSET tracker shows the 2D image, which was irradiated by ^{90}Sr , providing a beta source.

2.1.2 Residual range detector

The RRD used for determining the proton beam energy is called a calorimeter. In figure 2.4 shows two main types of calorimeter, homogeneous calorimeters or sampling calorimeters. The structure of calorimeter is comprised of particle absorption and signal generation, known as passive and active media, respectively.

- Homogeneous calorimeters: The detecting volume is entirely active using scintillating materials. There are several pCT prototypes constructed using scintillating crystal materials as their calorimeters, for example, LSO (Schulte et al., 2004), YAG:Ce (Civinini et al., 2013; Scaringella et al., 2013), NaI(Tl) (Saraya et al., 2014), CsI(Tl) (Bashkirov et al., 2016).

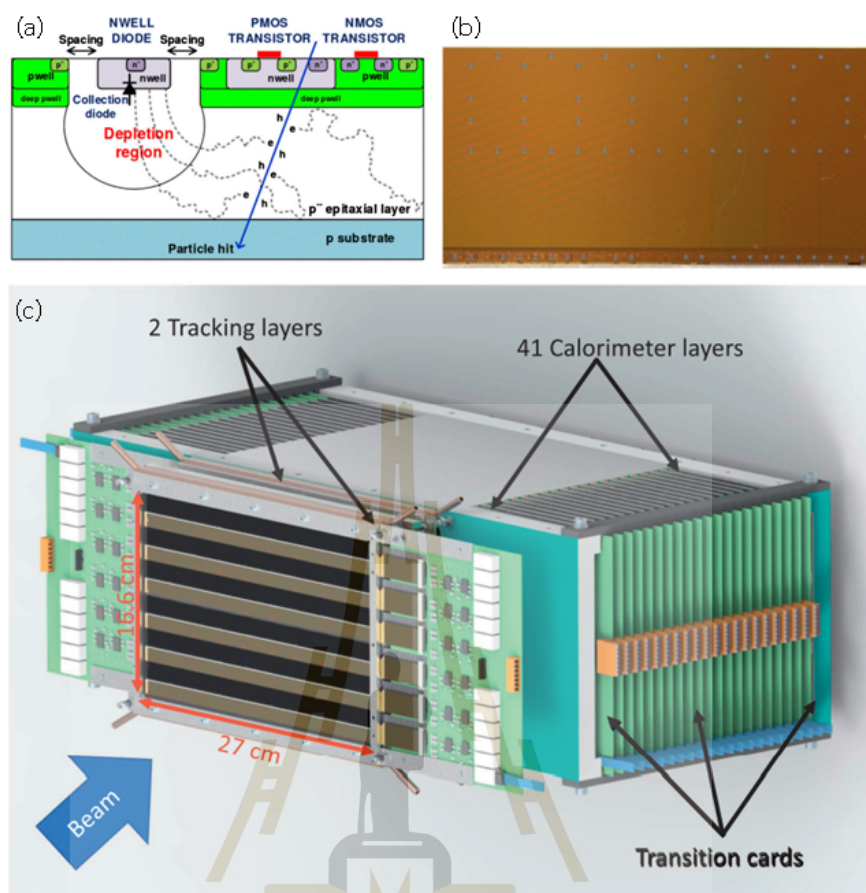


Figure 2.2 (a) Cross sectional view of ALPIDE pixel by showing the collection CMOS components, (b) Photograph of the ALPIDE, and (c) the structure of Bergen pCT system.

- Sampling calorimeters: it has stacks of active and passive media layers, sometimes called a sandwich structure. The stacked layers are arranged perpendicularly to the particle projection. The passive layers are there to absorb the incoming particle energy and help to decrease the number of stacked layers. PMMA, carbon fiber, aluminum, copper, tungsten, and other materials are being studied as passive media under the conditions of each design (Pettersen et al., 2019). The active medium employs a CMOS-based position-sensitive sensor. When compacting with an absorber, the ALPIDE chip can also be used as a sampling calorimeter (Mager, 2016; Pettersen et al., 2019).

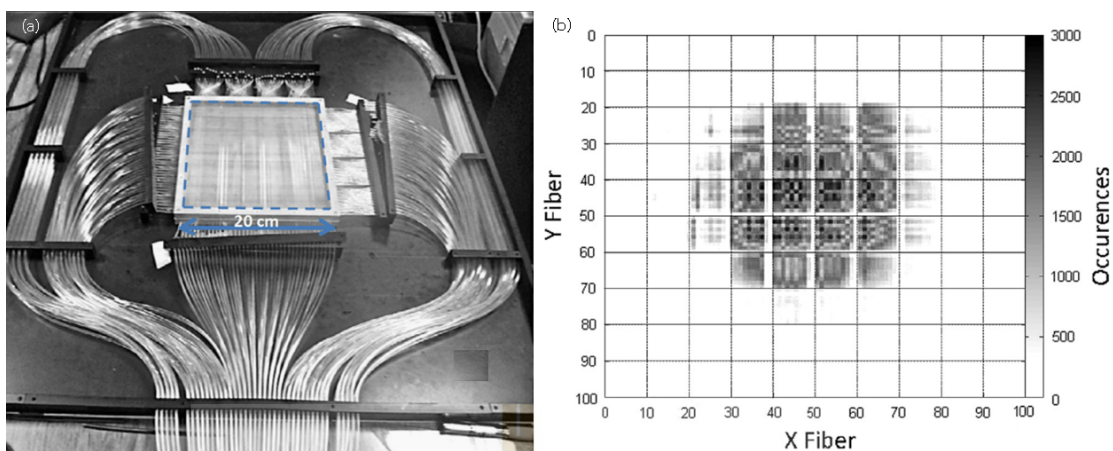


Figure 2.3 (a) OFFSET tracker and (b) the 2D image of ^{90}Sr beta source.

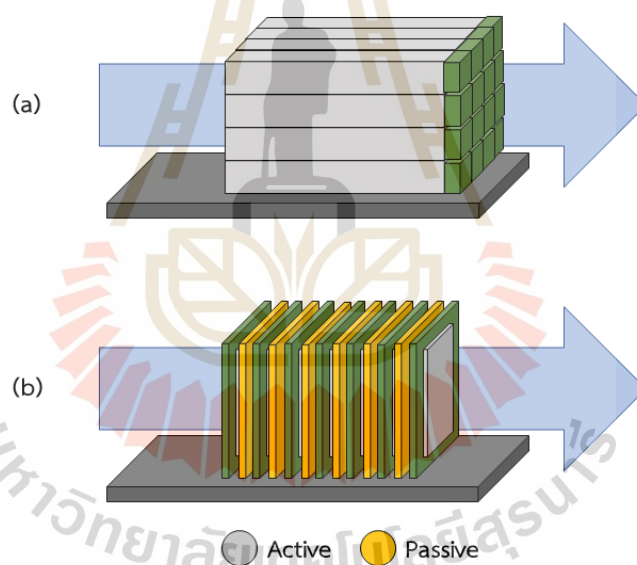


Figure 2.4 Type of calorimeter for (a) the homogeneous calorimeters and (b) the sampling calorimeters.

2.1.3 Evolution of pCT

The successful pCT prototypes were proposed by many collaborations, as presented in Table 2.1. The pCT collaborations used various tracking technologies, such as the Gas Electron Multiplier (GEM), the silicon strip detector, and optical fiber. The silicon detectors based on the MINOSA23 and ALPIDE sensors were

of interest and proposed by the Bergen pCT collaboration. Suranaree University of Technology joined the Bergen pCT collaboration in 2018, and since then we have been developing the pCT prototype based on a silicon detector.

2.2 Physics of proton therapy

2.2.1 proton interaction mechanisms

When protons move through the matter, the charged particles may interact with the medium. In a figure 2.5, types of interactions of protons are including coulombic interactions with atomic electrons, coulombic interactions with the atomic nucleus, and nuclear reactions (Newhauser and Zhang, 2015). For the first interaction, the coulombic interactions with atomic electrons, protons lose kinetic energy on a constant basis as a result of numerous inelastic coulombic interactions with atomic electrons. Because their rest mass is 1832 times greater than that of an electron, most protons move in a straight line. Second, as a moving proton approaches the atomic nucleus, it experiences a repulsive elastic coulombic interaction. As a result, the proton's trajectory changes from the original straight line. In the proton's interaction with the nucleus, the nucleus can emit a proton, gamma ray, neutron, etc. Moreover, proton Bremsstrahlung is possible in the theory. However, this effect is negligible in the therapeutic interaction.

2.2.2 Energy loss rate

The energy loss rate of the ions, or linear stopping power, is defined as the dE and dx , where dE is the mean energy loss and x is the distance. The energy loss rate (S) is depended on the mass density as

$$\frac{S}{\rho} = -\frac{dE}{\rho dx} \quad (2.1)$$

where ρ is the mass density of the absorber. The new formula based on the Bragg-Kleeman (BK) rules (Bragg and Kleeman, 1905) is given by

$$\frac{S}{\rho} = -\frac{dE}{\rho dx} \approx -\frac{E^{1-p}}{\rho \alpha p} \quad (2.2)$$

Table 2.1 The collaboration working on developing the pCT with their technology (Johnson, 2017).

Collaboration	Aperture (cm ²)	Tracking technology	Residual range detector technology
PSI (Pemler et al., 1999)	22.0 × 3.2	Sci Fi	scint. range counter
AQUA (Bucciantonio et al., 2013)	10 × 10	GEM	scint. range counter
PRIMA (Scaringella et al., 2013)	5.1 × 5.1	Si strip	YAG:Ce calorimeter
Niigata (Saraya et al., 2014)	9 × 9	Si strip	Nal calorimeter
QBeRT (Lo Presti et al., 2014)	9 × 9	Sci Fi	Sci Fi range counter
PRaVDA (Taylor et al., 2015)	4.8 × 4.8	Si strip	CMOS APS telescope
LLU/UCSC Phase-II (Bashkirov et al., 2016)	36 × 9	Si strip	5 scint. stage
NIU, FNAL (Naimuddin et al., 2016)	24 × 20	Sci Fi	scint. range counter
pCT-Bergen (Haas et al., 2018)	4.0 × 4.0	MIMOSA23	Sampling calorimeter
pCT-Bergen (Alme et al., 2020)	27.0 × 16.6	ALPIDE	Sampling calorimeter

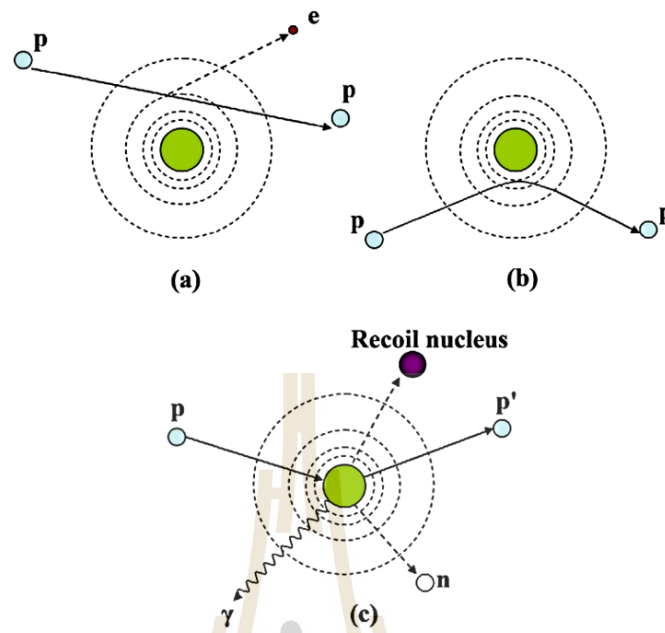


Figure 2.5 Schematic proton interaction mechanisms: (a) energy loss by inelastic coulombic interactions, (b) distortion of proton path due to repulsive Coulomb elastic scattering with the nucleus, (c) remove a primary proton and create a secondary particles by non-elastic nuclear interaction (p: proton, e: electron, n: neutron, γ : gamma rays) (Newhauser and Zhang, 2015)

where ρ is the material density, E is the proton beam energy, α is the materials-dependent constant, and the p is a constant which is depending on the proton energy. The α and p can be achieved by fitting from ranges or stopping power from the measurement or theory.

A complete theory is based on the calculation of the momentum impulse of a stationary, unbound electron, and the impact parameter. The formula, proposed by Bethe (Bethe, 1930) and Bloch (Bloch, 1933), is given by

$$\frac{S}{\rho} = -\frac{dE}{\rho dx} = 4\pi N_A r_e^2 m_e c^2 \frac{Z z^2}{A \beta^2} \left[n \frac{2m_e c^2 \gamma^2 \beta^2}{l} - \beta^2 - \frac{\delta}{2} - \frac{C}{Z} \right] \quad (2.3)$$

where ρ is the material density, N_A is Avogadro's constant, r_e is classical electron radius, m_e is the electron mass, c is the speed of light, Z is the atomic number of the absorber, A is the target-atomic weight, and z is the

atomic number of the projectile, $\beta = \frac{v}{c}$ where v is the velocity of projectile, $\gamma = (1 - \beta^2)^{-1/2}$, I is the mean excitation potential of the absorber, δ is the density corrections arising from the shielding of remote electrons by close electrons, C is the shell correction item for low particle energy. The unit of the Eq. 2.3 is MeV/g cm^{-2} .

2.2.3 Range

The total distance at which half of the protons come to rest is referred to as the proton range. There have been variations in protons due to range straggling. However, an average of the quantity is calculated for the proton beam (not for individual protons). The average range of half-protons is stopped inside the absorber or the medium.

The path of the majority of traveling proton beams is an almost straight line. Thus, the lateral scattering is negligible, and the proton loses its energy in a continuous medium. In this case, the range (R) is given by

$$R(E) = \int_0^E \left(\frac{dE'}{dx} \right)^{-1} dE' \approx \sum_0^E \left(\frac{dE'}{dx} \right)^{-1} \Delta E' \quad (2.4)$$

where E is the proton's kinetic energy. The continuous traveling proton is provided by the summation. However, the simplest formula of proton range can be obtained from the relationship between energy and the special material parameters, which is proposed by the Bragg-Kleeman (BK) rule (Bragg and Kleeman, 1905). The equation of proton range is given by Eq. (2.5)

$$R(E) = \alpha E^p \quad (2.5)$$

where α is the materials-dependent constant, E is the initial proton beam energy, and p is a constant dependent on the proton energy. The average of proton range can be obtained from the Eq. (2.5) using the parameter from Table 2.2.

As the range depends on initial proton energy and the kind of medium, The online programing, Stopping Powers and Ranges for Protons (PSTAR), can calculate the stopping power and the total range of the proton beam. The range

Table 2.2 The fitting parameters from BK rule for common materials (Newhauser and Zhang, 2015).

Material	ρ (g/cm ³)	α	p
Water	1.0	2.633×10^{-3}	1.735
PMMA	1.185	2.271×10^{-3}	1.735
Aluminum	2.698	1.364×10^{-3}	1.719
Lead	11.322	6.505×10^{-4}	1.676

is considered using continuous slowing-down approximation (CSDA) by integrating the reciprocal of the total stopping power (collision plus nuclear), which depends on the proton energy. The CSDA range of the initial proton energy, including water, polystyrene, aluminium, and copper, are presented in figure 2.6. The range in the figure is in units of $\text{g} \cdot \text{cm}^{-2}$. The proton range for each mediums can be obtained by dividing its density by the calculated range in unit of $\text{g} \cdot \text{cm}^2$ (water = $1.00 \text{ g} \cdot \text{cm}^{-3}$, polystyrene = $1.06 \text{ g} \cdot \text{cm}^{-3}$, aluminium = $2.69 \text{ g} \cdot \text{cm}^{-3}$, and copper = $8.96 \text{ g} \cdot \text{cm}^{-3}$).

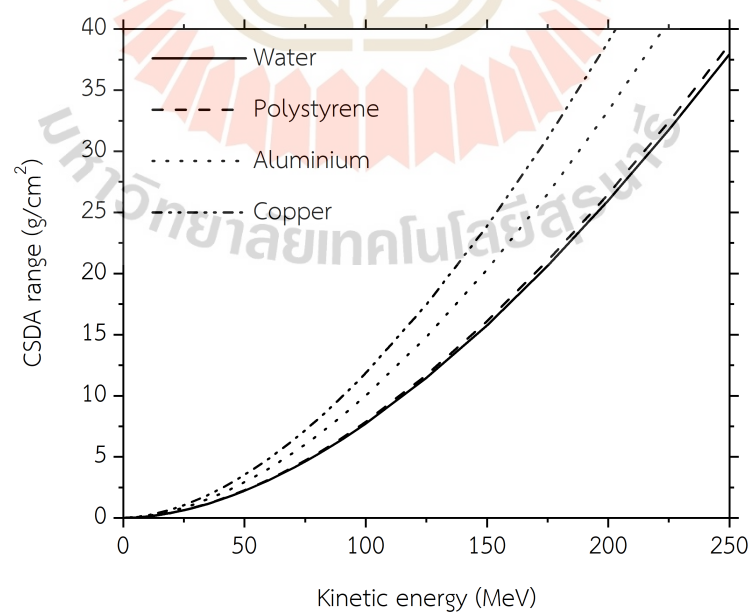


Figure 2.6 The CSDA range of proton for the mediums.

2.2.4 Depth-dose profile

Along its path, the proton beam deposits its energy in the medium (Newhauser and Zhang, 2015). The deposited energy of the proton beam is different for each medium thickness. The depth-dose profile represents the deposited energy of the proton beam for each medium and for each initial proton beam. Typically, a technique to determine the depth-dose profile of the proton beam involves utilizing scintillating materials with different medium thicknesses. Below are the proposed techniques and scintillating materials for measurement of the depth-dose profile.

- Bare silica glass fiber: The measurement of the depth-dose profile is measured by the bare silica glass fiber (Darafsheh et al., 2017). The energies of the proton beam at 100, 180, and 225 MeV were utilized. The emitted spectra from the fiber showed two regions in the 400-500 and 600-700 nm ranges. The depth-dose profile for each proton beam energy was proposed in figure 2.7.
- Doped fibers: The Gd-, Cu-, and Ce-doped fibers were proposed to measure the depth-dose profile for the proton beam at 74 MeV (Hoehr et al., 2019). In figure 2.8(a), The water phantom was used to change the absorber thickness during the measurement. The proton beam was irradiated through water and the doped fiber, respectively. The measured emission from the glass was proposed and compared with the Markus chamber in figure 2.8(b).
- Plastic scintillator: The compact camera was used to set up the large size of the scintillating materials, as shown in figure 2.9(a). The plastic scintillator, BC-408 scintillator, was the proton detector and provided the emission light when the proton was irradiated (Almurayshid et al., 2017). The 60 MeV proton beam traveled from the cyclotron through the plastic scintillator and was compared with the Geant4 simulation. In figure 2.9(b), the depth-dose profile in this setup was illustrated through the measured scintillation and simulation of the proton beam.

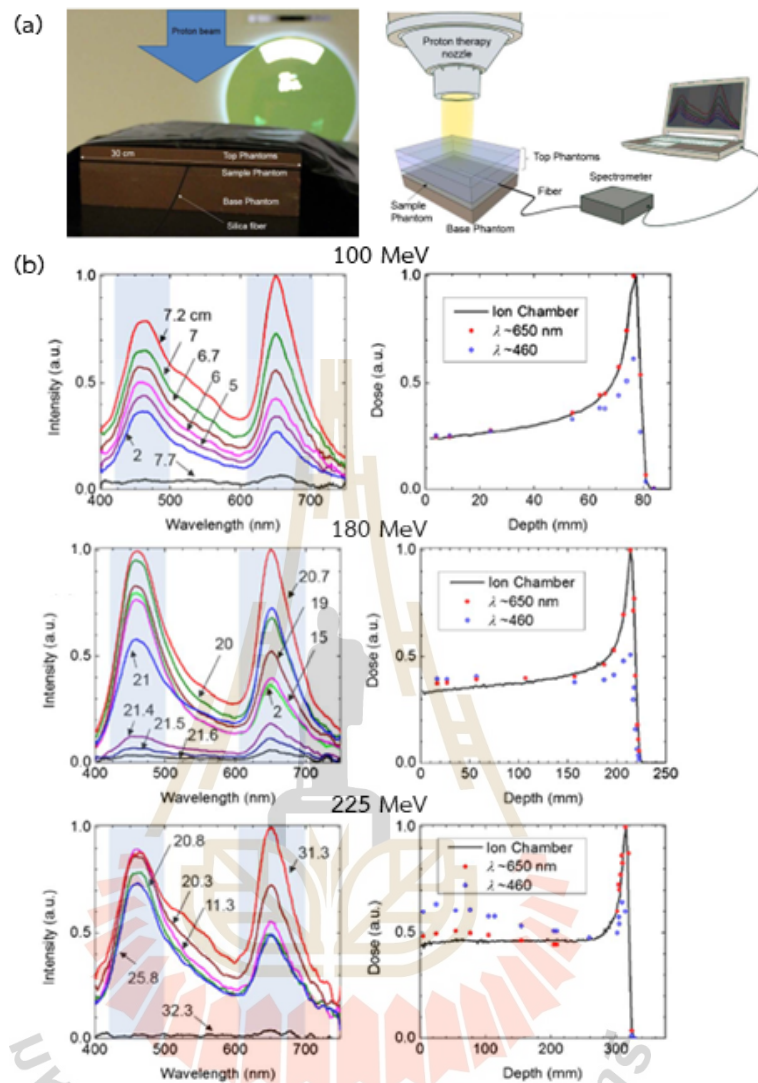


Figure 2.7 (a) The measurement setup of the silica glass fiber and (b) depth-dose profile and each spectra acquired from the fiber at 100, 180, and 225 MeV of the proton beam (Darafsheh et al., 2017).

2.3 Scintillation

2.3.1 Physics of scintillation

In figure 2.10, the scintillation is a complicated physical phenomenon that can be separated into three processes: conversion, energy transfer, and

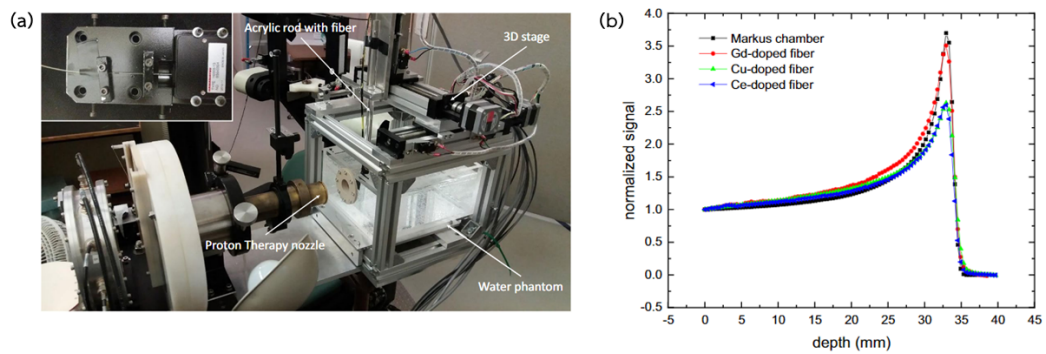


Figure 2.8 (a) The setup of the water phantom and (b) the depth-dose profile of 74 MeV proton beam which is measured by Gd-, Cu-, Ce-doped fibers, and Markus chamber.

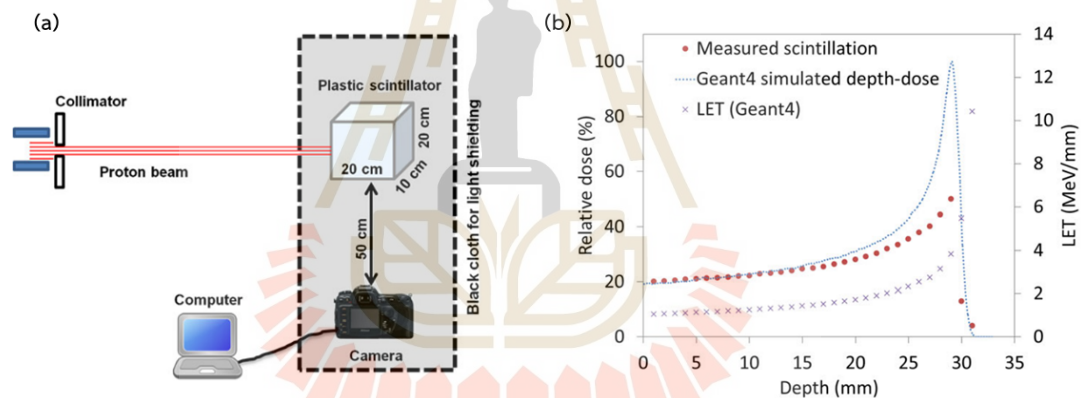


Figure 2.9 (a) The setup of the measurement and (b) the measured scintillation emission by the BC-408 scintillator distributed as a function of depth for a 60 MeV proton beam and simulated depth-dose by Geant4 (Almurayshid et al., 2017).

luminescence. The interaction of the radiation, protons, with the matter occurs with three kinds of mechanisms, reported in Section 2.2.1. In figure 2.10, the scintillation processes are described by:

1. Conversion: When the radiation is absorbed by the scintillating material, it creates primary electron-hole pairs, which, through a cascade effect, make secondary electron-hole pairs.

2. Energy transfer: When the energy of the excited electrons drops below the ionization threshold, this is called thermalization. At the end of this stage, all of the electrons are at the bottom of the conduction band and all of the holes are at the top of the valence band. In the first step, this is completed in less than a picosecond. After the thermalization stage, the excited electrons transfer through the material to the luminescent centers.
3. Luminescence: The excited electrons relax into the valence band by decaying their energy (a photon) and recombining with their hole pairs. The energy of the emitted photon depends on the energy level of the luminescent center. Also, the decay time is determined by the type of luminescent center. The elements with singlet and triplet states provide a decay time range of nanoseconds and microseconds, respectively.

As mentioned in the description of the luminescence, the timescales for each luminescent center of a nanosecond and a millisecond depend on the singlet or triplet state, which can be described clearly with the Jablonski diagram. The

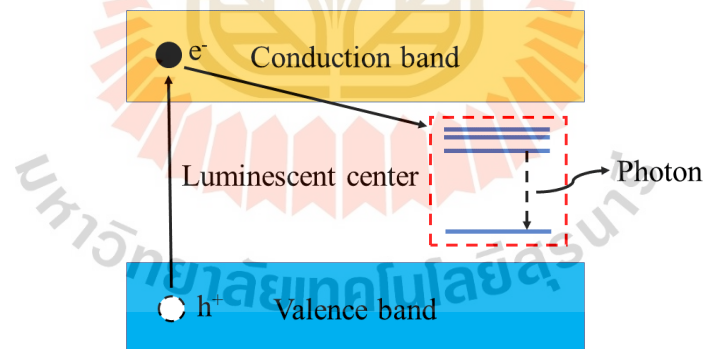


Figure 2.10 Band structure of an extrinsic doped glass scintillator.

Jablonski diagram can describe the possible transition of the molecule during the photoexcited, as proposed in figure 2.11.

- Energy levels: The horizontal black lines indicate the energy levels of a molecule, with the energy increasing down the vertical axis. The thicker

lines represent the lowest vibrational levels of each electronic state, while the thinner lines represent the higher vibrational levels. The singlet state is represented by S (0 total spin angular momentum). The singlet ground state is S_0 , and the first excited singlet ground state is S_1 . For a higher state, S_n is the nth excited singlet state. T denotes triplet states with one total spin angular momentum. The first excited triplet state is T_1 , and the nth excited triplet state for the higher state is T_n .

- Radiative and non-radiative transitions: The colored arrows represent the variety of transitions between molecules, which are divided into radiative and non-radiative transitions: (1) Radiative transitions are transitions between molecules, that emit or absorb photons, and (2) non-radiative transitions are transitions between molecular states without the emission or absorption of photons.
- Absorption: A photon's absorption, as represented by the blue arrows, moves a molecule from its ground state to a higher one. It is the transition with the shortest timescale in the Jablonski diagram, happening over a duration of 10^{-15} seconds. The absorption of the photon stimulates molecule from the S_0 to one of the vibrational levels of the singlet excited states (S_1, S_2, \dots). However, the triplet excited state (T_1, T_2, \dots) is not possible due to conservation of angular momentum.
- Vibrational relaxation: After being promoted to the excited state by absorption, the molecules are in a non-equilibrium condition and suddenly return to the ground state (relaxation). The first way to release their energy is through vibrational relaxation (orange arrows), where the vibrational energy is lost to vibrational modes within the same molecular type (intramolecule) or surrounding molecules (intermolecule). The vibrational relaxation is a quick process that lasts between $10^{-12} - 10^{-10}$ seconds.
- Internal conversion: Excited molecules in a higher singlet state can undergo possible internal conversion to a lower singlet electronic state (purple arrows). Internal conversion is suddenly continued by vibrational relaxation to the lowest electronic level of that state. Internal conversion is proportional to the energy difference between the two electronic states. Internal conversion

occurs in timescales ranging from 10^{-11} to 10^{-9} s in ($S_3 \Rightarrow S_2$, $S_2 \Rightarrow S_1$, ...). By the way, the energy gap between S_0 and S_1 is wider due to internal conversion, leading to a slower timescale in the transition.

- Intersystem crossing: The dark red arrows represent an alternate transition to fluorescence and internal conversion from the S_1 to the T_1 state. Because of the conservation of spin angular momentum, this transition is in principle disallowed. Intersystem crossing competes with other S_1 depopulation transitions (internal conversion and fluorescence) and is too slow to be significant for the vast majority of purely organic compounds. Following intersystem crossing, the molecule will immediately undergo vibrational relaxation to the ground vibrational level T_1 .
- Fluorescence: The green arrow represents the fluorescence emission of the $S_1 \Rightarrow S_0$ radiative transition with a time scale of 10^{-10} to 10^{-7} seconds. The molecules at the lowest vibrational level lose energy to the singlet ground state as a result of the consequence of the vibrational relaxation and conversion processes. The energy loss occurs by emitting a longer wavelength than the absorption.
- Phosphorescence: The emission of photons caused by the $T_1 \Rightarrow S_0$ transition is referred to as phosphorescence. Phosphorescence, like intersystem crossing, is a forbidden transition in principle, but it is weakly permitted due to spin-orbit coupling. A consequence of phosphorescence occurs over a longer timescale, with lifetimes being in the range of 10^{-6} to 10 seconds.

2.3.2 Types of scintillator

There are several types of scintillators, of which we would like to give a brief summary as follows:

- Inorganic scintillators: inorganic scintillators are normally crystals that are grown in high-temperature furnaces. The examples of inorganic scintillators are including lead tungstate ($PbWO_4$), lithium iodide (LiI), sodium iodide (NaI), cesium iodide (CsI), and zinc sulfide (ZnS). These crystalline scintillators have a high density, a high atomic number, and pulse decay durations of less than

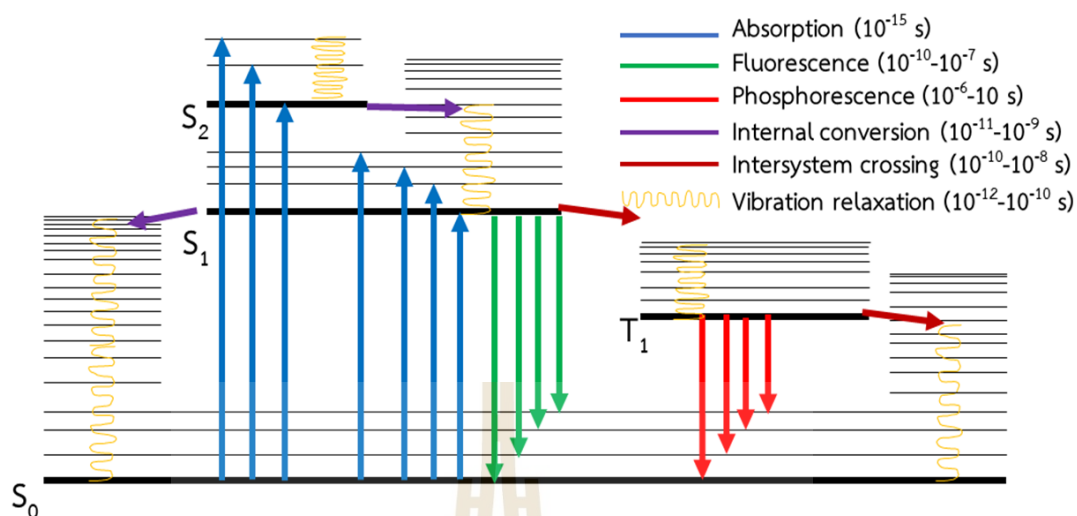


Figure 2.11 A typical Jablonski diagram.

one microsecond. They have a high gamma ray detection efficiency and can handle high count rates. Inorganic crystals can be chopped to tiny sizes and assembled in an array to provide position sensitivity. There are two kinds of luminescence in inorganic scintillators: intrinsic and extrinsic. Self-trapped exciton luminescence is a type of intrinsic luminescence that produces free-exciton luminescence by trapping itself. The exciton luminescence is almost always found in the large bandgap of the semiconductor materials, for example, zinc oxide (ZnO), gallium nitride (GaN), etc. Another kind of inorganic scintillator is the host material, which consists of luminescent centers as the main luminescent centers to emit the photon. The photon or emission properties are dependent on the luminescent ions of the host, for example, bismuth germanate (BGO), cerium fluoride (CeF_3), etc.

- Organic scintillators: The mechanism of scintillation in organic materials is different from that of inorganic crystals. Because the fluorescence process in organic materials is caused by changes in the energy levels of a single molecule, the fluorescence may be detected regardless of the physical condition (vapor, liquid, solid).
- Gaseous scintillators: The detection of the gaseous scintillators is based on the luminescence of noble gases, e.g., Ar, Xe, Ar-N₂, etc. The scintillator

is useful for heavy charged particles with high energies (greater than 100 MeV).

- Glass scintillator: To make a glass scintillator, the glass is doped or some special element for acting as the luminescent centers. Rare earth elements are widely doped into the glass as the luminescent centers. The rare earth elements have a characteristic energy level and provide different photon wavelengths.

2.4 Glass scintillators

In this section, we describe the composition of the scintillating glasses. The network former, modifier, and intermediate are the three main components. The typical network formers are also proposed for use in the glass fabrications. To become the scintillating glass, the luminescent centers doped in the glass were introduced in this section.

2.4.1 Fabrication of the glass

The glass can be synthesized using the glass material and the elements as the luminescent center. The glass material is based on the three categories: network formers, modifiers, and intermediates.

- Network former form a mostly cross-linked network of chemical bonds in the whole bulk of the glass. Various network formers can be made from many elements to be glass, such as silicate, borate, phosphate, germanate, aluminate, etc.
- Modifiers are added to the glass former in small chemical quantities to change the glass's properties. The added chemical can form with the cross-linked network former, reduce the relative number of strong bonds in the glass, or reduce the melting point and viscosity. There are alkaline metals and alkaline earth metals, for instance, lithium, sodium, potassium, calcium, barium, etc.
- Intermediates are chemical quantities that connect to the network formers to maintain structural continuity and glass properties. The chemicals used

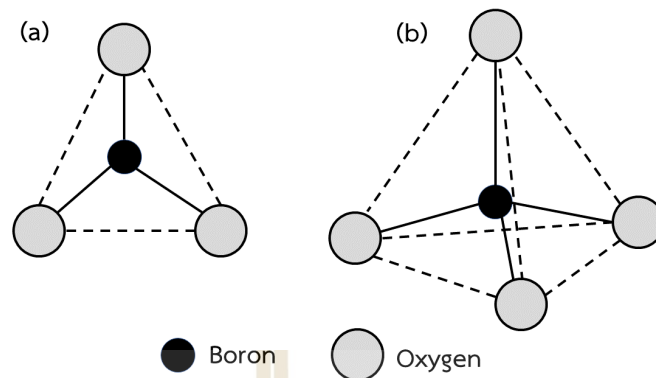


Figure 2.12 The structures of borate glass for (a) BO_3 -triangles and (b) BO_4 -tetrahedra.

to make the intermediates are almost entirely from the compound oxide family, such as aluminum oxide (Al_2O_3), zinc oxide (ZnO), barium oxide (BaO), titanium dioxide (TiO_2), lead oxide (PbO) etc. Furthermore, the small quantity of rare earth elements is doped into the glass to create a luminescent center.

2.4.2 Network former

Many glasses with different elements, such as silicate, borate, phosphate, germanate, and aluminate, have been suggested as network formers. In this section, we propose a common network former for the glass base.

- Borate: The borate glasses have been extensively studied. In the periodic table, boron is the first member of Group III, and the B^{3+} ion is very tiny. B^{3+} can occupy the trigonal space formed by three oxide ions in mutual contact and form a $[\text{BO}_3]$ -unit, as shown in figure 2.12. Because B in $[\text{BO}_3]$ is negatively charged ions (it has only six electrons in its outermost orbit in a covalent bound $[\text{BO}_3]$ -unit), it can take two extra electrons in the form of a locate bond. In borate glass structures, $[\text{BO}_4]$ -units can thus be easily formed. $[\text{BO}_4]$ -units are tetrahedral. Borate glasses are interesting as network formers due to their low melting points of 450°C and 510°C for trigonal and tetrahedral structures, respectively.

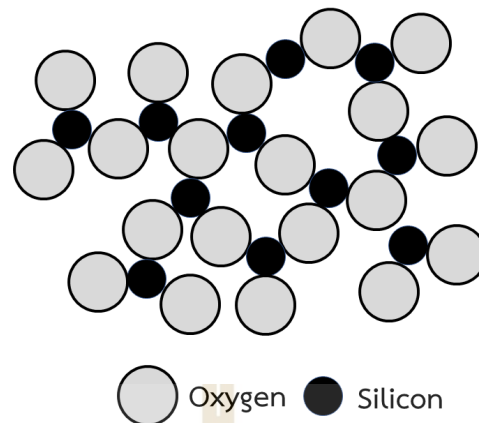


Figure 2.13 Schematic structure of the 2-dimension glass former.

- Silicate: The silicon atom with a coordinate number of four serves as the basic block for the silicon-oxygen tetrahedron. These tetrahedra are connected at continue all 4-corners with 3-dimensional network. Oxygen shares its two atoms of silicon at the center of the connected tetrahedra. Disorder of the structure can be found in the Si-O-Si angle in the connected tetrahedra. Moreover, rotation of the adjacent connected tetrahedra introduces the disorder structure. A 2-dimensional glass former of the silicate is presented in figure 2.13, where the fourth oxygen is directed above the small silicon.
- Phosphate: The structure of phosphoric oxide is also based on a tetrahedral block. Phosphorus, a pentavalent, has a phosphorus-oxygen tetrahedron with 4-bridging oxygens and a net positive charge of 1. While the other oxygens from BO are in the tetrahedron, a charged balance can occur. The connection makes a two-dimensional network that is tetrahedral at the three corners, just like boric oxide, but the blocks that connect them are tetrahedral with 4-corners.

2.4.3 Singlet and triplet states

As shown in Table 2.3, rare-earth elements were widely doped into the glasses to serve as the luminescent center. Different elements also provided different emission wavelengths and decay times, depending on their individual

characteristic quantum states. As referred to in the Jablonski diagram, there are two kinds of states, singlet and triplet states.

Singlet states are represented by a single spectral line, with all pairs being electrons. The net angular momentum of a singlet state is zero. On the other hand, the triplet state splits the spectral lines and consists of two unpaired electrons. Total net angular momentum is 1, allowing spin compositions of -1, 0, and +1.

In a singlet ground state, all electrons are paired, as shown in figure 2.14. The electrons in their excited state are still paired with their ground state due to the Pauli exclusion principle. On the other hand, in the triplet excited state, the electrons are not pairing with their electrons in the ground state (same spin of the electrons).

The light emitted as a result of excitation by incident radiation is known as fluorescence or phosphorescence. Fluorescence occurred due to the relaxation of the excited atoms or molecules to a lower energy state without a change in the electron spin. In contrast, the relaxation caused by changing the electron spin is called phosphorescence.

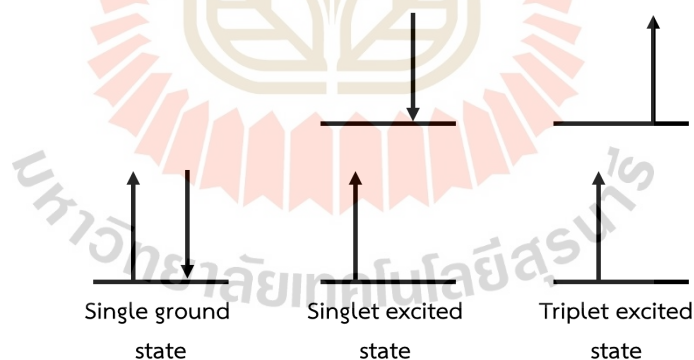


Figure 2.14 Ground and excited states for singlet and triplet states.

2.4.4 Luminescent center

Glass scintillators or scintillating glasses are fabricated by doping the glass with elements that have luminescent properties. In Table 2.3, some works successfully synthesized the glass, doping with rare-earth materials (RE). The

doped RE glass provided different emission wave lengths, and the decay time depended on the type of RE. The glasses doped with Ce, Pr, and Sm have the fastest decay times in nanoseconds compared to other RE. The Nd and Sm give the decay time in the range of microseconds. The luminescent centers of the glasses introduce the elements Eu, Tb, and Dy for a longer decay time (milliseconds).

Table 2.3 Example of doped lanthanide-earth element with emission wavelength and decay time (\mathcal{T}).

Elements	Emission wavelength (nm)	\mathcal{T}	References
Nd	1064	μs	(González M. et al., 2021)
Ce	380	ns	(Sun et al., 2015a) (Pan et al., 2020)
Pr	340, 600-850	ns	(Kamada et al., 2016) (Minami et al., 2019)
Sm	725 nm	ns, μs	(Dixie et al., 2014)
Eu	582, 595, 616, 654, 701	ms	(Zhao et al., 2019)
Tb	486, 540, 546, 582, 618	ms	(Tang et al., 2019)
Dy	482, 572, 663, 751	ms	(Rajagukguk et al., 2021)

2.5 Cyclotron

In this work, we use a proton cyclotron as a beam source for our experiment. This section proposes the fundamental proton cyclotron and describes the cyclotron machine at KCMH.

2.5.1 Physics of proton cyclotron

A proton cyclotron is a charged particle accelerator for high energies. The cyclotron structure consists of two hollow, semicircular electrodes, which are made of a non-ferromagnetic material and called “dees”. In figure 2.15, the dees are separated by a narrow gap and are applied by oscillating electric field under the magnetic field (B). The system is installed in a vacuum chamber between the magnet’s poles. Proton particles are separated from hydrogen gas

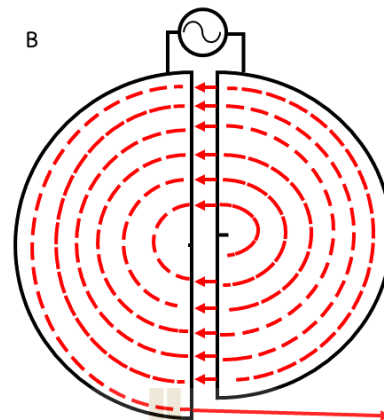


Figure 2.15 Top view of the schematic cyclotron. The dees are under magnetic field (B), perpendicular to the dees.

using a high voltage. The separated protons start at the middle of the dees and are accelerated under an electric field. The protons are moving in a circular path inside the dees under the magnetic field. The protons move out of the dees and accelerate under the electric field again. The accelerated protons move to another dees and continue their motion. Finally, when the protons have no more space to grow in the radius, they go out through the window. Due to circular moving path, centripetal force is considered in term of mass, velocity, and radius ($f_c = mv^2/r$). The radius (r) of the circular path of the charged particles is defined by Eq. (2.6):

$$r = \frac{mv}{qB} \quad (2.6)$$

Where m, v and q are representing to a mass, velocity, and charge, respectively. The speed of the particle is $v = rqB/m$. Therefore, the final non-relativistic kinetic energy is

$$K = \frac{1}{2}mv^2 = \frac{r^2q^2B^2}{2m} \quad (2.7)$$

The magnitudes of kinetic energy of the particle is depended the cyclotron radius and magnetic field.

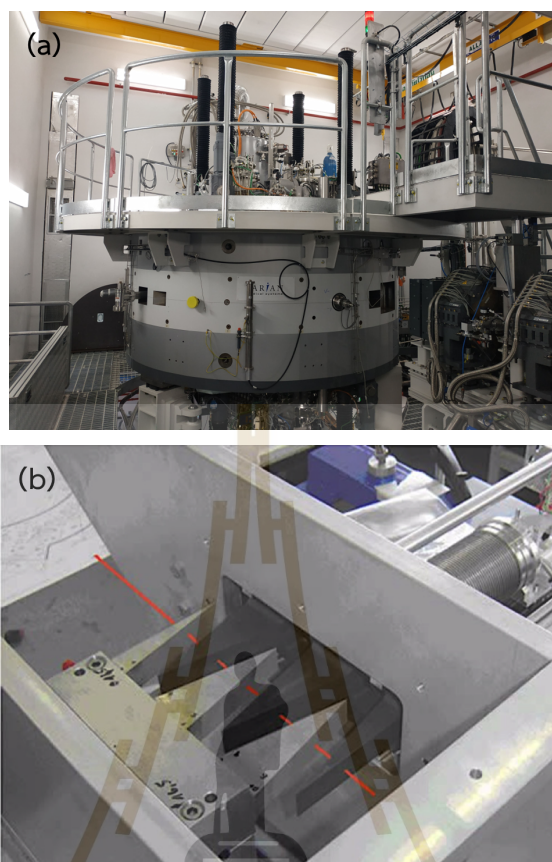


Figure 2.16 (a) The cyclotron of the KCMH proton center, and (b) energy selection, which reduces the proton energy from 250 MeV to a range of 70–230 MeV. The red line represents the 250 MeV beam direction from the cyclotron.

2.5.2 KCMH Proton Center

The proton center is located at Her Royal Highness Princess Maha Chakri Sirindhorn Proton Center, KCMH. The system to generate a proton beam is from the Varian ProBeam proton therapy system. The proton center has a compact single-room system with a 360-degree rotating gantry for treatment and research. The proton beam is accelerated by a cyclotron to 250 MeV of proton energy, as shown in figure 2.16(a). In cases of treatment or research, the proton energy is reduced to the requested energy by the energy selection system in figure 2.16(b). The energy selection system is made of two-multi wedge graphite that moves together to reduce proton energy in the 70-220 MeV range. Additionally, the character of the beam profile is the Gaussian beam, described in Appendix C.

CHAPTER III

GADOLINIUM ALUMINUM FLUOROBORATE SCINTILLATING GLASS

This section describes the glass synthesis processes used in this thesis and their properties. We study the gadolinium aluminum fluoroborate (GAF) glass by doping a small amount of CeF_3 as the luminescent center. The properties of the fabricated scintillating glasses, including, XANES, transmittance, optical band gap, photoluminescence, and X-ray induced luminescence, are presented. Finally, under X-ray radiation, the light emission properties of fabricated glasses are compared to those of a standard BGO scintillator.

3.1 Introduction

Proton-computed tomography (pCT) is a medical 3D-imaging technique that utilizes a proton beam with energies of up to 250 MeV to penetrate the human body and determine stopping power distributions throughout the tissue volume. This technology is compatible with proton therapy and is undergoing global development at the present time (Bashkirov et al., 2016; Civinini et al., 2013; Scaringella et al., 2013; Saraya et al., 2014; Schulte et al., 2004). The current architecture of pCT requires a unique calorimeter that can precisely measure the residual energy of the scattered protons. This component comprises of a single array or numerous arrays of crystal scintillators, which convert proton-induced charged particles into scintillation light. Photomultipliers or large-area photodiodes subsequently collect the emitted photons (Scaringella et al., 2013; Schulte et al., 2004). The development of highly efficient calorimeters requires scintillating materials with a high density, fast decay times, and high light yields. For pCT calorimeters, various crystal scintillators have been proposed, such as Ce-doped lutetium LSO (Schulte et al., 2004), YAG:Ce (Civinini et al., 2013; Scaringella et al., 2013) NaI(Tl) (Saraya et al., 2014), and CsI(Tl) (Bashkirov et al., 2016). Scintillating glasses are a feasible alternative to crystal scintillators due to their advantageous properties, such as low cost, radiation absorption capability, ease of manufacture in a variety of sizes and forms, and stability in a normal atmosphere.

Rare earth (RE) elements are widely utilized as glass compounds to improve glass's scintillating properties. Some RE elements are thought to be luminescence centers in glass, emitting ultraviolet, visible, and near-infrared photons. Furthermore, some of them can boost emission intensity by transferring energy to suitable luminescence centers. High-density scintillating glass is required for calorimeter applications in particle therapy to enhance the stopping power of energetic particles in the scintillator with short decay times to avoid redundancy of the incoming particles. High-Z elements, such as Gd-doped with lanthanide earth elements as luminescence centers, can be used to synthesize significant scintillating glasses (Sun et al., 2014b). Numerous scintillation investigations have demonstrated that cerium is an excellent luminous center due to its nanosecond-scale decay time (Chewpraditkul et al., 2011; Pan et al., 2020; Rajaramakrishna et al., 2020; Shi et al., 2020; Sontakke et al., 2016; Sun et al., 2014b; Sun et al., 2017), and high radiation hardness (Pan et al., 2020; Wang et al., 2003).

According to previous research on scintillating glasses used to determine the residual energy of pCT, a series of Eu-doped $\text{Gd}_2\text{O}_3\text{-WO}_3\text{-B}_2\text{O}_3$ glasses can be utilized to detect incident protons by measuring the light emitted by these glasses (Wilkinson et al.,). Nevertheless, Ce doping of scintillating glasses is regarded as more desirable due to its advantageous properties for pCT calorimeters. A higher concentration of Ce^{3+} in the glass providing convenient photoluminescence (PL) in investigations involving Ce doping (Sun et al., 2014b; Sun et al., 2017). Cerium fluoride (CeF_3), an inorganic molecule, was chosen as the dopant Ce rather than the conventional cerium oxide (CeO_2) because CeF_3 exhibits a higher ratio of Ce^{3+} to Ce^{4+} than CeO_2 (Sun et al., 2015a). Conversely, a low ratio of Ce^{3+} to Ce^{4+} in the glass generates a large X-ray-induced scintillation light yield (Masai et al., 2018). Consequently, the objective of this study was to examine the scintillation properties of gadolinium aluminum fluoroborate (GAF) glass by adjusting the concentration of CeF_3 . According to the desired applications, the fabricated scintillating glasses exhibited emission spectra with X-ray-induced luminescence (XIL).

3.2 Material and method

3.2.1 scintillating glasses synthesis

The GAF scintillating glasses $25\text{Gd}_2\text{O}_3-(65-x)\text{B}_2\text{O}_3-10\text{AlF}_3-x\text{CeF}_3$ (where $x = 0.0, 0.05, 0.1, 0.2, \text{ and } 0.3 \text{ mol\%}$) were synthesized using the melt quenching method in an air atmosphere. In alumina crucibles, a precise stoichiometric ratio of high-purity chemicals, including CeF_3 , gadolinium oxide, boric acid, and aluminum fluoride, were mixed. The mixture were then melted for 3 hours at $1400 \text{ }^\circ\text{C}$ in a high-temperature furnace. The melt was poured over a preheated graphite plate and annealed at $500 \text{ }^\circ\text{C}$ for 3 hours to decrease stress and prevent samples from cracking. As indicated in figure 3.1, the samples were cut and polished to obtain samples with dimensions of $10 \times 15 \times 3 \text{ mm}^3$.

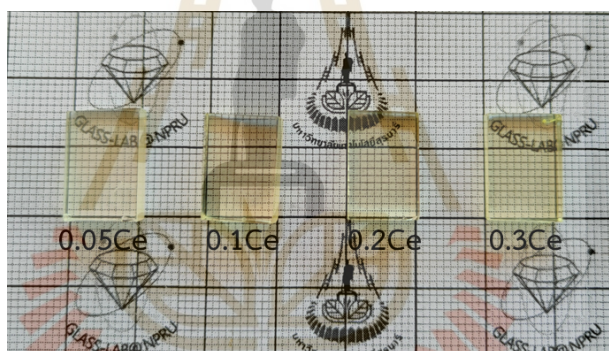


Figure 3.1 Image of the fabricated scintillating glasses, $25\text{Gd}_2\text{O}_3-(65-x)\text{B}_2\text{O}_3-10\text{AlF}_3-x\text{CeF}_3$ (where $x = 0.05, 0.1, 0.2, \text{ and } 0.3 \text{ mol\%}$).

3.2.2 Characterizations

A density of the fabricated glasses was measured employing Archimedes' principle using a 4-digit sensitive microbalance (AND, HR-200). XANES was employed to analyze the oxidation state of the Ce doping atom. The XANES spectra were collected at the BL5.2:SUT-NANOTEC-SLRI XAS beamline in Thailand's Synchrotron Light Research Institute (SLRI) using an electron energy of 1.2 GeV . The Ce L_{III} -edge XANES profiles were acquired with a spectral resolution of 0.3 eV in the fluorescence mode over for an energy range of $5693\text{--}5803 \text{ eV}$. The transmittance spectra in the $200\text{--}800 \text{ nm}$ region were obtained using ultraviolet

spectroscopy (Cary 50 UV-Vis spectrophotometer) in fluorescence mode. The excitation and emission spectra were obtained with a Cary Eclipse fluorescence spectrophotometer (Agilent Technologies) linked with a Xe flash lamp. Using a DeltaPro fluorescence lifetime system, the decay time was determined. In addition, the X-ray-induced luminescence was determined using a Cu target as an X-ray source at an applied voltage of 50 kV and an emission current of 30 mA, with the emitted light getting recorded by a spectrometer (QE65 Pro, Ocean Optics). The samples of bismuth germanate (BGO) scintillator were compared to those of the fabricated scintillating glasses at room temperature (25 °C).

3.3 Results and discussion

3.3.1 Physical properties

Figure 3.1 shows images of the constructed CeF₃-doped GAF scintillating glasses. Table 3.1 lists the density of the manufactured scintillating glasses. The density of the un-doped glass or the host glass with 25% mol% Gd is the same as that of a conventional borate glass (4.24 g/cm³). The density increased to 4.29-4.31 g/cm³ after doping the host glass with CeF₃ at concentrations ranging from 0.05 to 0.3 mol%. The rise in density indicates that the Ce³⁺-doped glass samples are compact. This density increase could be attributed to the glass formula's replacement of CeF₃ with B₂O₃. According to previous work, the densities of CeF₃ (6.16 g/cm³) are greater than those of B₂O₃ (2.46 g/cm³) (Zaman et al., 2017).

Table 3.1 Glass properties, density (ρ), absorption edge of the transmittance spectra, indirect of the optical band gap (E_g), decay time, and light yield which is compared to that of standard BGO scintillator.

Samples	ρ (g/cm ³)	Absorption edge (eV)	Indirect E_g (eV)	Decay time (ns)	Light yield compared to BGO (%)
0.05Ce:GAF	4.29	3.59	3.19	23.30	4.36
0.1Ce:GAF	4.30	3.47	3.12	24.52	5.22
0.2Ce:GAF	4.30	3.41	3.05	22.73	1.73
0.3Ce:GAF	4.31	3.32	2.89	21.24	1.34

3.3.2 XANES

The spectra of Ce L_{III} -edge XANES are presented in figure 3.2, along with the spectra of the reference compounds CeF_3 and CeO_2 . A clear peak of trivalent Ce (CeF_3 - Ce^{3+}) is observed in the spectra of the reference samples at 5727 eV, corresponding to the 5d-4f transition of CeF_3 . The tetravalent Ce (CeO_2 - Ce^{4+}) on the other hand, reveals a double peak at 5731 and 5737 eV, which can be attributed to the 2p-5d transition (Rajaramakrishna et al., 2020). The peak shapes corresponding to all of these glasses (represented by a single peak) are the same as those of the CeF_3 profile, as illustrated in figure 3.2. In addition, the CeF_3 doped in the glass samples was determined to be in the Ce^{4+} oxidation state, as shown by the second peak (5737 eV) in the spectra, which corresponds to the CeO_2 state (Sun et al., 2017). Thus, the coexistence of Ce ions with two valence states in the GAF glasses is validated based on the two observed Ce states in the doped glasses.

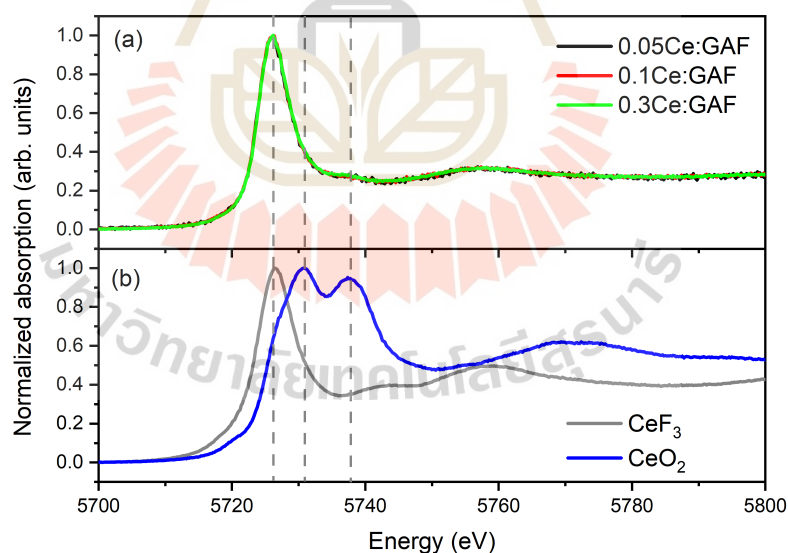


Figure 3.2 Ce L_{III} -edge XANES profiles of the (a) fabricated scintillating glasses and (b) CeF_3 and CeO_2 standards.

3.3.3 Transmittance and optical band gap

The transmittance spectra of the fabricated scintillating glasses in the region of 200-800 nm are presented in figure 3.3(a). The linear transmittance percentage for the undoped host glass exceeds 78 % in the 450-800 nm region, with a value of 72 % for the Ce^{3+} -doped scintillating glasses. When the concentration of CeF_3 increases, the transmittance percentage drops. Furthermore, as the concentration of Ce^{3+} increases, the cut-off absorption edge of the transmittance shifts from 345 to 374 nm (320 nm for an undoped sample). The optical band gap (E_g) can be estimated using Eq. (3.1)

$$E_g = \frac{1240}{\lambda_{\text{cut-off}}} \quad (3.1)$$

where $\lambda_{\text{cut-off}}$ is the optical absorption cut-off edge. The results are shown in Table 3.1. When the Ce concentration was increased, the optical band gap dropped in the range of 3.59-3.32 eV. Tauc's relation can be used to accurately determine the energy gap, as demonstrated in Eq. (3.2).

$$\alpha h\nu = [A(h\nu - E_g)]^r \quad (3.2)$$

where α and $h\nu$ represent the absorption coefficient and photon energy, respectively, and $r = 2$ for amorphous materials (Sun et al., 2015b). When we set $E_g = 0$ in Eq. (3.2), we get the plots between $\alpha h\nu^{1/2}$ and $h\nu$, as illustrated in figure 3.3(b). Table 3.1 provides the calculated indirect band gaps. The indirect band gap reduces from 3.19 to 2.89 eV as Ce concentration increases. These findings are in agreement with previous research, which found an indirect optical band gap of around 3.2 eV even in Ce-doped hosts, such as $\text{B}_2\text{O}_3\text{-GeO}_2\text{-Gd}_2\text{O}_3\text{-CeO}_2\text{-MgO}$ (Sun et al., 2015a), $\text{Na}_2\text{O-Gd}_2\text{O}_3\text{-Al}_2\text{O}_3\text{-P}_2\text{O}_5\text{-CeF}_3$ (Wantana et al., 2018), and $\text{Gd}_2\text{O}_3\text{-CaO-SiO}_2\text{-B}_2\text{O}_3\text{-CeF}_3$ (Rajaramakrishna et al., 2020).

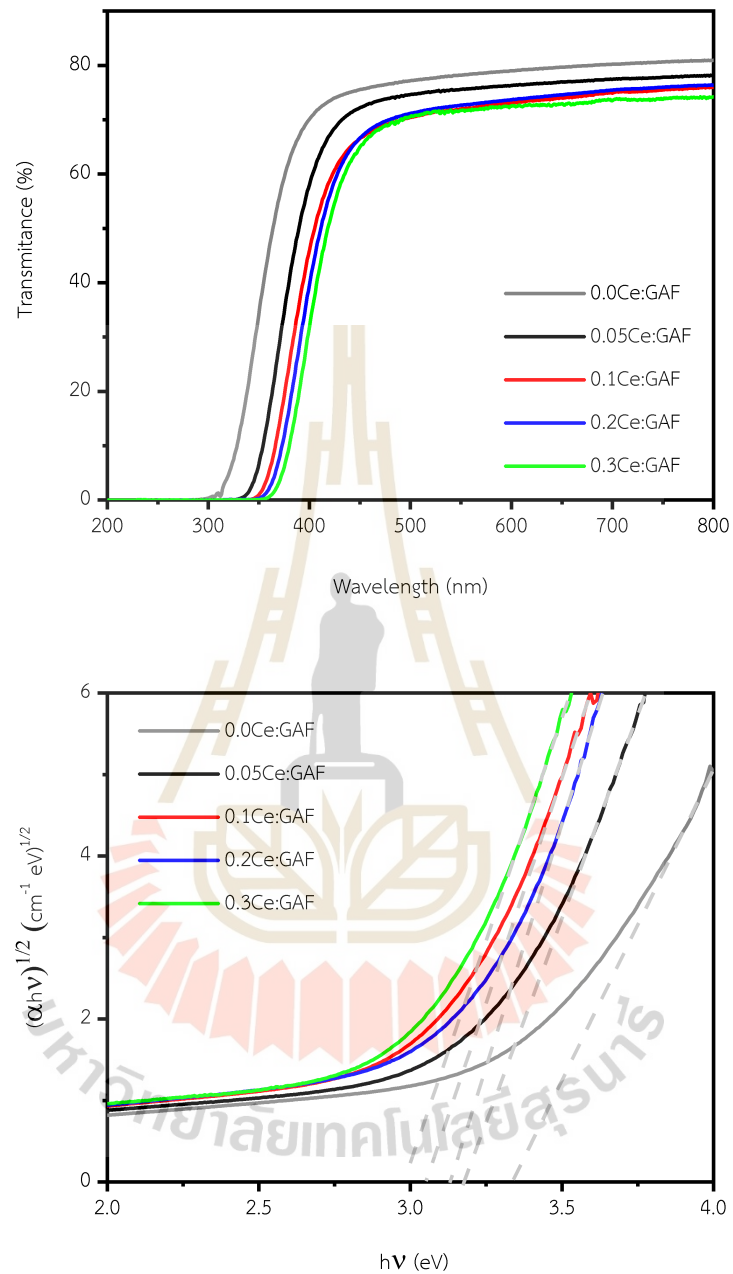


Figure 3.3 (a) Transmittance spectra of the fabricated scintillating glasses and (b) indirect optical band gap plotted from Tauc's relation. The dashed lines are drawn based on the calculated edge from Tauc's relation, indicating the optical band gap.

3.3.4 Photoluminescence

Figure 3.4 illustrates the PL emission and excitation spectra of the fabricated scintillating glasses. Due to a single peak of the Ce^{3+} transition in the emission spectra, the excitation spectra were obtained at an emission wavelength (λ_{Em}) of 360 nm. The spectra of the host glass without Ce^{3+} doping showed two broadenings at 236 (Gd^{3+}) and 266 nm (Gd^{3+}). Three distinct broadbands were detected for the Ce^{3+} -doped scintillating glasses at 247 (Gd^{3+}), 275 (Gd^{3+}), and 320 nm (Ce^{3+}) (Fu et al., 2003; Wang et al., 2013). This result suggests that doping the host with Ce^{3+} can change the state of Gd^{3+} ions from an undoped energy level. According to the excitation spectrum, electrons in the ground state of Ce^{3+} can be attributed to the 4f-5d transition of its state and the excited state of Gd^{3+} (Sun et al., 2014b; Sun et al., 2015a). The emission spectra of the fabricated scintillating glasses, as shown in figure 3.4, exhibited an emission band centered at 360 nm under a direct excitation wavelength (λ_{Ex}) of 312 nm. This band is attributed to the Ce^{3+} due to 5d-4f transition (Pan et al., 2020; Shi et al., 2020; Sun et al., 2017; Sun et al., 2015b; Wang et al., 2013). Furthermore, the two small emission bands at 490 and 520 nm may be associated to the $5d-{}^2F_{5/2,7/2}$ transition, which resulted from doping with Gd^{3+} and Ce^{3+} (Sun et al., 2020a; Wantana et al., 2018). The 0.1Ce:GAF sample has the strongest emission and excitation bands. This data reveals that at a CeF_3 concentration of 0.1 mol%, the host doped with Ce exhibits considerable quenching.

According to the Ce^{3+} oxidation of doped scintillating glasses, raising the concentration of trivalent Ce can improve the PL intensity (Sun et al., 2014b; Sun et al., 2017). However, a study on the coexistence of Ce^{3+} and Ce^{4+} oxidation revealed that the Ce^{3+} state can increase PL intensity, whereas the glass containing Ce^{4+} state can increase X-ray-induced luminescence intensity (Masai et al., 2018). Although the varied ratios of Ce oxidation from the doped scintillating glasses could not be demonstrated in this study, the coexistence of Ce^{3+} and Ce^{4+} observed by XANES is expected to influence the emission mechanism.

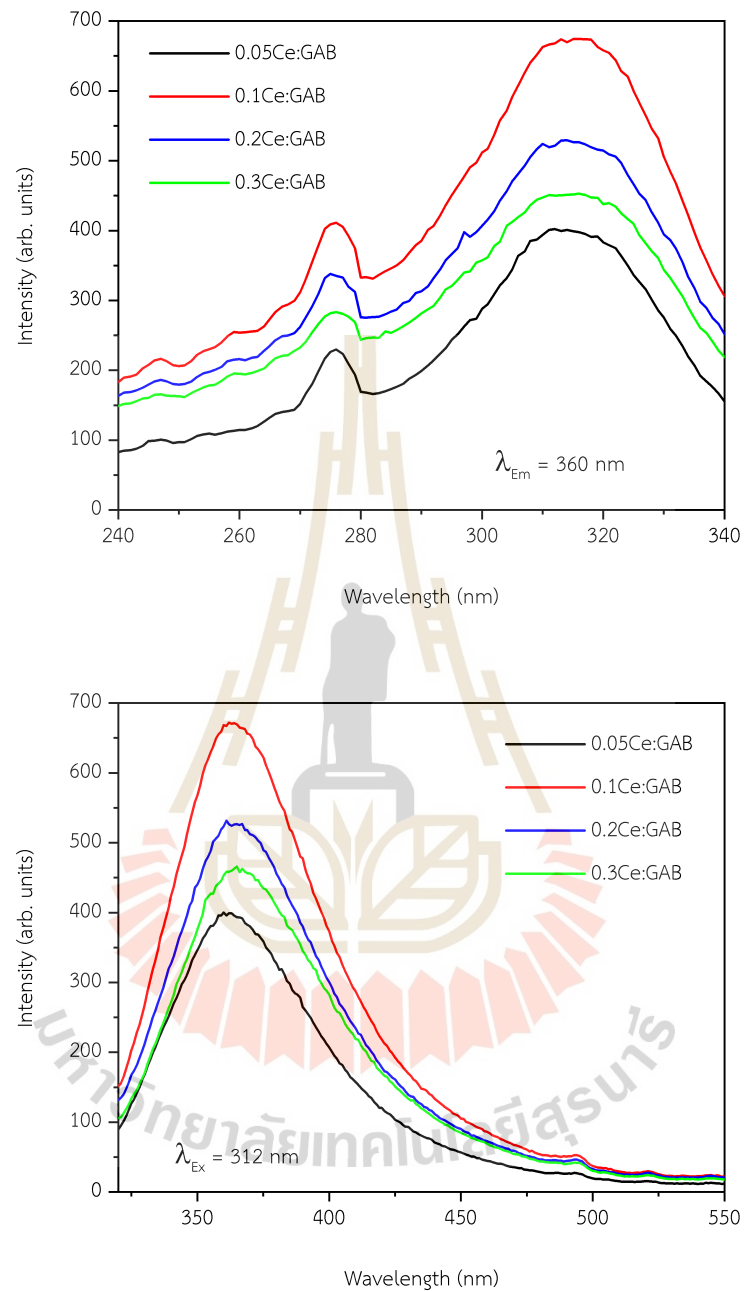


Figure 3.4 (a) Excitation spectra ($\lambda_{em} = 360 \text{ nm}$) and (b) emission spectra ($\lambda_{ex} = 312 \text{ nm}$) of the fabricated scintillating glasses.

3.3.5 Decay time

Figure 3.5 shows the decay time of the fabricated scintillating glasses at an emission wavelength of 360 nm and an excitation wavelength of 312 nm.

The decay counts demonstrate that the decay time curve deviated significantly from the single exponential behavior. Eq. (3.3) was used to fit the decay time.

$$A(t) = Ae^{-\frac{t-t_0}{\tau}} \quad (3.3)$$

where $A(t)$ is the count as a function of time, τ is the decay time, and A is the time component's amplitude. Table 3.1 shows the determined decay times of all the fabricated scintillating glasses. The decay time range is in line with previous studies on various Ce^{3+} -doped scintillating glasses (Shi et al., 2020; Sun et al., 2017; Wang et al., 2013) where the decay time was always in the nanosecond range. This short decay time demonstrates that the fabricated glass samples can be used in proton calorimeter or medical applications that require a short decay time to avoid signal redundancy from incoming particles.

3.3.6 X-ray-induced luminescence

In figure 3.6, the x-ray-induced luminescence spectra of the fabricated scintillating glasses in the region of 300-800 nm are displayed in comparison to the BGO scintillator. The observed emission peak is comparable to the PL emission spectra owing to 5d-4f transition of Ce^{3+} (Sun et al., 2017; Wantana et al., 2018). For low doped concentration, a broad emission band in the 350-600 nm range was centered around 400 nm. Furthermore, as the concentration of Ce^{3+} in 0.3Ce:GAF increased, the emission center shifted to longer wavelengths. This confirms a previously observed shift in the optical band gap (Park et al., 2016). The light yield of the scintillating glasses was estimated by integrating the emission spectra from 350 to 800 nm. In comparison to the standard BGO scintillator, the results are provided in Table 3.1. When compared to the BGO scintillator, the greatest light yield obtained from the 0.1Ce:GAF sample was only 5.22 %. When the concentration of Ce^{3+} was increased, the light yield of the fabricated scintillating glasses decreased.

3.4 Summary

In this study, CeF_3 -doped GAF glasses were successfully fabricated using quenching techniques. The density of the fabricated scintillating glasses ranged

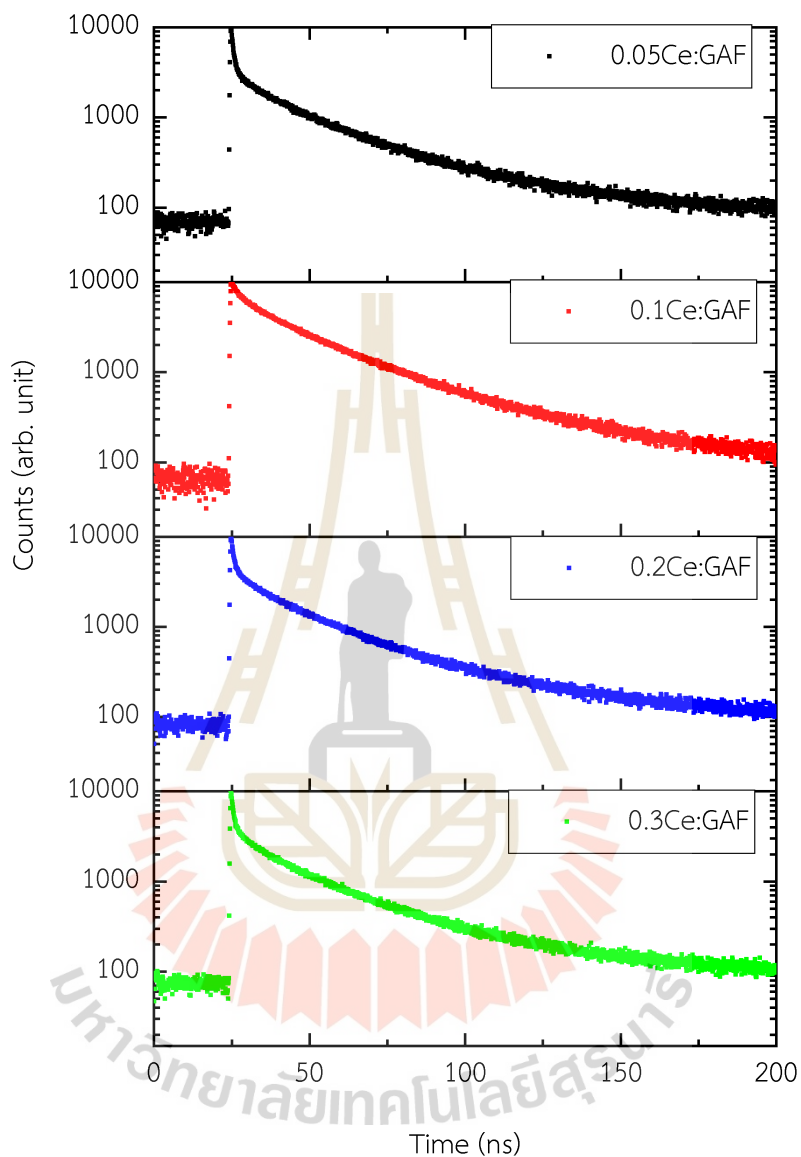


Figure 3.5 Luminescence decay time measurements of the fabricated scintillating glasses.

between 4.24 and 4.31 g/cm³, and XANES spectra revealed the coexistence of Ce³⁺ and Ce⁴⁺ oxidation states. These glasses displayed PL spectra with Gd and Ce states with decay times ranging range 21.24 to 24.52 ns. Under X-ray irradiation, the GAF glasses emitted visible light. Because of its short decay time,

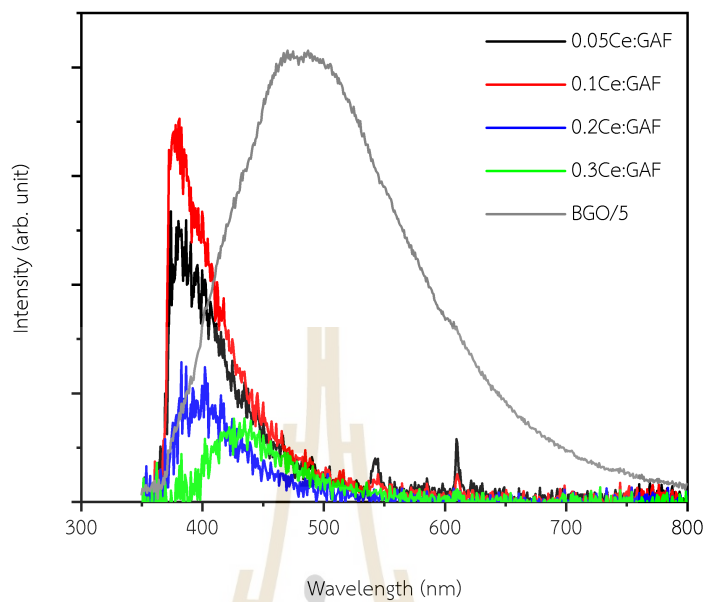


Figure 3.6 X-ray-induced luminescence spectra of the fabricated scintillating glasses compared to that of the standard BGO scintillator. The BGO spectrum is scaled down by a factor of 5.

it is possible to be used in some medical applications.

CHAPTER IV

GADOLINIUM BARIUM FLUOROBORATE SCINTILLATING GLASS

This chapter describes the doping of a high-Z element, barium-56, into the fabricated scintillating glass. We study the previous host by doping the barium oxide (BaO) to be the glass with CeF₃ for the luminescent center. The synthesis methodologies for the scintillating glass are the same as in the previous chapter. The glass properties, including transmittance, photoluminescence (PL), XANES, and radioluminescence, are presented. Also, the fabricated scintillating glasses are compared to the standard BGO scintillator for x-ray detection.

4.1 Introduction

Cerium (Ce), a 58-lanthanide earth element, is still interesting in this section because of its luminescent center, which provided fast decay times in the nanosecond range (Pan et al., 2020; Rajaramakrishna et al., 2020; Sun et al., 2020a; Sun et al., 2020b; Sun et al., 2017). Furthermore, barium can increase glass density as well as improve optical characteristics and gamma-ray shielding (Kaewjaeng et al., 2012). In this work, we develop a glass scintillator based on the doping of cerium on gadolinium-barium-fluoroborate (GBF) glasses.

We aim to determine the depth-dose profile of the proton beam by the fabricated glass. The relationship between the Ce-oxidation state and scintillation is investigated by fabricating glasses with different Ce and Ba concentrations to study scintillating glass properties. Also determined are x-ray-induced luminescence (XIL).

4.2 Materials and Methodologies

4.2.1 Glass scintillator synthesis

The gadolinium-barium-fluoroborate (GBF) scintillating glasses with the molecular formula $20\text{Gd}_2\text{O}_3-(80-x-y)\text{B}_2\text{O}_3-x\text{BaO}-y\text{CeF}_3$ (where $x = 10, 20,$ and 30 mol%, and $y = 0.1, 0.5, 1.0,$ and 1.5 mol%) were successfully synthesized in an

air atmosphere using melt-quenching technique. Glasses were prepared in alumina crucibles and melted for 3 hours in a high-temperature furnace at 1,400 °C. The glasses were then annealed at 500 °C for 3 hours to reduce stress. Finally, the glasses were cut and polished to $10 \times 15 \times 3 \text{ mm}^3$ dimensions, as seen in figure 4.1.

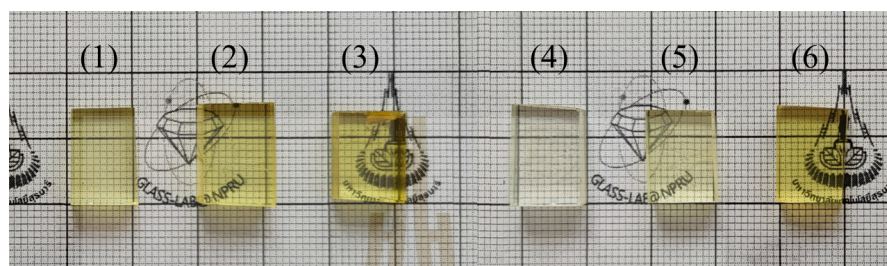


Figure 4.1 Image of the fabricated scintillating glass, including (1) B10GF:Ce1.0, (2) B20GF:Ce1.0, (3) B30GF:Ce1.0, (4) B10GF:Ce0.1, (5) B10GF:Ce0.5, and (6) B10GF:Ce1.5.

4.2.2 Characterizations

The glass density was calculated using Archimedes' principle and measured the weight by a 4-digit sensitive microbalance (AND HR-200). XANES spectra were used to determine the oxidation state of cerium doped glasses at the Synchrotron Light Research Institute (SLRI) in Thailand, utilizing a Beamline 5.2: SUT-NANOTEC-SLRI XAS. Ce LIII-edge XANES spectra were observed using XANES spectroscopy in the fluorescence mode in the energy range of 5693-5803 eV. Linear combination fitting (LCF) was performed with Athena software to analyze the concentration of cerium oxidation state (Ravel and Newville, 2005). Transmittance spectra obtained using a UV spectroscopy Cary 50 in fluorescence mode were observed in the 200-800 nm region. The excitation and emission spectra of the glasses treated with a xenon flash lamp for PL were displayed using a Cary Eclipse fluorescence spectrophotometer (Agilent Technologies) (PL). XIL presented the emission spectra observed using a spectrometer utilizing a copper target treated at 50 kV and 30 mA. (QE65 Pro, Ocean Optics).

4.3 Results and Discussion

4.3.1 Transmittance and optical band gap

Table 4.1 shows the chemical compositions of GBF glasses doped with various CeF_3 and BaO concentrations. The results reveal that when the concentrations of CeF_3 and BaO in the doped glasses grow, so does their density. The transmittance spectra of Ce-doped GBF glasses in the 300-800 nm range are depicted in figure 4.2(a). When the glasses are doped with increasing concentrations of CeF_3 and BaO, the cutoff UV absorption edge shifts to a longer wavelength (redshift). Tauc's relation by Eq. (3.2) may be used to measure the energy gap value of the glasses (Mott et al., 1975).

Figure 4.2(b) illustrates the Tauc's plot results for each glass sample. Table 4.1 demonstrates the measurement of E_g for each sample based on the calculations. When the Ce concentration in the glasses is increased, the band gap reduces from 3.28 to 2.76 eV. The presence of Ce^{3+} in the glass matrix reduces the band gap and shows a redshift (Sontakke et al., 2016; Xu et al., 2018). In the comparison of glasses with different BaO concentrations, the band gap decreases from 2.91 to 2.77 eV, which is consistent with the existence of Ce^{3+} in the glass samples. A increase in E_g corresponds directly to a decrease in metal-oxygen bond strength, indicating the formation of non-bridging oxygen in the glass structure. When BaO concentration increases, the conversion of the host glass structure could increase electron localization and result in a decrease in E_g .

4.3.2 Photoluminescence

Figure 4.3 illustrates the PL excitation and emission spectra at different CeF_3 and BaO concentrations. Two broad bands in the 270-280 and 280-330 nm wavelength regions are observed in the excitation spectra of figure 4.3 due to the characteristic absorption transitions of the Ce^{3+} state from the 4f level to the excited state of Gd^{3+} and its 5d excited state, respectively (Sun et al., 2017; Masai et al., 2018; Sun et al., 2014b; Wang et al., 2013). In 4.3, the emission spectra of the 4f5d transition of CeF_3 are observed with a single broad band in the region of 325-450 nm, which was a transition itself. This band was a contribution from the 5d-4f transition Ce^{3+} , as indicated by previous

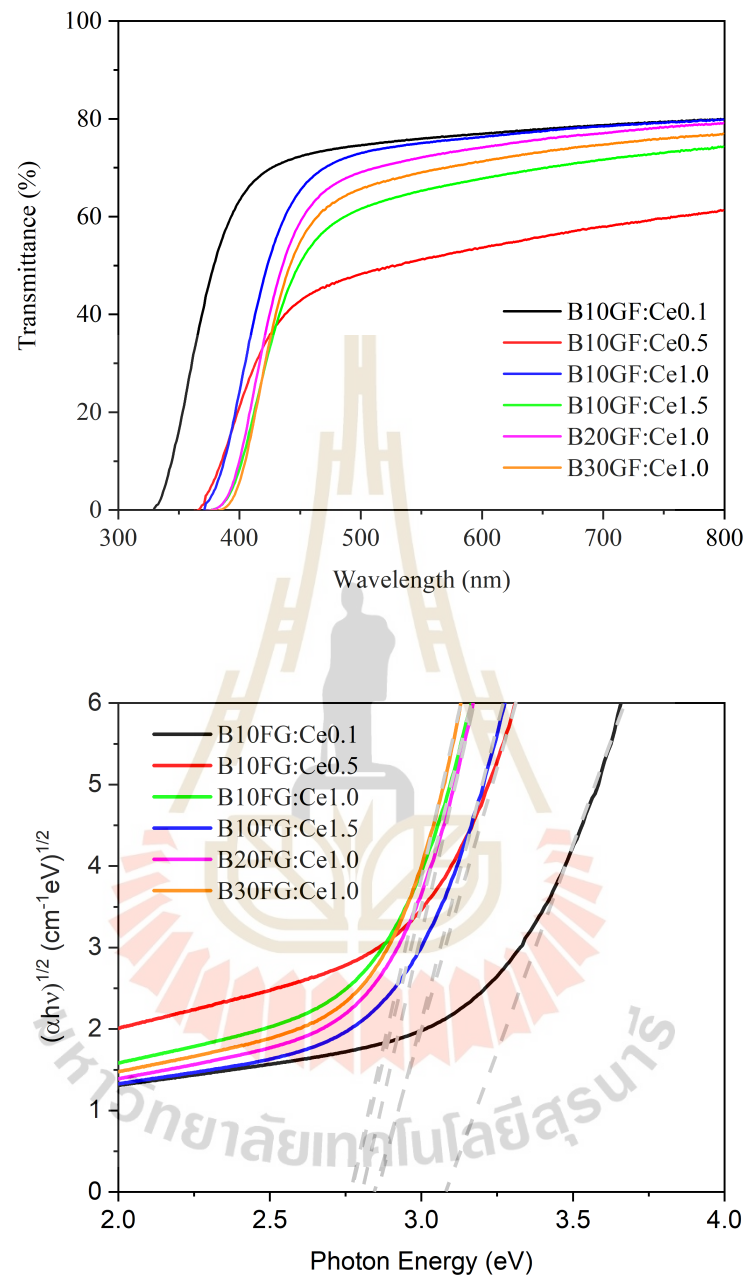


Figure 4.2 (a) Transmittance spectra and (b) Tauc's plot as a function of photon energy of doped GBF glasses.

references (Pan et al., 2020; Sun et al., 2017; Sun et al., 2015b; Wang et al., 2013; Shi et al., 2020). In the CeF_3 concentration measurement, the B10GF:Ce0.5 glass has the highest intensity. The excitation spectra, on the other hand, reveal

Table 4.1 Properties, including the density, absorption edge of transmittance, and emission light yield of RL, compared to those of BGO. The chemical composition of $20\text{Gd}_2\text{O}_3-(80-x-y)\text{B}_2\text{O}_3-x\text{BaO}-y\text{CeF}_3$ is defined by the different BaO (x) and CeF_3 (y) concentrations.

Glasses	BaO (x) (mol%)	CeF_3 (y) (mol%)	Density (g/cm^3)	Absorption edge (nm)	Light yield compared to BGO (%)
B10GF:Ce0.1	10	0.1	3.95	331	4.71
B10GF:Ce0.5	10	0.5	4.01	367	5.42
B10GF:Ce1.5	10	1.5	4.00	394	6.55
B10GF:Ce1.0	10	1	3.94	377	6.19
B20GF:Ce1.0	20	1	4.15	390	2.30
B30GF:Ce1.0	30	1	4.29	396	2.19

that increasing the CeF_3 concentration to 1.5 mol% removes the state of Gd^{3+} . The concentration of BaO in the doped glasses clearly reduces the intensity. Furthermore, as illustrated in figure 4.3, increasing the BaO concentration reduces the Gd^{3+} state of the excitation spectra and slightly shifts the emission peak.

4.3.3 X-ray induced luminescence

Figure 4.4 illustrates the x-ray induced luminescence (XIL) spectra of Ce^{3+} -doped scintillating glasses. XIL emission spectra clearly indicate a broad band in the 375-550 nm region, which is correlated to the PL with the Ce^{3+} transition. The light yield was calculated by integrating the emission spectra in the wavelength range 350-800 nm and comparing it to that of a standard BGO scintillator with a centered emission wavelength of 480 nm. The results are shown in Table 4.1, which shows the light yield of the doped glasses at different concentration of CeF_3 and BaO. The emitted light yield decreases as the BaO concentration in the doped glass increases. Furthermore, increasing the concentration of Ce^{3+} shifts the emission spectra by increasing the cutoff absorption edge in the transmittance spectra (Park et al., 2016). When considering the Ce L_{III} -edge XANES, PL, and XIL spectra, we reach the conclusion that glass with a high fraction of Ce^{3+} to Ce^{4+} causes a reduction in PL intensity and high light yield in the XIL spectra (Sun et al., 2017; Sun et al., 2014b). Higher

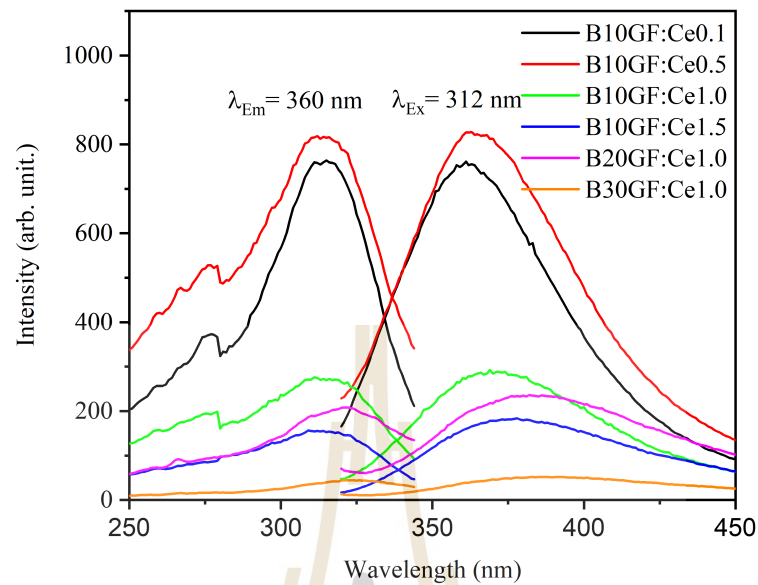


Figure 4.3 Excitation and emission spectra of Ce-doped GBF glasses.

BaO concentration reduce scintillation intensity in the PL and XIL spectra, as illustrated in figures 4.3 and 4.4.

4.3.4 XANES

The spectra of Ce L_{III} -edge XANES were measured. The cerium oxidation states of the glasses are compared to those of CeF_3 as a trivalent cerium (Ce^{3+}) and CeO_2 as a tetravalent cerium (Ce^{4+}) in figure 4.5. The Ce^{3+} state has a single peak at 5727 eV, whereas the Ce^{4+} state has two peaks at 5731 and 5737 eV (Sun et al., 2017; Ranasinghe et al., 2019). In response to the concentration change, the white line shifts. The shapes of the CeF_3 -doped glasses are similar to the shapes of normal CeF_3 glasses. The investigation of the rise of doped BaO, on the other hand, indicates an increasing broad band at around 5737 eV, which is attributable to the second peak of the Ce^{4+} state. The R-factor correlated with the LCF method is defined as follows to evaluate

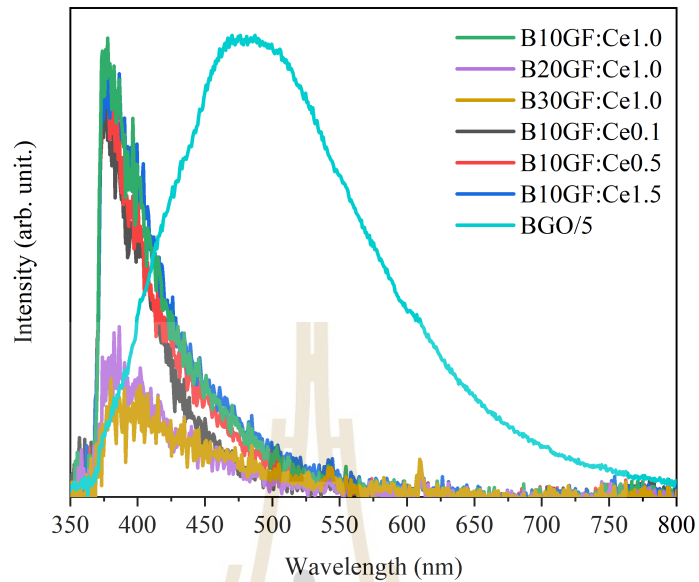


Figure 4.4 RL spectra of the Ce-doped GBF glasses.

the fitting oxidation state using Eq. (4.1)

$$R \text{ - factor} = \frac{\sum (\text{data} - \text{fit})^2}{\sum (\text{data})^2} \quad (4.1)$$

where the R-factor is calculated based on the observed data and the fitted value. According to the LCF data reported in Table 4.2, a low dopant concentration resulted in a low Ce^{3+} oxidation state in B10GF:Ce. However, the highest Ce doping concentration, 10GF:Ce1.5, provides a higher Ce^{3+} concentration and a low Ce^{4+} state. As a result, increasing the CeF_3 concentration raises the fraction of Ce^{3+} and Ce^{4+} oxidation states. However, as the BaO concentration increases, the fraction of the Ce^{3+} and Ce^{4+} oxidation states decreases. We can conclude that glasses with a high CeF_3 (1 mol%) and a low BaO (10 mol%) content have a high Ce^{3+} oxidation state. The doped glass can provide emission light under x-ray radiation due to its high Ce^{3+} oxidation state (Sun et al., 2017; Sun et al., 2014b).

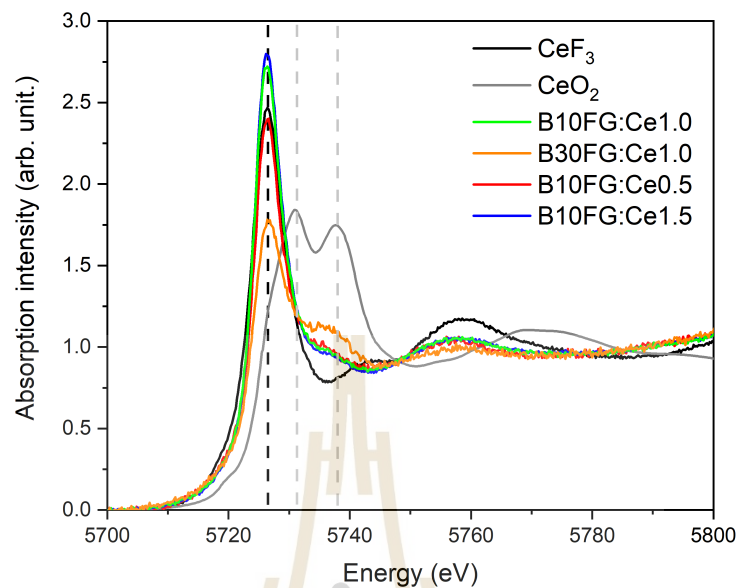


Figure 4.5 The Ce L_{III} -edge XANES spectra of GBF glasses doped at different Ce concentration and the reference spectra of CeF_3 and CeO_2 .

4.4 Summary

We successfully synthesized the GBF glasses using melt-quenching techniques. The properties of the glasses, including transmittance, PL, XANES, and x-ray induced luminescence (XIL), depth-dose profile were all measured. The Ce^{3+} valence state increased with increasing CeF_3 concentration, while the fraction of Ce^{3+} reduced with increasing BaO fraction in the glasses. The PL spectra revealed that B10GF:Ce0.5 had the highest excitation and emission spectrum intensity. In the x-ray-induced property, the B10GF:Ce1.5 with the highest CeF_3 concentration provided the best light yield. As a result, the glasses doped with a high concentration of CeF_3 and a low concentration of BaO generated the highest x-ray light yield.

Table 4.2 Fraction of the cerium oxidation state calculated using the LCF method.

Glasses	R-factor	Ce ³⁺	Ce ⁴⁺
B10GF:Ce0.5	0.015	0.845	0.155
B10GF:Ce1.5	0.026	0.979	0.021
B10GF:Ce1.0	0.022	0.950	0.050
B30GF:Ce1.0	0.016	0.604	0.396

CHAPTER V

DEPTH-DOSE PROFILE

The purpose of this chapter is to determine the depth-dose profile of a proton beam measured by fabricated scintillating glasses with varying absorber thicknesses. This chapter describes the development of the measurement setup at the KCMH proton center. The first setup employs stacked virtual water phantoms (VWP) as the absorber thickness and scintillating glasses being placed under the VWP. For another setup, water (a liquid) is used as the absorber instead of the VWP. The setting details of the simulation of the experiment are explained in this chapter. Finally, the results of the experiments are compared to those of the simulations.

5.1 Setup 1: The virtual water phantom

5.1.1 Experimental Setup

The measurement of the depth-dose profile was performed by using a proton beam that radiated to the different absorber thicknesses, as shown in figure 5.1(a). The absorber is the VWP, which has a constant thickness (the lowest thickness of the VWP is 2 mm). The material component of the VWP is comprised of H:0.077, C:0.687, N:0.023, O:0.189, Cl:0.001, and Ca:0.023 with a density of 1.03 g/cm³. In this setup for the measurement, the proton beam, after passing through the VWP, is measured by the fabricated scintillating glass. The measurement was tested in a dark box, to prevent light from entering the environment. The top of the dark box was cut into an aperture for proton beam entrance with a dimension of 40 × 40 mm², which is covered by a piece of thin black plastic tape to protect it from the external light source. In figure 5.1(b), the measurement of the depth-dose profile was performed by radiating a proton beam to the glass placed at fixed position and increasing the VWP thickness by stacking it up layer by layer. The proton beam was accelerated in the cyclotron (Varian ProBeam Compact Therapy System) at KCMH. A 543-nm air-spaced doublet collimator (F810SMA-543) was used to collect the

emission light from the glass. Then, its data was sent to the spectrometer (AvaSpec-ULS4096CL-EVO) via SMA fiber optics. The integration time of the spectrometer was set to 6 seconds for the collection period of the emitted scintillator light. The proton beam was set at an energy of 70 MeV, a dose of 2500 M.U. (25 Gy), and a beam current of 350 nA. The distance from the proton nozzle to the glass was fixed at 42.1 cm and the glass was placed exactly at the isocenter.

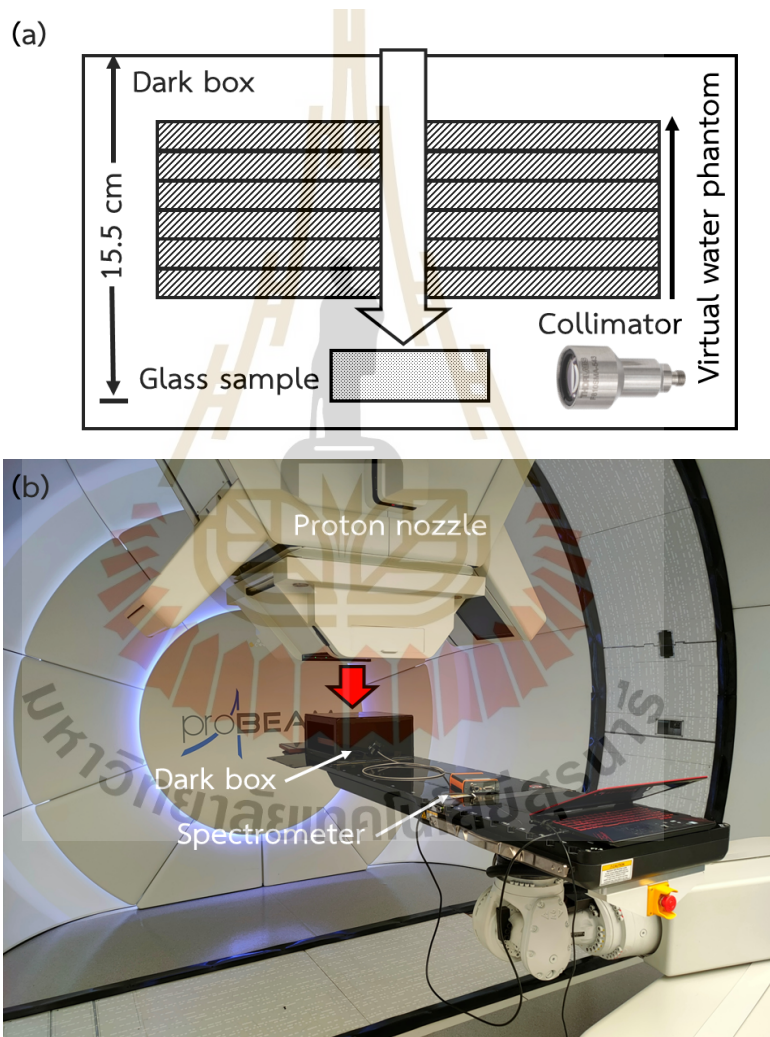


Figure 5.1 (a) The setup of the depth-dose profile in the setup of the virtual water phantom where x is the VPW thickness and (b) the experimental setup in the gantry room at KCMH. The red arrow represents the proton beam direction in the vertical direction.

5.1.2 Measurement process

The process of taking a measurement is divided into two steps: preparing the proton beam and using the spectrometer to collect the emitted light from the glass. In figure 5.2, the initial point of the measurement is the zero thickness of the absorber (without VPW). Then, the proton beam is prepared by selecting the quality assurance (QA) mode. The background signal is saved by the spectrometer at that time (Save_dark process). The prepared proton beam then begins to irradiate the glass sample with its dose. The spectrometer stops recording when the proton beam finishes delivering its dose. These are the complete measurements for each thickness of the absorber. The process is continued by adding absorber thickness, and the process starts all over again until the final thickness is reached.

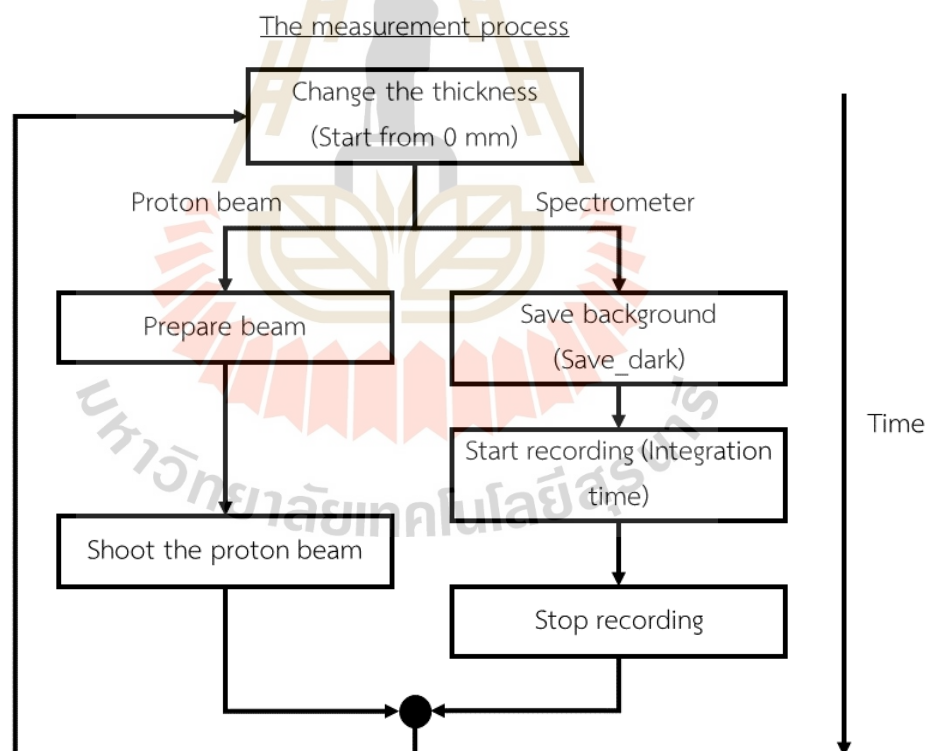


Figure 5.2 The schematic measurement process.

5.1.3 Light yield calculations

The depth-dose profile was set up to record the emission light from the scintillating glass when it was irradiated by a proton beam. Due to the limitations of our collimator, the emission light was recorded in the wavelength range of 350–750 nm. The spectra were analyzed using the ROOT framework with the Gumbel function (Antcheva et al., 2009; Gumbel, 1935). The Gumbel function was defined by following the Eq. (5.1),

$$f(x) = \frac{A}{\beta} e^{-(x-\mu)/\beta} - e^{-(x-\mu)/\beta} + C \quad (5.1)$$

where β and μ were the scale and location parameter, respectively. C represents the background signal of the measurement as a function of a constant line. The A parameter in Eq. (5.1) represents the total emission light for each VWP thickness

The glass sample for testing with the proton beam is chosen by considering the glass that provides the highest emitted light under x-ray irradiation. As reported in Table 4.1, the 1.5Ce glass sample shows the highest emitted light compared to that of other glass samples. Thus, the 1.5Ce glass sample is chosen to be tested with the proton beam at KCMH.

5.1.4 Simulation

The energy deposition (E_{dep}) of the proton beam, which it obtains from the calculations, defines the amount of light yield emitted by the scintillating glass. GATE packages version 8.2, which is based on the Geant4 toolkit, was used to compute the E_{dep} (Jan et al., 2004; Jan et al., 2011; Sarrut et al., 2014). In the calculation of the depth-dose profile measurement, we consider the contributions from the air gap, thin black plastic, virtual water phantom, and glass scintillator, respectively. The simulation takes into account the interaction with the air particle. In figure 5.3, the simulation shows the proton path passing through each part of the equipment. The simulation was carried out with 10^6 primary protons and the recommended physics list for hadron therapy applications, QGSP_BIC_EMY (Almurayshid et al., 2017; Winterhalter et al., 2020). The simulation also includes the interaction of a proton beam with air. The

simulation calculated the total E_{dep} within the glass thickness of 3 mm. The results are integrated into the glass sample for the E_{dep} .

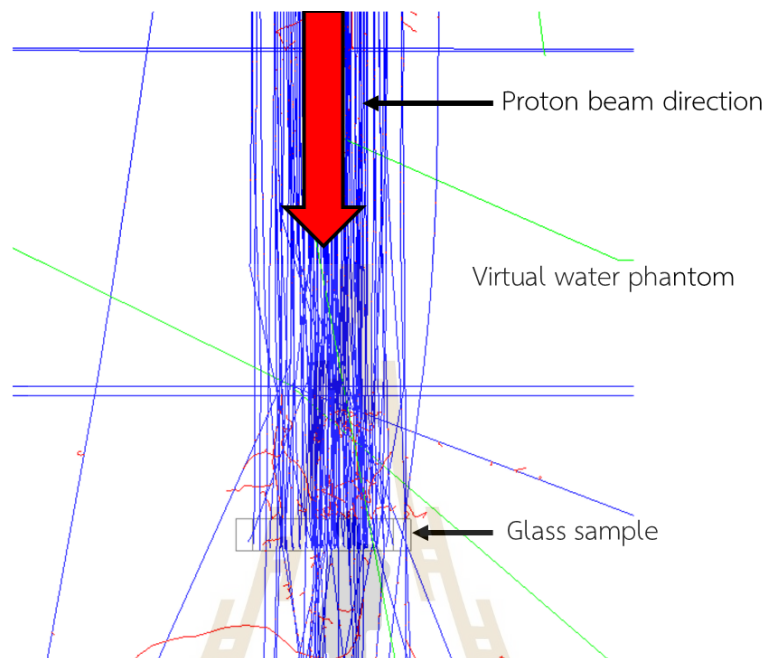


Figure 5.3 The simulation of the measurement in the virtual water phantom. The red arrow represents the proton beam direction from the nozzle to the glass sample.

5.1.5 Comparison between experiments and simulations

The results showed that the intensity peaks of both the measured emission light from the glass scintillator and the simulated energy deposition are located inside the glass scintillator after passing through a 3.2 cm of virtual water phantom with a similar plateau trend, as shown in figure 5.4. However, the measured light intensity peak was significantly lower than that of the simulation. In this case, the emission light was reduced in a process known as quenching, which was the same phenomenon found in the plastic scintillator (Almurayshid et al., 2017; Birks J. B., 1964). This reduction phenomenon of emission light was also discovered in the study of Gd^{3+} - and Ce^{3+} -doped fibers under proton radiation (Hoehr et al., 2019).

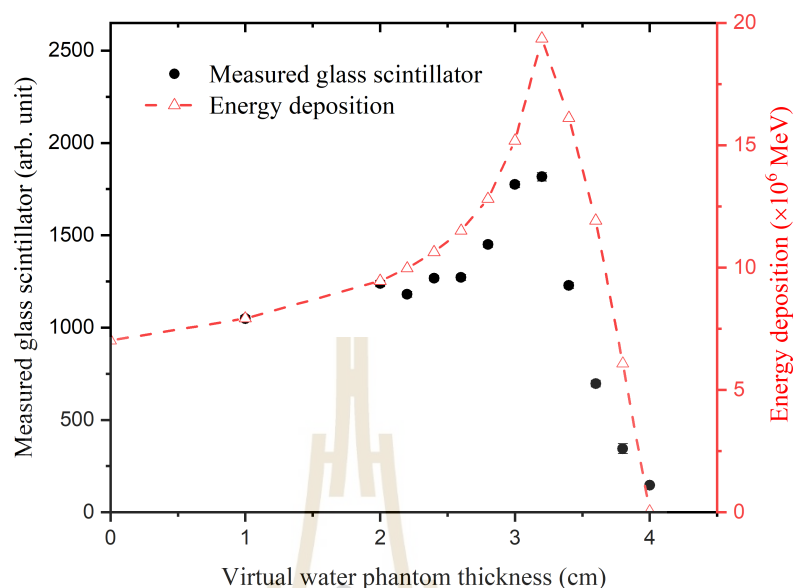


Figure 5.4 Comparison the results between experiments and simulations.

5.2 Setup 2: The water phantom

5.2.1 Experimental Setup

The depth-dose profile of the proton beam for the second setup was measured by dipping fabricated glass into a water tank. The water tank contains both the water and a glass holder for a light measurement system. The water tank is made of Polymethyl methacrylate (PMMA) with a tank wall thickness of 10 mm. The glass is put into a centered glass holder and compacted with the light measurement system. The glass holder box has a dimension of 3×3 cm², made of black PETG filament. The proton pass through the tank wall, water, glass holder, and glass, respectively, as shown in figure 5.5. The light measurement system consists of the collimator connected to the spectrometer. It is the same system as the VWP setup. To get the depth-dose profile, the proton beam was irradiated into the glass, passing through water with different thicknesses. The thickness of the water was changed by moving the glass holder away from the water tank tank wall. This movement is done with a linear motion guide controlled by a motorized ball screw. This controller is called the

“water-depth control box”, which was designed and constructed by a member of our group, Passakorn Phumara.

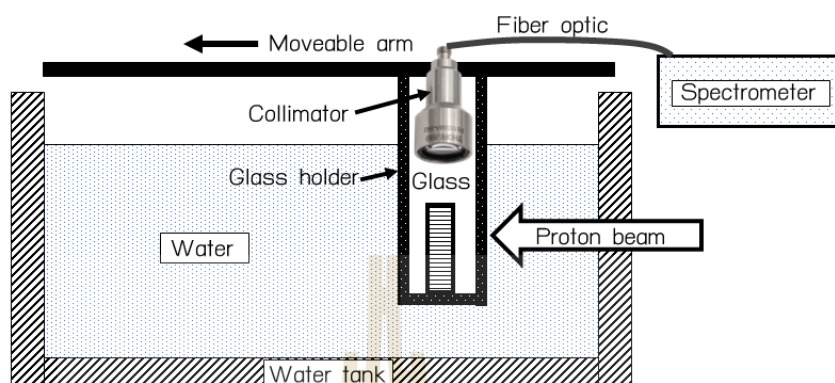


Figure 5.5 Schematic setup for the measurement of the water phantom. The water tank is made from an 10 mm acrylic. The scintillating glass was compacted with the collimator inside the glass holder, where it is made of 3 mm PETG.

In figure 5.6, the measurement was set up in the gantry room at KCMH. A 543-nm air-spaced doublet collimator (F810SMA-543) was located on top of the glass sample inside the glass holder. The collimator was used to collect the emitted light when the glass was irradiated by the proton beam. The data of the emitted light was delivered to the spectrometer (AvaSpec-ULS4096CL-EVO) via SMA fiber optics. The integration time of the spectrometer was set to 6 seconds. The proton beam’s energy was set to 70 MeV, the dose to 2,500 M.U. (25 Gy), and the beam current to 300 nA. For the measurement process, it is the same as the process that is described in Section 5.1.2.

5.2.2 Simulation

GATE packages version 8.2 are used in the simulation part to calculate the E_{dep} , as mentioned in Section 5.1.4. In this setup, the proton beam comes from the proton nozzle and then passes through the setup, which includes the tank wall (10 mm), water, glass holder (2 mm), and glass sample (3 mm), respectively. In figure 5.7, the simulation illustrates the proton beam path radiating to the setup. The simulation calculated the amount of E_{dep} on the scintillating glass by the proton beam. The E_{dep} of the scintillating glass was



Figure 5.6 The setup of the water phantom of the depth-dose profile at KCMH.

calculated for each thickness of water. Then, the deposited energy integrates within the glass thickness (3 mm) for the total E_{dep} for each thickness of water.

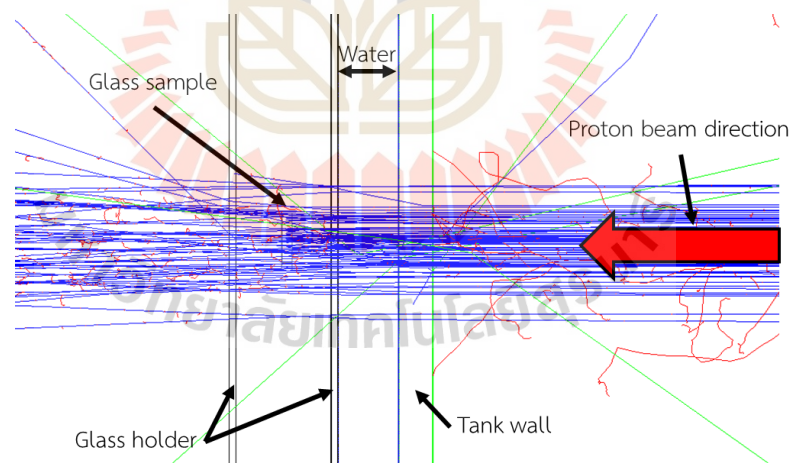


Figure 5.7 The simulation of the depth-dose profile in the setup of the water phantom. The proton beam radiates to the glass sample.

5.2.3 Comparison between experiments and simulations

The depth-dose profile of the proton beam in the setup of the water phantom was determined by utilizing the scintillating glasses shown in figure 5.8. The emitted light intensity increases as the water thickness increases from 10 to 15 mm, and it significantly drops beyond 18 mm. We calculated the proton energy deposition in the glass sample to confirm the measured results. The depth-dose profile does not demonstrate a significant Bragg peak around 10 to 15 mm as reported by the simulation, as shown by the red dots in figure 5.8. The measured light intensity fluctuates, probably due to glass non-uniformity and scattering with front-end components (the water tank wall and the plastic glass holder). The experimental results were in agreement with the calculated results, which followed the measured trend in emitted light and energy deposition. We can conclude that the depth-dose profile of the proton beam can be detected by inserting CeF_3 ions into scintillating glasses.

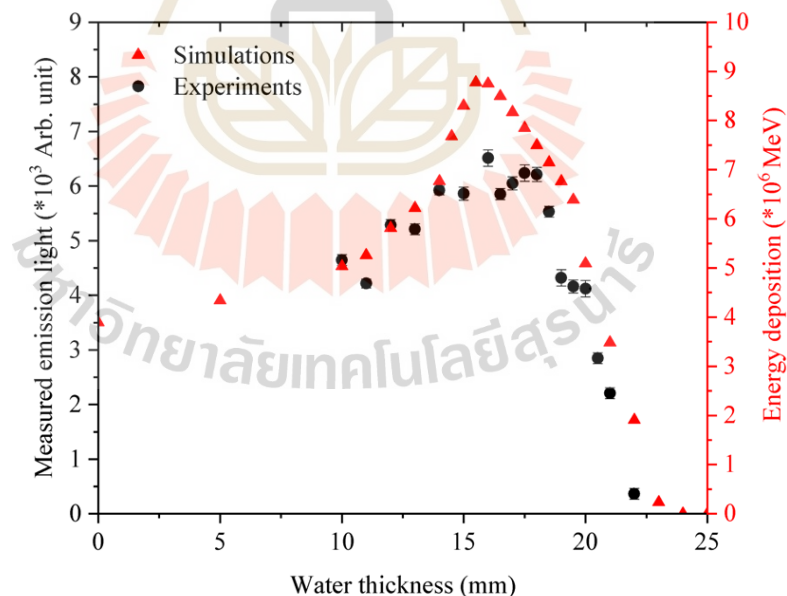


Figure 5.8 Comparison between experiments and simulations of the results in the setup of the water phantom.

5.3 Summary

This section describes the process of measuring the depth-dose profile by comparing the results between the emission light emitted by scintillating glasses and the calculated deposition energy. The two setups are using different two absorbers for the measurements, VWP and water. The first setup, which used a constant 2 mm VWP thickness with fixed position of the glass scintillator, revealed the depth-dose profile of the proton beam. The results are compatible with the deposition energy from those of the simulations. And second, using the water tank, we can continuously vary the water depth with the absorber's provided data points of different thickness. However, the emission light around the Bragg peak of the depth-dose profile was not as clear compared to the simulations. The right position of Bragg's peak cannot be observed by our fabricated scintillating glasses due to the non-homogeneous glasses and low emitted light under the proton beam. Using our fabricated scintillating glasses, we can conclude that the setups can provide an estimation of the depth-dose profile.

CHAPTER VI

SUMMARY AND CONCLUSION

The Ce^{3+} -doped glasses were successfully fabricated using quenching techniques. In this thesis, there are two types of glasses that are cerium ion doped, including gadolinium-aluminum-fluoroborate (GAF) glasses and gadolinium-barium-fluoroborate (GBF) glasses. Physical and scintillating properties of the fabricated glasses were determined and analyzed, such as glass density and spectroscopic properties such as transmittance, photoluminescence, XANES, and x-ray-induced luminescence. The CeF_3 -doped GAF glasses revealed glass properties of the coexistence of Ce^{3+} and Ce^{4+} oxidation states and a short decay time in a range of nanoseconds. The low concentration of Ce^{3+} dopant provided a higher light output under x-ray radiation. For another glass host, barium oxide was considered to be the host in the GBF glass. The CeF_3 -GBF revealed that the fraction of Ce^{3+} increased with increasing of CeF_3 in the glass and reduced with increasing of BaO fraction. The states of Gd^{3+} were observed in the CeF_3 -doped glass. Conversely, an increasing of BaO concentration vanished the state in PL of both states of Ce^{3+} and Gd^{3+} . Under x-ray radiation, the doped glass with a higher CeF_3 (Ce^{3+}) provided more emitted light (Sun et al., 2017; Sun et al., 2014b).

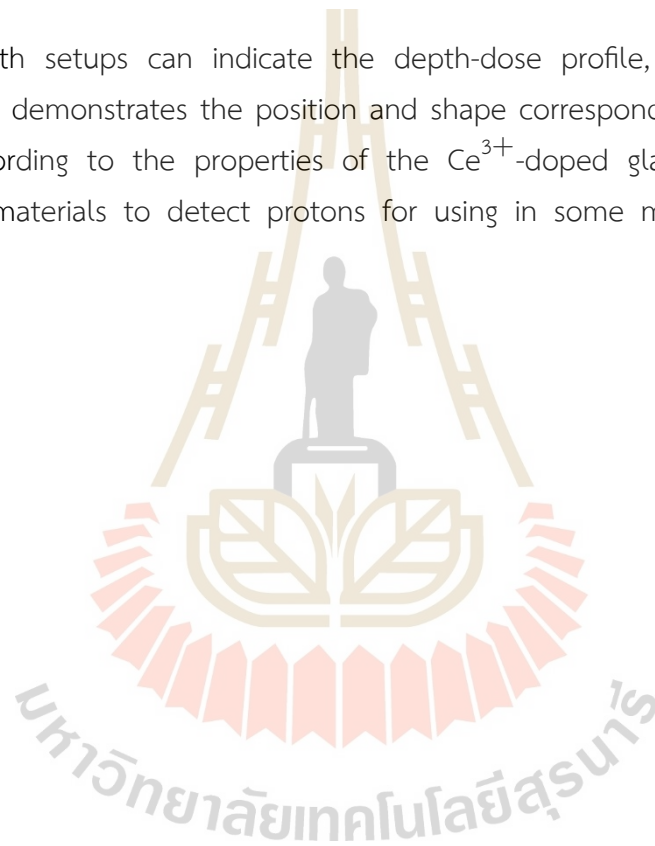
The fabricated Ce^{3+} -doped glasses were used to measure the depth-dose profile of 70 MeV proton energy. To illustrate the proton profile, the glass measured the emission light for different absorber thicknesses. The development of the measurement has two versions, including the setups of the virtual water phantom and a water phantom. The simulation results demonstrated by GATE/Geant4 were related to the measured emission light. The setup of the virtual water phantom provided the similar depth-dose profile compared to the deposition energy from the simulations. For the second setup, water can continuously vary the water depth and show a more consistent profile of the proton beam. We can conclude the results by:

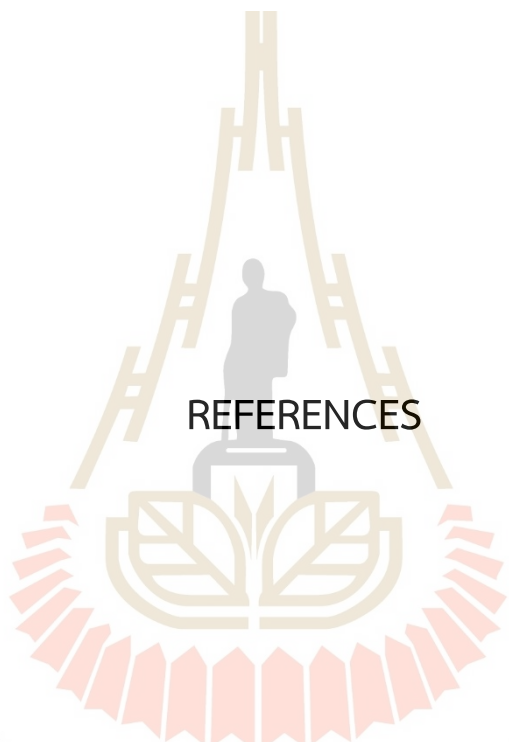
- Virtual water phantom: The setup was used 2 mm VWP thickness as an absorber and stacked layer by layer. The results revealed an clear proton

beam profile compared to the simulation results due to the constant thickness.

- Water phantom: Liquid water was used instead of VWP. The observed emission light revealed the similar trending of the depth-dose profile, as confirmed by the simulation results. However, the measured emissions around Bragg's peak position are unclear due to the non-homogeneous glass sample.

Although both setups can indicate the depth-dose profile, the water phantom setup clearly demonstrates the position and shape corresponding to the simulation results. According to the properties of the Ce^{3+} -doped glasses, they might be suitable as materials to detect protons for using in some medical applications.





REFERENCES

มหาวิทยาลัยเทคโนโลยีสุรนารี

REFERENCES

- Alme, J., Barnaföldi, G. G., Barthel, R., Borshchov, V., Bodova, T., van den Brink, A., Brons, S., Chaar, M., Eikeland, V., Feofilov, G., Genov, G., Grimstad, S., Grøttvik, O., Helstrup, H., Herland, A., Hilde, A. E., Igoikin, S., Keidel, R., Kobdaj, C., van der Kolk, N., Listratenko, O., Malik, Q. W., Mehendale, S., Meric, I., Nesbø, S. V., Odland, O. H., Papp, G., Peitzmann, T., Seime Pettersen, H. E., Piersimoni, P., Protsenko, M., Rehman, A. U., Richter, M., Röhrich, D., Samnøy, A. T., Seco, J., Setterdahl, L., Shafiee, H., Skjolddal, Ø. J., Solheim, E., Songmoolnak, A., Sudár, Á., Sølve, J. R., Tambave, G., Tymchuk, I., Ullaland, K., Underdal, H. A., Varga-Köfaragó, M., Volz, L., Wagner, B., Widerøe, F. M., Xiao, R. Z., Yang, S., and Yokoyama, H. (2020). A High-Granularity Digital Tracking Calorimeter Optimized for Proton CT. *Frontiers in Physics*, 8, 1–20.
- Almurayshid, M., Helo, Y., Kacperek, A., Griffiths, J., Hebden, J., and Gibson, A. (2017). Quality assurance in proton beam therapy using a plastic scintillator and a commercially available digital camera. *Journal of Applied Clinical Medical Physics*, 18(5), 210–219.
- Antcheva, I., Ballintijn, M., Bellenot, B., Biskup, M., Brun, R., Buncic, N., Canal, P., Casadei, D., Couet, O., Fine, V., Franco, L., Ganis, G., Gheata, A., Maline, D. G., Goto, M., Iwaszkiewicz, J., Kreshuk, A., Segura, D. M., Maunder, R., Moneta, L., Naumann, A., Offermann, E., Onuchin, V., Panacek, S., Rademakers, F., Russo, P., and Tadel, M. (2009). ROOT - A C++ framework for petabyte data storage, statistical analysis and visualization. *Computer Physics Communications*, 180(12), 2499–2512.
- Bashkirov, V. A., Johnson, R. P., Sadrozinski, H. F., and Schulte, R. W. (2016). Development of proton computed tomography detectors for applications in hadron therapy. *Nuclear Instruments and Methods in Physics Research, Section A: Accelerators, Spectrometers, Detectors and Associated Equipment*, 809, 120–129.

- Bethe, H. (1930). Zur theorie des durchgangs schneller korpuskularstrahlen durch materie. *Annalen der Physik*, 397(3), 325-400.
- Birks J. B. (1964). *The Theory and Practice of Scintillation Counting*. Oxford: Pergamon.
- Bloch, F. (1933). Zur bremsung rasch bewegter teilchen beim durchgang durch materie. *Annalen der Physik*, 408(3), 285-320.
- Bragg, W. H. and Kleeman, R. (1905). On the Alpha Particles of Radium and Their Loss of Range in Passing through Various Atoms and Molecules. *Philosophical Magazine*, 10(57), 318-340.
- Bucciantonio, M., Amaldi, U., Kieffer, R., Sauli, F., and Watts, D. (2013). Development of a fast proton range radiography system for quality assurance in hadrontherapy. *Nuclear Instruments and Methods in Physics Research, Section A: Accelerators, Spectrometers, Detectors and Associated Equipment*, 732, 564–567.
- Chewpraditkul, W., He, X., Chen, D., Shen, Y., Sheng, Q., Yu, B., Nikl, M., Kucerkova, R., Beitlerova, A., Wanarak, C., and Phunpueok, A. (2011). Luminescence and scintillation of Ce³⁺-doped oxide glass with high Gd₂O₃ concentration. *Physica Status Solidi (A) Applications and Materials Science*, 208(12), 2830–2832.
- Civinini, C., Bruzzi, M., Bucciolini, M., Carpinelli, M., Cirrone, G. A., Cuttone, G., Lo Presti, D., Pallotta, S., Pugliatti, C., Randazzo, N., Romano, F., Scaringella, M., Sipala, V., Stancampiano, C., Talamonti, C., Vanzi, E., and Zani, M. (2013). Recent results on the development of a proton computed tomography system. *Nuclear Instruments and Methods in Physics Research, Section A: Accelerators, Spectrometers, Detectors and Associated Equipment*, 732, 573–576.
- Darafsheh, A., Taleei, R., Kassaee, A., and Finlay, J. C. (2017). Proton therapy dosimetry using the scintillation of the silica fibers. *Optics Letters*, 42(4), 847.
- Dixie, L. C., Edgar, A., and Bartle, C. M. (2014). Samarium doped calcium fluoride: A red scintillator and X-ray phosphor. *Nuclear Instruments and Methods in Physics Research, Section A: Accelerators, Spectrometers, Detectors and Associated Equipment*, 753, 131–137.

- Fu, J., Parker, J. M., Brown, R. M., and Flower, P. S. (2003). Compositional dependence of scintillation yield of glasses with high Gd₂O₃ concentrations. *Journal of Non-Crystalline Solids*, 326–327, 335–338.
- González M., D., Becerro, A. I., Calderón-Olvera, R. M., Cantelar, E., Corral, A., Balcerzyk, M., de la Fuente, J. M., and Ocaña, M. (2021). Neodymium doped lanthanide fluoride nanoparticles as contrast agents for luminescent bioimaging and X-ray computed tomography. *Boletín de la Sociedad Española de Cerámica y Vidrio*, 1, 40–49.
- Gumbel, E. (1935). Les valeurs extrêmes des distributions statistiques. *Annales de l'institut Henri Poincaré*, 2, 115–158.
- Haas, A. D., Nooren, G., Peitzmann, T., Reicher, M., Rocco, E., Rohrich, D., Ullaland, K., Brink, A. V. D., Leeuwen, M. V., Wang, H., Yang, S., and Zhang, C. (2018). The focal prototype - an extremely fine-grained electromagnetic calorimeter using cmos pixel sensors. *Journal of Instrumentation*, 13(1), P01014.
- Han, Y. (2019). Current status of proton therapy techniques for lung cancer. *Radiation Oncology Journal*, 37(4), 232–248.
- Hoehr, C., Morana, A., Duhamel, O., Capoen, B., Trinczek, M., Paillet, P., Duzenli, C., Bouzaoui, M., Bouwmans, G., Cassez, A., Ouerdane, Y., Boukenter, A., El Hamzaoui, H., and Girard, S. (2019). Novel Gd³⁺-doped silica-based optical fiber material for dosimetry in proton therapy. *Scientific Reports*, 9(1), 4–11.
- Jan, S., Benoit, D., Becheva, E., Carlier, T., Cassol, F., Descourt, P., Frisson, T., Grevillot, L., Guigues, L., Maigne, L., Morel, C., Perrot, Y., Rehfeld, N., Sarrut, D., Schaart, D. R., Stute, S., Pietrzyk, U., Visvikis, D., Zahra, N., and Buvat, I. (2011). GATE V6: A major enhancement of the GATE simulation platform enabling modelling of CT and radiotherapy. *Physics in Medicine and Biology*, 56(4), 881–901.
- Jan, S., Benoit, D., Becheva, E., Lin, H.-h., Chuang, K.-s., Lin, Y.-h., Pet, C., España, S., Herraiz, J. L., Vicente, E., Lazaro, D., Buvat, I., and Loudos, G. (2004). GATE : a simulation toolkit for PET and SPECT. *Physics in Medicine and Biology*, 49, 4543–4561.

- Johnson, R. P. (2017). Review of medical radiography and tomography with proton beams. *Reports on Progress in Physics*, 81(1), 016701.
- Kaewjaeng, S., Kaewkhao, J., Limsuwan, P., and Maghanemi, U. (2012). Effect of BaO on optical, physical and radiation shielding properties of SiO₂-B₂O₃-Al₂O₃-CaO-Na₂O glasses system. *Procedia Engineering*, 32, 1080–1086.
- Kamada, K., Kurosawa, S., Yokota, Y., Pejchal, J., Ohashi, Y., Yoshino, M., and Yoshikawa, A. (2016). Single Crystal Growth of Cerium and Praseodymium. *486 IEEE TRANSACTIONS ON NUCLEAR SCIENCE*, 63(2), 486–489.
- Liu, L., Shao, C., Zhang, Y., Liao, X., Yang, Q., Hu, L., and Chen, D. (2016). Scintillation properties and X-ray irradiation hardness of Ce³⁺-doped Gd₂O₃-based scintillation glass. *Journal of Luminescence*, 176, 1–5.
- Lo Presti, D., Aiello, S., Bonanno, D. L., Cirrone, G. A., Leonora, E., Longhitano, F., Pugliatti, C., Randazzo, N., Romano, F., Russo, G. V., Russo, M., Stancampiano, C., and Sipala, V. (2014). *Nuclear Instruments and Methods in Physics Research, Section A: Accelerators, Spectrometers, Detectors and Associated Equipment*, 737, 195–202.
- Mager, M. (2016). ALPIDE, the Monolithic Active Pixel Sensor for the ALICE ITS upgrade. *Nuclear Instruments and Methods in Physics Research, Section A: Accelerators, Spectrometers, Detectors and Associated Equipment*, 824, 434–438.
- Masai, H., Okada, G., Torimoto, A., Usui, T., Kawaguchi, N., and Yanagida, T. (2018). X-ray-induced Scintillation Governed by Energy Transfer Process in Glasses. *Scientific Reports*, 8(1), 1–8.
- Minami, Y., Gabayno, J. L., Agulto, V. C., Lai, Y., Empizo, M. J. F., Shimizu, T., Yamanoi, K., Sarukura, N., Yoshikawa, A., Murata, T., Guzik, M., Guyot, Y., Boulon, G., Harrison, J. A., and Cadatal-Raduban, M. (2019). Spectroscopic investigation of praseodymium and cerium co-doped 20Al(PO₃)₃-80LiF glass for potential scintillator applications. *Journal of Non-Crystalline Solids*, 521, 119495.

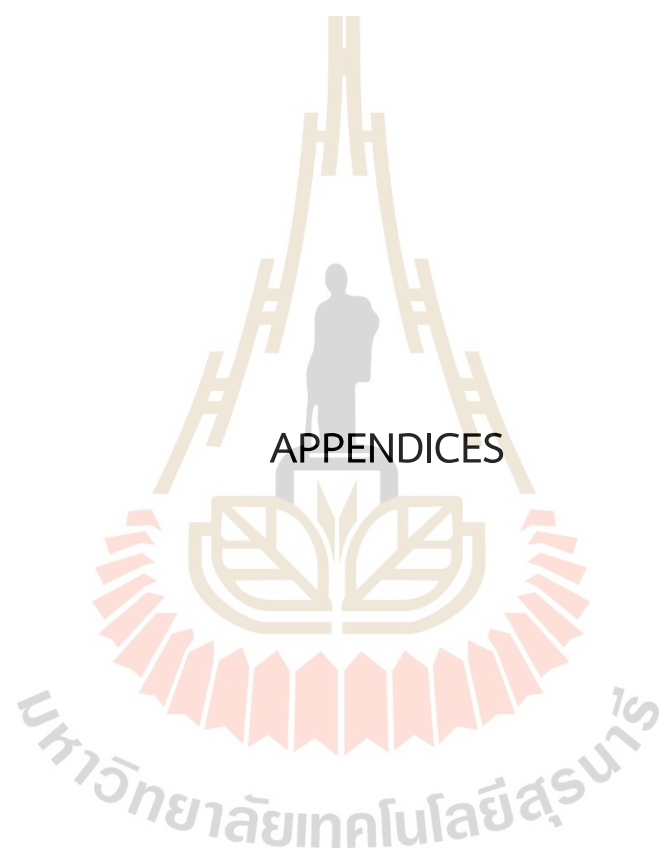
- Mott, N. F., Davis, E. A., and Street, R. A. (1975). States in the gap and recombination in amorphous semiconductors. *Philosophical Magazine*, 32(5), 961–996.
- Naimuddin, M., Coutrakon, G., Blazey, G., Boi, S., Dyshkant, A., Erdelyi, B., Hedin, D., Johnson, E., Krider, J., Rukalin, V., Uzunyan, S. A., Zutshi, V., Fordt, R., Sellberg, G., Rauch, J. E., Roman, M., Rubinov, P., and Wilson, P. (2016). Development of a proton Computed Tomography detector system. *Journal of Instrumentation*, 11(2), C02012.
- Newhauser, W. D. and Zhang, R. (2015). The physics of proton therapy. *Physics in Medicine and Biology*, 60(8), R155–R209.
- Pan, L., Daguano, J. K., Trindade, N. M., Cerruti, M., Zanotto, E. D., and Jacobsohn, L. G. (2020). Scintillation, luminescence and optical properties of Ce-Doped borosilicate glasses. *Optical Materials*, 104, 109847.
- Park, J., Ha, D., Kaewjeang, S., Maghanemi, U., Kothan, S., Kaewkhao, J., and Kim, H. (2016). Luminescence properties of Ce³⁺ doped gadolinium-calcium-silicaborate glass scintillator. *Radiation Measurements*, 90, 166–169.
- Pemler, P., Besserer, J., De Boer, J., Dellert, M., Gahn, C., Moosburger, M., Schneider, U., Pedroni, E., and Stäubli, H. (1999). Detector system for proton radiography on the gantry of the Paul-Scherrer-Institute. *Nuclear Instruments and Methods in Physics Research, Section A: Accelerators, Spectrometers, Detectors and Associated Equipment*, 432(2-3), 83–495.
- Pettersen, H. E. S., Alme, J., Barnaföldi, G. G., Barthel, R., van den Brink, A., Char, M., Eikeland, V., García-Santos, A., Genov, G., Grimstad, S., Grøttvik, O., Helstrup, H., Hetland, K. F., Mehendale, S., Meric, I., Odland, O. H., Papp, G., Peitzmann, T., Piersimoni, P., Ur Rehman, A., Richter, M., Samnøy, A. T., Seco, J., Shafiee, H., Skjæveland, E. V., Sølvi, J. R., Tambave, G., Ullaland, K., Varga-Kofarago, M., Volz, L., Wagner, B., Yang, S., and Röhrich, D. (2019). Design optimization of a pixel-based range telescope for proton computed tomography. *Physica Medica*, 63, 87–97.
- Rajagukguk, J., Sarumaha, C. S., Chanthima, N., Wantana, N., Kothan, S., Wongdamnern, N., and Kaewkhao, J. (2021). Radio and photo luminescence of

- Dy³⁺ doped lithium fluorophosphate scintillating glass. *Radiation Physics and Chemistry*, 185, 109520.
- Rajaramakrishna, R., Kaewjaeng, S., Kaewkhao, J., and Kothan, S. (2020). Investigation of XANES study and energy transport phenomenon of Gd³⁺ to Ce³⁺ in CaO–SiO₂–B₂O₃ glasses. *Optical Materials*, 102, 109826.
- Ranasinghe, K. S., Singh, R., Day, D. E., Attenkofer, K., Stavitski, E., Quinn, L. A., Patterson, D., and Duenas, A. (2019). Evidence of the coexistence of multivalence cerium oxide nano-particles in a sodium borate glass. *Journal of Non-Crystalline Solids*, 515, 75–81.
- Ravel, B. and Newville, M. (2005). ATHENA, ARTEMIS, HEPHAESTUS: Data analysis for X-ray absorption spectroscopy using IFEFFIT. *Journal of Synchrotron Radiation*, 12(4), 537–541.
- Saraya, Y., Izumikawa, T., Goto, J., Kawasaki, T., and Kimura, T. (2014). Study of spatial resolution of proton computed tomography using a silicon strip detector. *Nuclear Instruments and Methods in Physics Research, Section A: Accelerators, Spectrometers, Detectors and Associated Equipment*, 735, 485–489.
- Sarrut, D., Bardiès, M., Bousson, N., Freud, N., Jan, S., Létang, J. M., Loudos, G., Maigne, L., Marcatili, S., Mauxion, T., Papadimitroulas, P., Perrot, Y., Pietrzyk, U., Robert, C., Schaart, D. R., Visvikis, D., and Buvat, I. (2014). A review of the use and potential of the GATE Monte Carlo simulation code for radiation therapy and dosimetry applications. *Medical Physics*, 41(6), 064301.
- Scaringella, M., Brianzi, M., Bruzzi, M., Bucciolini, M., Carpinelli, M., Cirrone, G. A., Civinini, C., Cuttone, G., Lo Presti, D., Pallotta, S., Pugliatti, C., Randazzo, N., Romano, F., Sipala, V., Stancampiano, C., Talamonti, C., Tesi, M., Vanzi, E., and Zani, M. (2013). The PRIMA (PRoton IMAGING) collaboration: Development of a proton Computed Tomography apparatus. *Nuclear Instruments and Methods in Physics Research, Section A: Accelerators, Spectrometers, Detectors and Associated Equipment*, 730, 178–183.

- Schulte, R., Bashkurov, V., Li, T., Liang, Z., Mueller, K., Heimann, J., Johnson, L. R., Keeney, B., Sadrozinski, H. F., Seiden, A., Williams, D. C., Zhang, L., Li, Z., Peggs, S., Satogata, T., and Woody, C. (2004). Conceptual design of a proton computed tomography system for applications in proton radiation therapy. *IEEE Transactions on Nuclear Science*, 51(3), 866–872.
- Shi, R. D., Ma, X., Ma, P. P., Zhu, X. L., Fu, M. S., and Chen, X. M. (2020). Ba-based complex perovskite ceramics with superior energy storage characteristics. *Journal of the American Ceramic Society*, 103(11), 6389–6399.
- Sontakke, A. D., Ueda, J., and Tanabe, S. (2016). Effect of synthesis conditions on Ce^{3+} luminescence in borate glasses. *Journal of Non-Crystalline Solids*, 431, 150–153.
- Sun, X. Y., Jiang, D. G., Sun, Y. Z., Zhang, X., Hu, Q. L., Huang, Y., and Tao, Y. (2014a). Eu^{3+} -activated $\text{B}_2\text{O}_3\text{-GeO}_2\text{-RE}_2\text{O}_3$ (RE = Y^{3+} , La^{3+} and Gd^{3+}) borogermanate scintillating glasses. *Journal of Non-Crystalline Solids*, 389, 72–77.
- Sun, X.-Y., Lin, L.-W., Wu, Y.-T., Gao, P., and Xiao, Z.-H. (2015a). Enhanced Ce^{3+} emission in $\text{B}_2\text{O}_3\text{-GeO}_2\text{-Gd}_2\text{O}_3$ scintillating glasses induced by melting temperature. *Optical Materials Express*, 5(4), 920.
- Sun, X. Y., Liu, X. J., Wu, Y., Xiao, Z., Chen, Q., Wang, W. F., and Yang, Q. M. (2020a). Enhanced emission intensity of Ce^{3+} -doped aluminoborosilicate glasses prepared in air. *Ceramics International*, 46(3), 4035–4038.
- Sun, X. Y., Liu, X. J., Xiao, Z. H., Jiang, D. G., Wang, W. F., Wen, Y., Yang, Q. M., and Kang, Z. (2020b). Enhancement of emission intensity in Ce^{3+} -activated aluminoborosilicate scintillating glass synthesized in air. *Journal of the American Ceramic Society*, 103(2), 768–772.
- Sun, X. Y., Xiao, Z. H., Wu, Y. T., and Kang, Z. (2017). Fast Ce^{3+} -activated borosilicate glass scintillators prepared in air atmosphere. *Ceramics International*, 43(3), 3401–3404.

- Sun, X. Y., Xiao, Z. H., and Zhong, J. P. (2015b). Alkaline-earth oxide network modifier on optical properties of Ce^{3+} -activated borogermanate glasses. *Optical Materials*, 50, 110–113.
- Sun, X.-Y., Ye, Z.-P., Wu, Y.-T., Gao, P., Mao, R.-H., Zhang, Z.-J., and Zhao, J.-T. (2014b). A Simple and Highly Efficient Method for Synthesis of Ce^{3+} -Activated Borogermanate Scintillating Glasses in Air. *Journal of the American Ceramic Society*, 97(11), 3388–3391.
- Tang, G., Qian, G., Shi, Z., Liu, Y., Huang, B., He, Y., Jiang, L., Sun, M., Qian, Q., and Yang, Z. (2019). Heavily Tb^{3+} doped multi-component phosphate glass fibers for green fiber lasers. *Optical Materials Express*, 9(2), 362.
- Taylor, J. T., Allport, P. P., Casse, G. L., Smith, N. A., Tsurin, I., Allinson, N. M., Esposito, M., Kacperek, A., Nieto-Camero, J., Price, T., and Waltham, C. (2015). Proton tracking for medical imaging and dosimetry. *Journal of Instrumentation*, 10(2), C02015.
- Wang, Q., Yang, B., Zhang, Y., Xia, H., Zhao, T., and Jiang, H. (2013). High light yield Ce^{3+} -doped dense scintillating glasses. *Journal of Alloys and Compounds*, 581, 801–804.
- Wang, S., Chen, G., Baccaro, S., Cecilia, A., Du, Y., Nie, J., and Zhang, Y. (2003). Radiation hardness of Ce^{3+} -doped heavy germanate glasses. *Nuclear Instruments and Methods in Physics Research, Section B: Beam Interactions with Materials and Atoms*, 201(3), 475–479.
- Wantana, N., Kaewnuam, E., Chanthima, N., Kaewjaeng, S., Kim, H. J., and Kaewkhao, J. (2018). Ce^{3+} doped glass for radiation detection material. *Ceramics International*, 44, S172–S176.
- Wilkinson, C. J., Ruane, L., Miller, W., Gunsch, A., Zieser, A., Tillman, I. J., Thune, Z., Wang, D., and Akgun, U. (2017). *IEEE Nuclear Science Symposium and Medical Imaging Conference*, 1–5.
- Winterhalter, C., Taylor, M., Boersma, D., Elia, A., Guatelli, S., Mackay, R., Kirkby, K., Maigne, L., Ivanchenko, V., Resch, A. F., Sarrut, D., Sitch, P., Vidal, M.,

- Grevillot, L., and Aitkenhead, A. (2020). Evaluation of GATE-RTion (GATE/Geant4) Monte Carlo simulation settings for proton pencil beam scanning quality assurance. *Medical Physics*, 47(11), 5817–5828.
- Xu, P., Fu, Z., Fan, S., Lin, H., Li, C., Yao, G., Chen, Q., Zhou, Y., and Zeng, F. (2018). Study on the sensitization of Gd^{3+} on Ce^{3+}/Tb^{3+} co-doped GBS scintillating glass. *Journal of Non-Crystalline Solids*, 481(7989), 441–446.
- Yao, Y., Liu, L., Zhang, Y., Chen, D., Fang, Y., and Zhao, G. (2016). Optical properties of Ce^{3+} doped fluorophosphates scintillation glasses. *Optical Materials*, 51, 94–97.
- Zaman, F., Rooh, G., Srisittipokakun, N., Kim, H. J., Kaewnuam, E., Meejitpaisan, P., and Kaewkhao, J. (2017). Scintillation and luminescence characteristics of Ce^{3+} doped in $Li_2O-Gd_2O_3-BaO-B_2O_3$ scintillating glasses. *Radiation Physics and Chemistry*, 130, 158–163.
- Zhao, J., Huang, L., Zhao, S., and Xu, S. (2019). Eu^{3+} doped transparent germanate glass ceramic scintillators containing LaF_3 nanocrystals for X-ray detection. *Optical Materials Express*, 9(2), 576.



APPENDIX A

FABRICATION GLASS AND MEASUREMENT GLASS PROPERTIES

A.1 Fabrication of glass

This appendix describes the process used to synthesize the scintillating glasses. The glasses of GAF and BGF were synthesized using the same method, as well as measurements of their properties.

1. Preparing the glass compositions. The two compositions of the glass were prepared as presented in Table. A.1 and A.2. The compositions of the glass were prepared into the alumina crucible, as shown figure A.1.

Table A.1 The glass name of GAF and their weight for the glass composition of $25\text{Gd}_2\text{O}_3-(65-x)\text{B}_2\text{O}_3-10\text{AlF}_3-x\text{CeF}_3$ (where $x = 0.0, 0.05, 0.1, 0.2,$ and 0.3 mol%).

Glass name	Mol%	Weight of glass compositions (g)					Total weight
		CeF ₃	Gd ₂ O ₃	H ₃ BO ₃	AlF ₃	CeF ₃	
0.05Ce:GAF	0.05	9.4179	8.3472	0.8727	0.0102	18.6378	
0.1Ce:GAF	0.1	9.4137	8.3371	0.8723	0.0205	18.6232	
0.2Ce:GAF	0.2	9.4054	8.3169	0.8716	0.0409	18.5939	
0.3Ce:GAF	0.3	9.3971	8.2968	0.8708	0.0613	18.5647	

2. Melting at high temperature. There were melted using high temperature furnace at 1,400 °C for 3 h, as shown in figure A.2.
3. Annealing to reduce glass stress. After melting the glasses at high temperature, they were reduced their stress using low temperature furnace. In figure A.3, the furnace at 500 °C was utilized to anneal the glass stress for 3 h.
4. Cutting and polishing the glass. The synthesized glasses were cool down until room temperature. Then, they were cut and polished using grinding machine for the required dimensions. In figure A.4, the glasses were polished into dimensions of $10 \times 15 \times 3 \text{ mm}^3$.

Table A.2 The glass name (BGF) and the weight of the glass with composition of $20\text{Gd}_2\text{O}_3-(80-x-y)\text{B}_2\text{O}_3-x\text{BaO}-y\text{CeF}_3$ (where $x = 10, 20,$ and 30 mol%, and $y = 0.1, 0.5, 1.0,$ and 1.5 mol%).

Glass Name	Mol%		Weight of glass compositions (g)					Total Weight
	BaO	CeF ₃	Gd ₂ O ₃	H ₃ BO ₃	AlF ₃	CeF ₃		
B10GF:Ce0.1	10	0.1	7.9557	9.4858	2.1656	0.0216	19.6288	
B10GF:Ce0.5	10	0.5	7.9261	9.3965	2.1575	0.1077	19.5879	
B10GF:Ce1.5	10	1.5	7.8532	9.1760	2.1377	0.3203	19.4871	
B10GF:Ce1.0	10	1	7.8895	9.2858	2.1475	0.2145	19.5373	
B20GF:Ce1.0	20	1	7.4378	7.4854	4.0492	0.2022	19.1746	
B30GF:Ce1.0	30	1	7.0351	5.8801	5.7449	0.1913	18.8513	

A.2 Density measurement

In the part of measuring glass density, the Archimedes principle is demonstrated by measuring the glass mass in the air (M_a) and the mass in water (M_w), as shown in the figure A.5. Water density at room temperature is 0.9971 g/cm³. We calculate the glass density (ρ_g) using the Eq. (A.1):

$$\rho_g = \frac{W_a \rho_w}{W_a - W_w} = \frac{M_a \rho_w g}{(M_a - M_w)g} = \frac{M_a \rho_w}{M_a - M_w} \quad (\text{A.1})$$

where ρ_w is the water density. W_a and W_w represent glass weight in air and water, respectively.

A.3 Determine of the oxidation state of Ce³⁺ and Ce⁴⁺

The fraction of oxidation in the matter can be determined by XANES technique. Athena software is used to calculate the fraction of the oxidation (Ravel and Newville, 2005). The Athena software can down load from this website "https://bruceravel.github.io/demeter/". For the measurement of Ce³⁺ and Ce⁴⁺, the CeF₃-Ce³⁺ and CeO₂-Ce⁴⁺ powder are reference for the calculation, as shown in figure A.6. Moreover, We can follow the method to use the Athena software in the article of "https://www.slri.or.th/BL1-1W/Athena.html", wrote by SLRI.



Figure A.1 Preparing and mixing the glass compositions in the alumina crucible.



Figure A.2 High temperature furnace at NPRU.



Figure A.3 Reducing the stress of the glass after melting at high temperature.



Figure A.4 Cutting and polishing the synthesized glasses into the required dimensions.

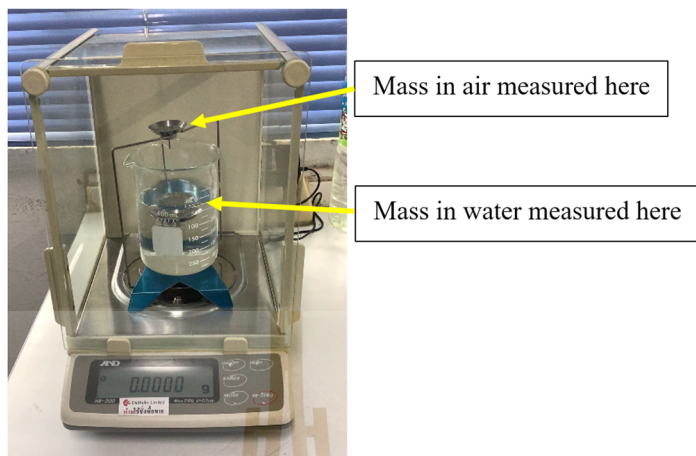


Figure A.5 The 4-digit sensitive microbalance (AND, HR-200) for measuring the glass density.

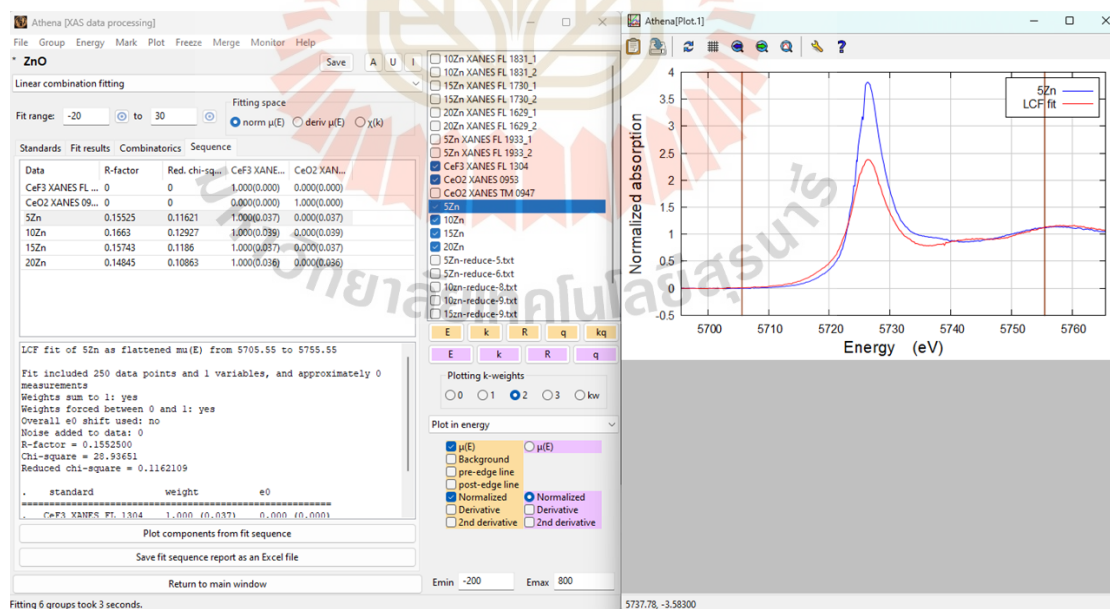


Figure A.6 Fraction of the cerium oxidation state calculated using the LCF method.

APPENDIX B

INSTALLING SIMULATION SOFTWARE

This chapter describes the installation process of the programming simulation. This consists of three programs.

- Install Geant4 toolkit
- Install ROOT framework
- Install GATE simulation

B.1 Install Geant4

To install Geant4, it should install the required software then install GATE. The list of required software is:

- a C++ compiler (new enough to compile code with the C++11 standard)
- the GNU version of make
- CMAKE tool (3.3 or newer)

To compile Geant4, we can download its data in website of <http://geant4.web.cern.ch/geant4/support/download.shtml>. Then, we call Cmake to install the Geant4 by typing:

```
cmake -DCMAKE_INSTALL_PREFIX=./geant4.10.03.p03-install
      ../geant4.10.03.p03 -DGEANT4_INSTALL_DATA=ON
      -DGEANT4_USE_QT=ON
      -DGEANT4_USE_OPENGL_X11=ON
```

If it is complete the compiling, Cmake will generate the Cmake file and folders, then we can install by typing

```
make -jN (where N is the number of processor)
make install
```

B.2 Install Root

Root can download from website of <http://root.cern/install/> and then it can execute by typing:

```
wget https://root.cern/download/root_v6.24.02.Linux-ubuntu20-x86_64-gcc9.3.tar.gz
tar -xzf root_v6.24.02.Linux-ubuntu20-x86_64-gcc9.3.tar.gz
source root/bin/thisroot.sh
```

B.3 Install GATE

After the Geant4 and ROOT are completed installation processes, GATE can download from website of <http://www.opengatecollaboration.org/>, and then we can install by typing:

```
cmake -DCMAKE_INSTALL_PREFIX=./GATE-install ./GATE
make -jN
make install
```

APPENDIX C

PROPERTY OF BEAM AT KCMH PROTON CENTER

This section describes the specific parameters of the proton beam from the cyclotron (Varian ProBeam Compact Therapy System) at King Chulalongkorn Memorial Hospital (KCMH), Thailand.

C.1 Proton beam characterization

The profile of proton beam from KCMH was measured using an ALPIDE sensor from the work of Passakorn Pummara, a master's degree student. The measured beam profile is shown in figure C.1. The results show the beam



Figure C.1 Beam profile measured by ALPIDE sensor.

profile in case of Gaussian distribution. The Gaussian distribution is defined by Eq. (C.1):

$$P(x) = \frac{1}{\sigma\sqrt{2\pi}} e^{-\frac{(x-\mu)^2}{2\sigma^2}} \quad (C.1)$$

where μ mean of the distribution and σ is the standard deviation.

C.2 The σ of proton beam

In the beam profile measurement, T. Sanghangthum, lecherer at the division of Radiation Oncology at Chulalongkorn University, measured by using Lynx PT from IBA dosimetry. The measured results show the σ size of the beam profile shown in Table C.1. The σ was measured at a different distance from the isocenter. The distance of the isocenter is positive when the measurement is close to the proton nozzle. For the negative distance, the measured beam profile is far away from the proton nozzle, as shown in figure C.2

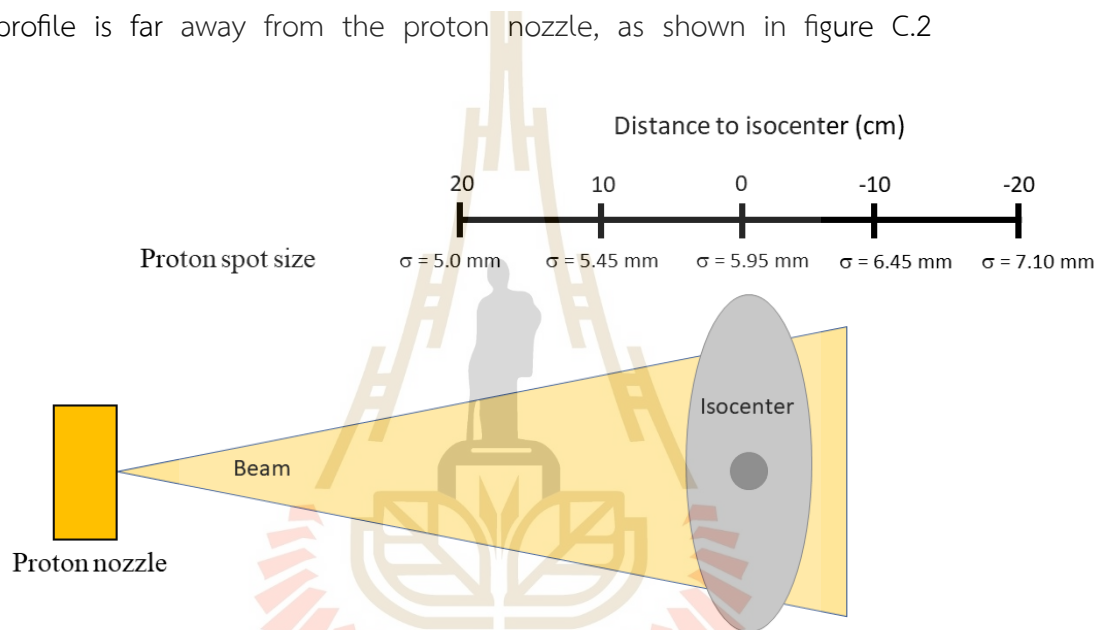


Figure C.2 Distance from the proton nozzle to the isocenter, which is defined from the proton nozzle to the isocenter. The σ is shown for the 70 MeV proton energy.

Table C.1 The σ at different distance from the proton nozzle to isocenter.

distance to isocenter (cm)	-20	-10	0	10	20
Energy(MeV)	σ (mm)				
70	7.10	6.45	5.95	5.45	5.00
80	6.40	5.95	5.50	5.15	4.75
90	6.00	5.55	5.20	4.85	4.55
100	5.65	5.20	4.95	4.65	4.35
110	5.35	5.00	4.65	4.45	4.25
120	5.05	4.70	4.50	4.35	4.15
130	4.85	4.55	4.35	4.25	4.05
140	4.65	4.40	4.20	4.05	3.95
150	4.45	4.30	4.15	4.00	3.85
160	4.35	4.15	4.05	3.85	3.80
170	4.25	4.05	3.90	3.80	3.75
180	4.20	3.95	3.80	3.80	3.55
190	4.05	3.85	3.75	3.70	3.60
200	3.95	3.75	3.65	3.60	3.50
210	3.95	3.65	3.60	3.60	3.50
220	3.80	3.70	3.50	3.50	3.40

APPENDIX D

MEASURED EMISSION LIGHT AND CALCULATED DEPOSITION ENERGY

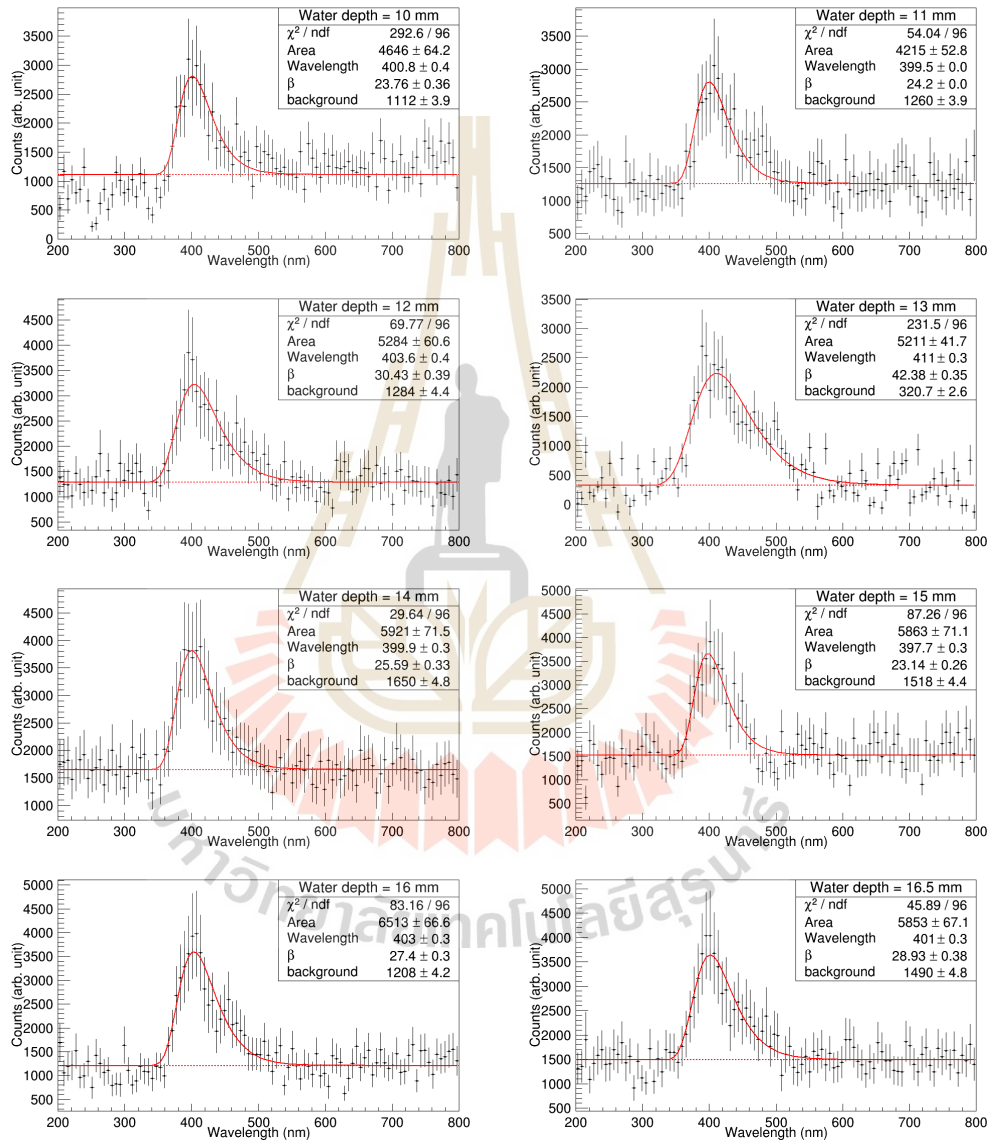


Figure D.1 Fitted emission light from the scintillating glass from a water in range of 10 - 16.5 mm.

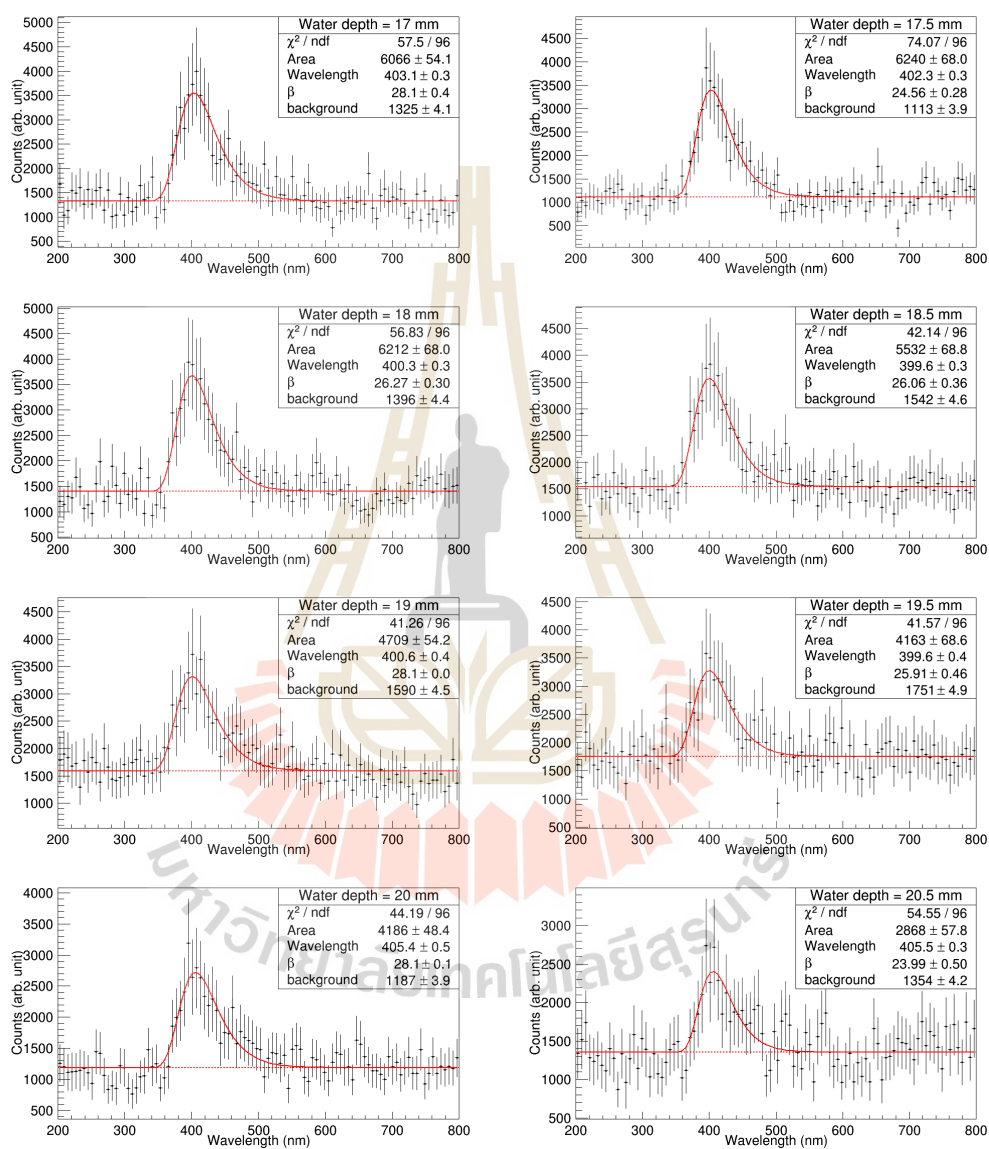


Figure D.2 Fitted emission light from the scintillating glass from a water in range of 17 - 20.5 mm.

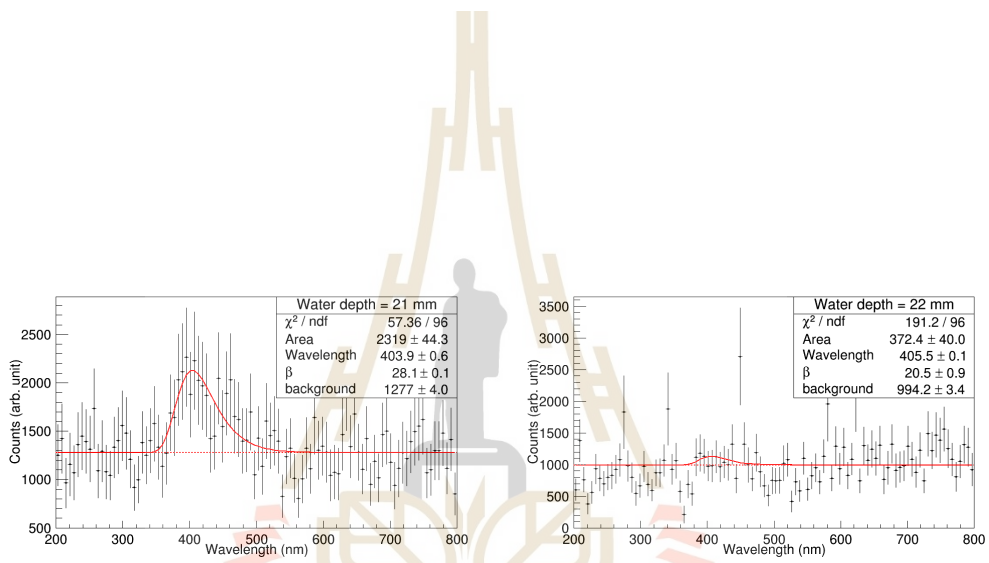


Figure D.3 Fitted emission light from the scintillating glass from a water of 21 and 22 mm.

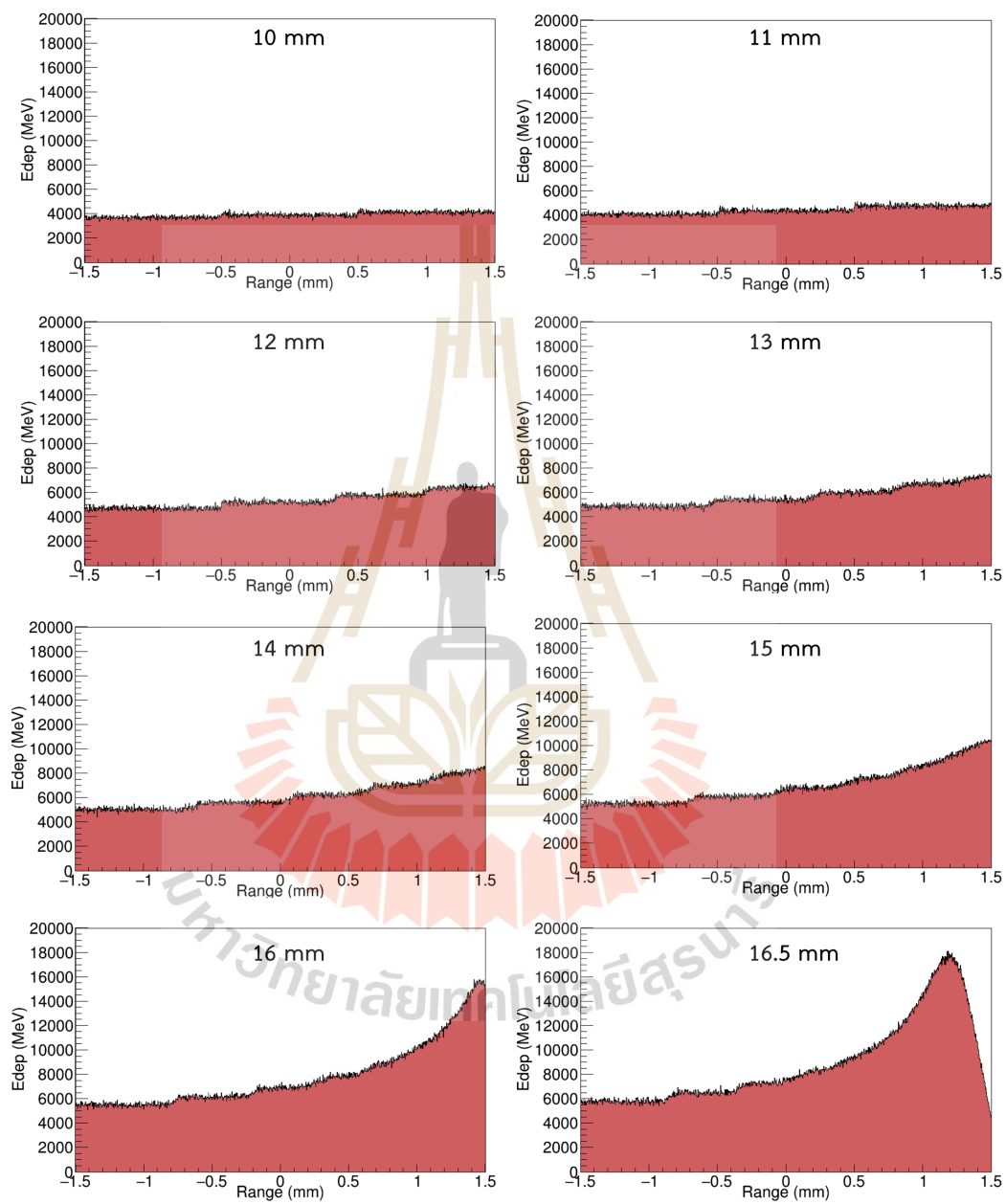


Figure D.4 Deposition energy of the glasses from the proton beam in a water in range of 10 - 16.5 mm.

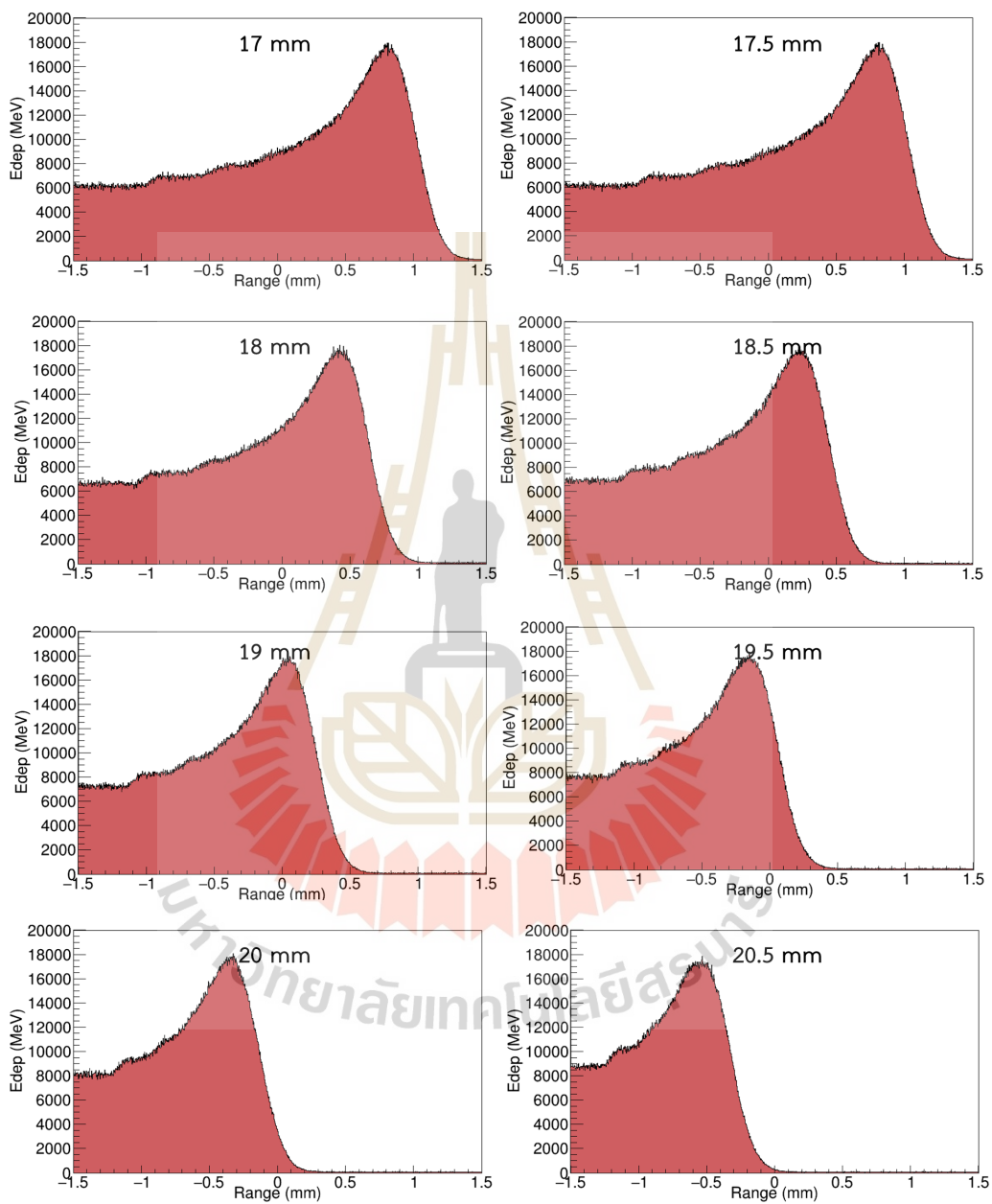


Figure D.5 Deposition energy of the glasses from the proton beam in a water in range of 17 - 20.5 mm.

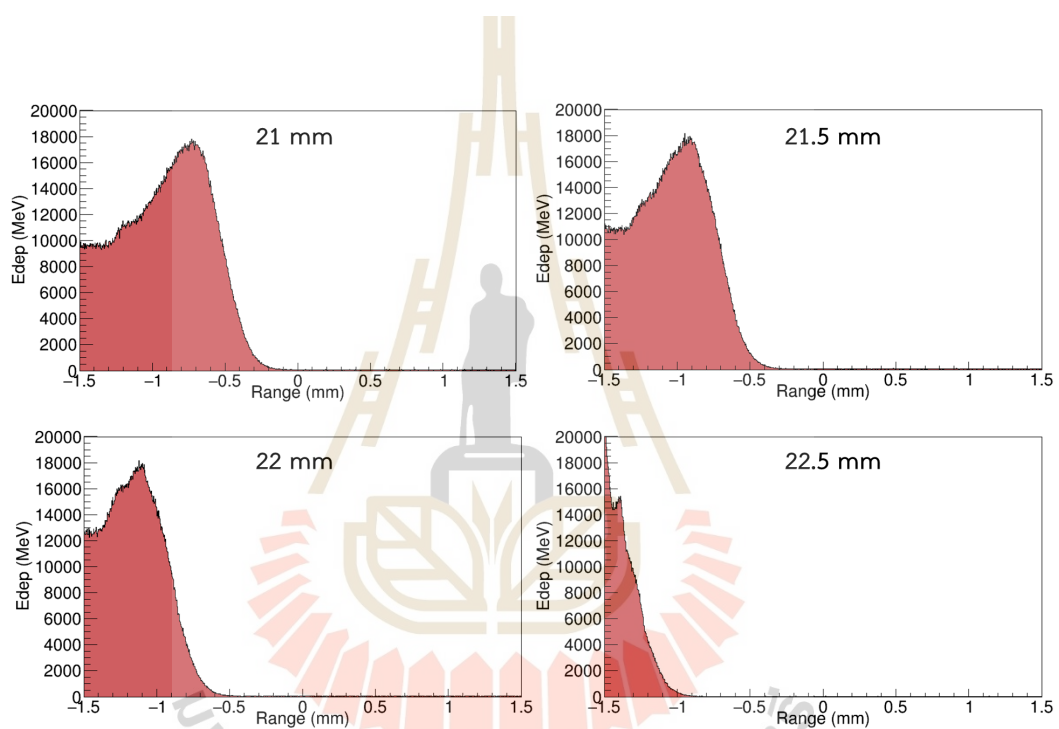


Figure D.6 Deposition energy of the glasses from the proton beam in a water in range of 21 - 22.5 mm.

CURRICULUM VITAE

Name : Mr. Phongnared Boontueng

Date of Birth : August 26, 1991

Place of Birth : Buriram, Thailand

Education :

2010 - 2014 Bachelor of Science, Department of Physics, Faculty of Science, Ubon Ratchathani university, Thailand

2015 - 2017 Master of Science, Department of Physics, Faculty of Science, Ubon Ratchathani university, Thailand

2017 - 2022 Doctor of Philosophy, School of Physics, Institute of Science, Suranaree University of Technology, Thailand

Publications :

1. **P. Boontueng**, N. Ritjoho, N. Wantana, P. Limkitjaroenporn, H.J. Kim, T. Sanghangthum, N. Chanlek, A. Limphirat, Y. Yan, J. Kaewkhao, and C. Kobdaj (2023) Fast scintillating Ce^{3+} doped gadolinium aluminum fluoroborate glass for calorimeter in proton CT prototype: a preliminary work. *Radiation Measurements*, 163, 106937.
2. **P. Boontueng**, N. Ritjoho, N. Laojamnongwong, P. Phumara, N. Wantana, N. Pinitkha, H.J. Kim, T. Sanghangthum, N. Chanlek, A. Limphirat, Y. Yan, S. Kothan, J. Kaewkhao, and C. Kobdaj (2023) Synthesis and characterization of Ce^{3+} -doped Barium-Gadolinium-Fluoroborate Glasses for proton beam diagnostic. *Optik* (submitted).